Investigating the link between bulge growth and quenching in massive galaxies through polychromatic bulge-disk decompositions in the CANDELS fields

Paola Dimauro

THÈSE DE DOCTORAT

de l'Université de recherche Paris Sciences et Lettres
PSL Research University

Préparée à l'Observatoire de Paris

Investigating the link between bulge growth and quenching in massive galaxies through polychromatic bulge-disk decompositions in the CANDELS fields

École doctorale n°127

ASTRONOMIE ASTROPHYSIQUE D'ILE-DE-FRANCE

Spécialité ASTRONOMIE ET ASTROPHYSIQUE

Soutenue par **Paola DIMAURO**
le 19 octobre 2017

Dirigée par
Marc HUERTAS-COMPANY
Emanuele DADDI

COMPOSITION DU JURY :

President: Daniel Rouan
LESIA, Observatoire de Paris

Rapporteur: Alfonso Aragón Salamanca
University of Nottingham

Rapporteur: Ignacio Trujillo
Instituto de Astrofisica de Canarias

Examinateur: Lidia Tasca
Laboratoire d'Astrophysique de Marseille

Examinateur: Alvio Renzini
Osservatorio Astronomico di Padova

PSL RESEARCH UNIVERSITY PARIS

l'Observatoire de Paris | LERMA

Abstract

Passive galaxies have different morphologies and structural properties than star-forming galaxies of similar mass. The evidence for a bimodal distribution of galaxy properties in scaling relations like the mass-size, color-magnitude, star formation rate (SFR)-mass, etc, confirms the existence of two populations and suggests a link between the quenching process and galaxy structure, namely with the presence/growth of a bulge. Understanding the origin of this correlation requires establishing constraints on the mechanisms, as well as on the timing, of bulge formation. How are bulges formed? Do bulges grow in the main sequence? Are galaxies re-accreting a star forming disk? Do galaxies start to quench from the inside? etc.

Proper answers to these questions require us to resolve the internal components of galaxies at different epochs. Thanks to the CANDELS high-resolution multi-wavelength data, I performed 2-D bulge-disk decompositions of the surface brightness profile of $\simeq$ 17.300 galaxies (F160W $<$ 23, 0 $<$ z $<$ 2) in 4-7 filters, covering a spectral distribution of 430-1600 nm. One challenge of this kind of analysis is the choice of the model (1 or 2 components) to describe the surface brightness distribution. We proposed a new approach based on deep-learning that allows us to make an a-priori selection of the best profile. It reduces contaminations from wrong fits or unphysical models caused by the second profile, which is not always needed. I fitted the 4-7 point Spectral Energy Distribution of disks and bulges independently with stellar population models (BC03) to obtain information regarding stellar masses, rest-frame colors, etc. The ensemble of the previous procedures results in a catalog that contains structural/morphological information of the stellar population properties for a large sample of bulges and disks within galaxies. The catalog is released to the community [1] and is the largest and most complete catalog of bulge-disc decomposition at $z < 2$.

I used the derived catalog to investigate how galaxies quench and how their morphology transform . If different mechanisms are acting, a signature may be left on the properties of the internal components.

[1] lerma.obspm.fr/huertas/form_CANDELS

Firstly I analyzed the distributions of bulges and disks within galaxies in the mass-size plane (separately from z$\sim$2 to z$\sim$0.5) in order to put additional constraints on their formation mechanisms. The relation between mass and size is parametrized with a power-law: $r = A\, m^{\alpha}$. Disks follow a mass-size relation with a typical slope of alpha $\sim$ 0.2 with a slight decrease at high redshift. The normalization factor 'A' increases by a factor of 1.3 from z$\sim$2. Disks at z$\sim$2 are 30% smaller than today. Interestingly, the size of the disk at fixed stellar mass does not depend on the bulge-to-total ratio of the host.

For bulges, I find that they follow a mass-size relation with a typical slope of alpha $\sim$0.5 and an intrinsic scatter of $\sim$0.2. The zeropoint increases by a factor of 2.5 from z$\sim$2. Interestingly, in this regime, at fixed stellar mass, the size of the bulge is also independent of the bulge-to-total ratio. It suggests a unique formation process for massive bulges, and also that disk survival/regrowth is a common phenomenon after bulge formation (30% of massive bulges live in disk dominated systems). I find, however, that pure bulges (B/T$>$0.8) are $\sim$ 30% larger than bulges embedded in disks at fixed stellar mass, and they have larger Sersic indices. This is compatible with a later growth of these systems through minor mergers.

The second part of the thesis focuses on the relation between morphological transformations and quenching. I found that the vast majority of (if not all) pure disks (B/T$<$0.2) in our sample lie in the main-sequence. While this does not discard the notion that pure passive disks exist, as observed in other works, it suggests that quenching without any bulge growth is not a common channel at least in the field environment probed by our data. Pure "blue" bulges (B/T$>$0.8) do exist however, suggesting that the formation of bulges happens while galaxies are still star forming. Intermediate B/T systems are both quenched and star-forming with similar abundances. I used these systems as a proxy to probe how quenching takes place within galaxies. At fixed stellar mass, bulges in star-forming galaxies are found to be 30% larger than bulges in quenched systems. Regarding the disks no systematic difference is measured. This can be interpreted as a sign that galaxies experience an additional morphological transformation during or after quenching. However, this result is not free of progenitor bias. Observed bulges in passive galaxies for a given epoch are more compact because they arise from a population of bulges in star forming systems that quenched, few Gyrs back and therefore were more compact.

In order to put more precise constraints on the formation timescales of bulges and disks I analyzed the resolved U,V,J colors of internal components. This is the first time this has been carried out up to z$\sim$2 to our knowledge. I found that almost all galaxies in our sample present negative color gradients. Bulges are always redder than the disks in star-forming galaxies at

all redshifts and their UVJ colors are compatible with them being passive, although they more likely to populate the dusty region than purely passive systems. This is compatible with a scenario of inside-out quenching put forward by previous works. However, rejuvenation through disk accretion could lead to similar signatures. Discriminating between the two possible processes requires a more robust estimate of ages. For that reason I extended the analysis to the SHARDS survey, a deep NB imaging survey (24 filters that cover the spectral range of 500-950 nm) of the GOODS-N field.

Résumé

Les galaxies passives présentent des morphologies et des propriétés structurelles différentes, que les galaxies, avec masse similaire, formant des étoiles. La preuve d'une distribution bimodale dans les relations taille - masse, couleur - magnitude, taux de formation d'étoiles (SFR) - masse suggère l'existence de deux populations de galaxies, mais aussi un lien entre le processus de quenching et les structures des galaxies; à savoir la présence et/ou la croissance d'un bulbe. Comprendre les mécanismes et la chronologie de la formation du bulbe s'avère fondamental pour comprendre l'origine de cette corrélation. Les bulbes grossissent-ils au cours de la séquence principale? Les galaxies ré-accrétent-elles un disque formant des étoiles? Les galaxies cessent-elles leur formation d'étoiles à partir des régions internes? et ainsi de suite.

Répondre à ces questions de manière pertinente nécessite de résoudre les parties internes des galaxies à différentes époques. Grâce aux données de haute résolution en multi-longueur d'ondes fournies par CANDELS, j'ai réalisé une décomposition séparant le bulbe du disque à partir des courbes de brillance de surface de $\simeq$ 17.300 galaxies (F160W$<$23, 0$<$z$<$2) dans 4 à 7 filtres couvrant un intervalle spectral compris entre 430 et 1600 nm. Le défit d'une telle analyse se trouve dans le choix d'un modèle à une seule or à deux composantes. Nous proposons une approche novatrice basée sur le deep-learning, nous permet de sélectionner à priori les meilleurs profils. La contamination par des mauvais ajustements ou des modèles non physiques produits par un profil secondaire est donc réduite. J'ai modélisé la SED (densité spectrale d'énergie) échantillonnée sur 4 - 7 points avec des modèles de population stellaires (BC03) de disques et de bulbes de manière indépendante afin d'obtenir les paramètres des populations stellaires (masses stellaires, couleurs). Cette procédure fournit un catalogue contenant à la fois les informations structurelles/morphologiques et les propriétés des populations stellaires d'un vaste échantillonnage de bulbes et de disques galactiques maintenant offert à la communauté (lerma.obspm.fr/huertas/form_CANDELS). Il s'agit du catalogue le plus grand et le plus complet décomposant le bulbe du disque galactique à des redshifts z$<$2.

J'ai utilisé le catalogue ainsi obtenu pour comprendre comment les galaxies cessent leur formation d'étoiles et pour déterminer l'impact que le quenching peut avoir sur les composantes internes. J'ai étudié la distribution des bulbes et des disques dans le plane taille - masse. La relation entre la masse et le taille est paramétrée avec une loi de puissance $r = A\, m^{\alpha}$. Les disques suivent une loi puissante avec une pente alpha de 0.2. Le paramètre de normalisation A augmente d'un facteur 1.2 jusqu'a z$\sim$2. Les disques, at z$\sim$2, ont une taille 30% plus petite q'aujourd'hui. D'une manière intéressante, la taille des disques ne dépendent pas de la morphologie globale de la galaxie mesurée par le B/T (le rapport entre la masse du bulbe et de la totalité de la galaxie). Les bulbes autrement, suivent une relation masse-taille avec un paramètre alpha ~ 0.5 et une dispersion intrinsèque de ~ 0.2. Le paramètre de normalisation augmente avec le redshift d'un facteur 2.5 jusqu'à z$\sim$2. Il est intéressant de noter que, à masse stellaire fixée, les tailles de bulbes ne sont pas aussi dependent de la morphologie. Ce résultat suggère une unique mécanismes de formation pour les bulbes massifs mais aussi que la survie ou la re-croissance du disque est un processus commun après la formation du bulbe (30% de bulbes massifs sont intégrés dans des galaxies-disques, B / T $<$0.2). Je trouve, toutefois, que les bulbes pures (B/T$>$0.8) ont des tailles 30% plus grandes que les bulbes contenus dans les galaxies à disque, et ont un indice Sersic également plus élevé. Ceci est compatible avec une croissance ultérieure tardive de ces systèmes par fusion de galaxies.

La deuxième partie de la these est concentré sur le lien entre la transformation morphologique et le quenching. La plus part de (sinon tout) les pure disques (B/T$<$0.2) vivre au long de la sequence principale dans le graphe SFR-masse. Bien que cela ne rejette pas la notion que les disques passifs purs existent, comme observé dans autres travaux, il suggère aussi que le quenching sans croissance de le bulbe n'est pas un processus commun, au moins dans l'échantillon analysée dans cette travaille. Pure "blue" bulbe (B/T$>$0.8) existent, suggérant que la formation des bulbes a lieux quand les galaxies sont encore formant étoiles. Les galaxies avec B/T entre 0.2-0.8 sont à la fois forment étoiles ou quenched. J'ai utilisé cette sélection comme proxy pour étudier comment le quenching act dans les galaxies. A masse fixée, J'ai trouvé que bulbes dans galaxies forment étoilés sont 30% plus grand que les bulbes dans galaxies que ont déjà arrêté la formation de nouveau étoilés. Concernant le disques, ils ne montre pas de difference entre le deux cas. Ces résultats peuvent être interprété comme un signe que les galaxies subissent une transformation morphologique supplémentaire pendant ou après le quenching. Pourtant, ils ne sont pas libre de l'effet appelé 'progenitor bias'. Les bulbes qui nous observons dans galaxies passive, dans une époque specific, sont plus compact parce que ils descendent d'une populations de bulbes

dans galaxies active que ont arrêté la formation des étoiles après, donc ils sont plus compact.

Afin de mettre des contraintes plus précises sur le temp de formation des bulbes et disques, J'ai étudié aussi le couleur U,V,J des composantes interne des galaxies. Il est la première fois que cette type d'analyse est fait sur une échantillon de galaxies jusqu'a z$\sim$2. J'ai trouvé que la plupart des galaxies ont négatif pente dans le couleur. La plupart des bulbes sont plus rouges que des disques dans galaxies encore formant étoiles au tout les époque. Leur couleur est donc compatible donc le définir passive, bien qu'ils occupe la région poussiéreuse. Cette scénario est compatible avec le modèle inside-out quenching proposée deja dans précédent travails. Néanmoins, rejuvenation pour l'accretion d'un nouveaux disque porte le meme signature. La connaissance des âges est à ce niveau nécessaire pour réellement contraindre ce scénario. Alors que le bulbe devrait être toujours plus vieux que le disque, la différence entre les âges pourrait mettre en évidence des galaxies en cours de rajeunissement. J'ai en ce sens élargis l'analyse en incluant de l'imagerie à bande étroite, SHARDS.

Contents

1 Introduction **17**
- 1.1 Brief history of the universe . . . 19
- 1.2 Statistical properties . . . 21
  - 1.2.1 Stellar Mass function . . . 21
  - 1.2.2 Mass-size plane . . . 22
  - 1.2.3 Star formation rate and stellar mass . . . 24
- 1.3 Galaxy evolution, morphology and quenching . . . 26
  - 1.3.1 How galaxies grow and die . . . 26
  - 1.3.2 Link between galaxy evolution and morphology . . . 30
  - 1.3.3 Mechanisms of bulge formation . . . 31
  - 1.3.4 Why studying bulges and disks . . . 33

2 Methods used in this work **35**
- 2.0.5 Morphological classification . . . 35
- 2.0.6 Surface brightness profile . . . 39
- 2.0.7 Stellar populations models . . . 41

3 Catalog of bulges and disks **43**
- 3.1 CANDELS Survey . . . 44
- 3.2 Modeling the surface brightness profile . . . 44
  - 3.2.1 Comparison with the literature . . . 47
  - 3.2.2 Limits on the bulge-to-disk decomposition . . . 48
  - 3.2.3 Uncertainties on the structural properties . . . 53
- 3.3 Selection of the best model . . . 59
  - 3.3.1 Brief introduction on machine learning . . . 59
  - 3.3.2 Profile selection with deep-learning . . . 61
  - 3.3.3 Reliability of the model selection . . . 66
- 3.4 Stellar masses of bulges and disks . . . 69
  - 3.4.1 Uncertainties on the SED analysis . . . 69
  - 3.4.2 Reliability of the mass . . . 72
- 3.5 Rest frame colors . . . 76

3.5.1 Uncertainties on the rest frame colors 76
3.6 Final catalog 76

4 Analysis of structural properties 81
4.1 Sample selection 82
4.2 Mass-size relation 82
4.2.1 Parametrization of the mass-size distribution 83
4.2.2 Mass-size relation of quenched and star-forming galaxies 84
4.2.3 Mass-size relation of bulges and disks 86
4.3 Bulges and disks in different morphologies 91
4.4 Effect of quenching on bulges and disks structure 96

5 Constraints on bulges and disks formation 103
5.1 Star forming main sequence 103
5.2 Colors as a proxy of the star formation activity 107
5.2.1 Comparison with CANDELS 111
5.2.2 Colors of bulges and disks 111
5.3 Discussion 112

6 Conclusions 117
6.1 On going work 120
6.1.1 Improving the SED analysis adding the SHARDS data 120
6.1.2 SHARDS survey 120
6.1.3 Method 120
6.1.4 Preliminary results 121
6.2 Future project 124

7 Appendix 127
7.1 Paper: A catalog of polychromatic bulge-disc decompositions of $\sim$ 17.000 galaxies in CANDELS 127

Acknowledgments 145

List of Figures

1.1 A time scale to compare the age of the Universe with redshift. 19
1.2 Stellar mass function . . . 21
1.3 Mass-size plane from van der Wel et al., 2014. . . . 23
1.4 Star forming main sequence . . . 25
1.5 SFR density across the time . . . 27
1.6 Stellar mass to halo mass ratio . . . 28
1.7 Environmental quenching . . . 29
1.8 Distribution of bulge-over total ratio in star forming and quiescent galaxies . . . 32
1.9 Surface density vs. stellar mass (Barro et al, 2015) . . . 32

2.1 Wolf classification . . . 36
2.2 Hubble classification . . . 36
2.3 Volume classification of galaxies . . . 37
2.4 Revised Hubble sequence by Kormendy & Bender 2012 . . . 38
2.5 Galaxy classification revised by Cappellari 2011 . . . 39
2.6 Sérsic profile . . . 40

3.1 Comparation between setups . . . 46
3.2 Uncertainties on 1-component fit . . . 49
3.3 Example of simulated galaxy . . . 50
3.4 SED template for galaxy simulation . . . 51
3.5 Comparison results from simulations . . . 52
3.6 Rescaling GALFITM errors . . . 54
3.7 Uncertainties in the derived structural parameters . . . 57
3.8 Uncertainties on the derived structural parameters in function of wavelength . . . 58
3.9 Example of the structure of a *neuron* . . . 60
3.10 Different machine learning approach . . . 61
3.11 Parameters range used for the profile selection . . . 62
3.12 Purity and Completeness of the selection method . . . 63

3.13 Examples of galaxies classified in the 4 types 65
3.14 Test of the model selection1 68
3.15 Test of the model selection 2 68
3.16 Distribution of the chi2 69
3.17 SED examples for different morphologies 71
3.18 Uncertainties on the mass estimation:1 73
3.19 Uncertainties on the mass estimation :2 74
3.20 The stellar mass and B/T with different wavelength coverage. 75
3.21 Distribution of the error on the rest-frame colors 77
3.22 Mass completeness of the sample 79

4.1 Mass-size relation star-forming-quiescent galaxies 85
4.2 Comparison of sizes distribution 87
4.3 Mass-size relation for bulge and disks in star-forming-quiescent galaxies 89
4.4 Evolution number density of bulges 91
4.5 Examples of galaxies with different B/T 92
4.6 Mass-size relation for bulges 93
4.7 Bulge sizes as a function of the redshift 95
4.8 Evolution of the median Sérsic index of the bulge 96
4.9 Mass size relation for disks 97
4.10 Disk sizes as a function of the redshift. 98
4.11 Mass size relation for bulges 99
4.12 Bulge sizes as a function of the redshift 100
4.13 Mass size relation for disks 101
4.14 Disks sizes as a function of the redshift. 102

5.1 SFR-mass plane 104
5.2 SFR-mass plane 105
5.3 Two color diagrams 108
5.4 Two color diagrams 109
5.5 Comparison between U-V, V-J and V-I rest-frame colors . . . 110
5.6 Color distributions of bulges and disks 113
5.7 Summary of the bulges and disks color in the UVJ/I plane . . 114
5.8 Color distribution of bulges and disks across the time 115

6.1 SHARDS filters 121
6.2 Example of the SED analysis 122
6.3 Example of SHARDS results 123
6.4 Distribution of disks in mass-size plane) 126

List of Tables

3.1 Order of the Chebyshev polynomial functions 46
3.2 Range of values used in the simulations 48
3.3 Results of the deep-learning classification on the real data . . 64
3.4 Mass completeness thresholds 78

4.1 Mass size fits results for star-forming and quiescent populations 84
4.2 Mass size fits results from van der Wel et al., 2014 84
4.3 Mass size fits results for bulges 88
4.4 Mass size fits results for disks 90

6.1 Results from the SED fitting on bulge and disk 122

Chapter 1

Introduction

The classification of galaxies into ellipticals, lenticulars and spirals (Hubble, 1929) is almost as old as the discovery of galaxies itself. (Harlow Shapley and Heber Curtis were still debating in 1920 whether the nebulae were extragalactic objects). Already in the first attempts of morphological classification it was known that galaxies are composed by a central dense core (bulge), surrounded by a flattened structure(disk). Humason [1947], discovered that morphological types correlate with spectral properties and thus with their stellar populations. Elliptical and lenticular galaxies are red because they formed the bulk over their stars in the first few billion years after the Big Bang and lack of short-lived blue massive stars. Spiral galaxies are mainly blue because, in most of them, the formation of new stars has not ceased yet (Sandage, 1986).

At the dawn of the new millennium, the field was revolutionized by the advent of large surveys. The Sloan Digital Sky Survey gave to the community $\sim$ 300′000 of galaxy spectra, shifting the main subject of study from the exploration of different morphologies to the analysis of stellar population and in particular on the galaxy color-bimodality which had been discovered thanks to the SDSS (Kauffmann et al., 2003, Baldry et al., 2004).

The advent of others survey as well as new facilities that extended the analysis on a larger range of frequencies from the UV, infrared to the radio, the recent introduction of the IFU facilities, open the possibility to improve such analysis. However the topic is still not completely solved. In particular the role of the morphology and its connection with the star formation history is still largely debated. While several works already suggested the existence of a correlation between the morphology and the star formation activity (Wuyts et al., 2011, Huertas-Company et al., 2015, Whitaker et al., 2016) the link between the growth of the central bulge and the quenching is still not well understood. Are galaxies decreasing the SFR a cause of the presence of the

bulge? are they growing the central density already on the main sequence? what are the main channels of bulge and disk formation? is the quenching affecting their properties? do galaxies start to quench from the inside? these are the main questions that motivates this work. Proper answers require to explore the morphology of galaxies as well as to resolve properties of their internal components.

The thesis is organized as follows: in the next chapter I will give a brief introduction on the state of art on galaxies properties as well as theory of galaxies formation and evolution, to then introduce the main topic of the work. In chapter 3 I present the morphological catalog of bulges and disks. In the two following chapters I use such catalog to investigate the connection between the morphology, presence/growth of the bulge and the star formation activity of the host galaxies. Firstly I analyzed how the bulge and disk structure change in different morphologies to put constraints on their formation mechanisms (chapter: 4). Then I studied the effect of the quenching comparing bulges and disks in star forming and quenched systems. Finally I explored the distribution of the color to put constrains on the quenching process (chapter: 5).

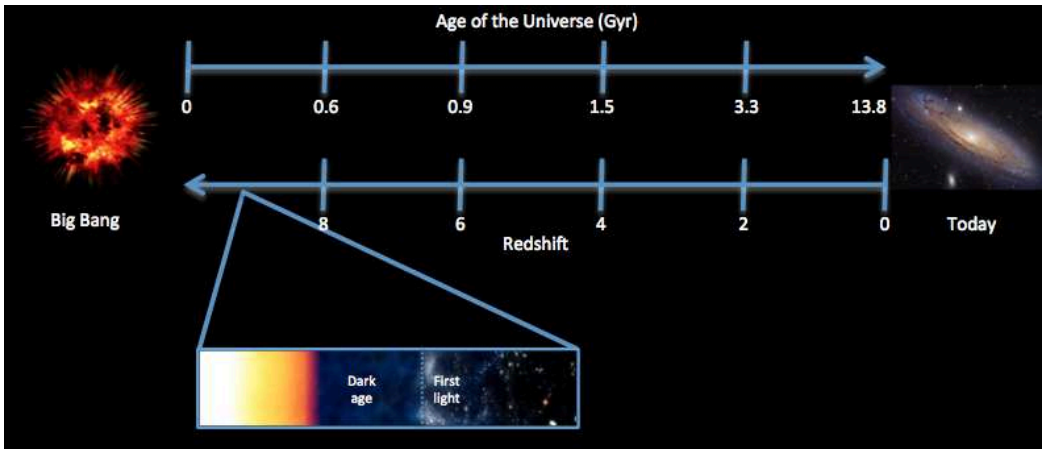

Figure 1.1: A time scale to compare the age of the Universe with redshift.

1.1 Brief history of the universe

"Our own existence, after all, is due to those slight imperfections existing in the primordial universe". [Balbi]

In 1929 Hubble discovered that almost all galaxies are moving away from us. A direct interpretation of that is the expansion of the universe. If it is undergoing an expansion phase now, it has to be more dense and hot in the past. Due to the timescale of the universe's life, we cannot observe its evolution, we can just measure indirect proofs of it. The combination of the finite speed of light, and the fact that the expansion 'stretches' the wavelength of the photons, until they reach our telescope, gives a measure of the distance but also an estimate of the time at which photons were emitted. Looking far away, allows us to explore the past.

In the 1965, Penzias & Wilson, discovered a residual signal at radio wavelengths, initially identified as background noise. This was the first detection of the *Cosmic microwave background* (CMB). The existence of this background signal was predicted almost in the same years by Gamow, Alpher and Herman, as a proof of *the Big Bang theory*. The first mission space that measured the microwave background was COBE satellite (Smoot et al., 1992), followed by WMAP (Bennett et al., 2013) and then recently by the Planck mission (Planck Collaboration et al., 2014). The analysis of the signal revealed that the CMB is well fitted by a blackbody spectrum with a temperature of 2.725 ± 0.001 K, with relative anisotropy of $\frac{\delta T}{T} \sim 10^{-5}$, at the angular scale of $\sim 1°$. These fluctuations of temperature probe density

fluctuations that are at the origin of the formation of galaxies. The understanding of the origin of this signal brings informations on how the universe evolves until today. In its early stage the universe appears highly homogeneous and permeated by a mixture of plasma and radiation. The very high temperature and density prevent the formation of the atoms and the photons cannot freely scatter. Thanks then to the expansion, the temperature decreases and the universe becomes progressively transparent. The baryonic component of the universe goes from being ionized to being neutral, passing through the epoch of the recombination. Consequently the ratio of photons interaction decreases until the time between collisions became longer then the Hubble time. This is the definition of the surface of the last scattering. The time at which a typical CMB photon underwent its last scattering to then freely streaming through the universe. The study of this signal is particularly interesting since it provides a snapshot of the universe at that time, allowing us to study the primordial fluctuations which initiate the growth of the large scale structures that we can observe today.

Currently, the most widely accepted cosmological model used to describe the evolution of the structures is the ΛCDM (Ostriker & Steinhardt, 2003, 1995). Λ represents the dark energy, hypothetical force that is accelerating the expansion of the universe. CDM is the acronym for Cold Dark Matter. It is made by cold slow moving particles that do not emit electromagnetic radiation since they do not interact with photons. Thus it is invisible/dark matter that can be revealed only through its gravitational effects on the visible matter. The new measurements from Planck have shown that the $\sim 27\%$ of the Universe is composed by dark matter, while the visible one covers only $\sim 5\%$. The rest is dark energy. *'We cannot claim to understand the evolution of structure in the universe, if we do not know the nature of the dark matter and how it fits within our models of fundamental physics'.* (Ostriker & Steinhardt, 2003)

Without this additional component, the universe would have remained too uniform to form galaxies, stars and planets. Indeed, just after the Big Bang, the universe was hot, dense and essentially homogeneous. Due to the high temperature and the photon scattering, the baryon fluctuations could not grow before the recombination era. Despite of that, since the dark matter does not interact with the ordinary matter, the radiation could not prevent its gravitational collapse, forming clumps of dark matter . The halo will then keep accreting mass through gravitational interactions between structures or merging. This hierarchical evolution is called *bottom-up*. Small structures form first, while larger structures form later,.(Springel et al., 2005). The growth of the dark matter structures simultaneously drives the accretion/formation of baryons structure through gravitational collapse into the

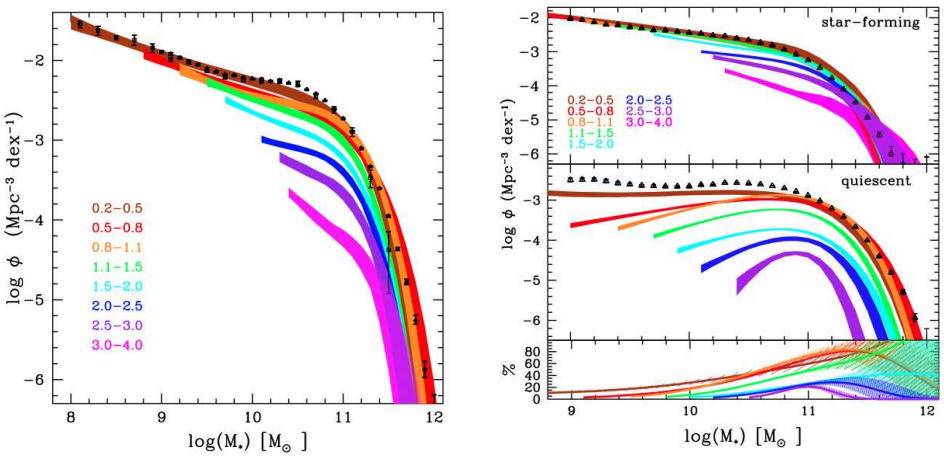

Figure 1.2: Stellar mass function for galaxies up to z = 4 using the VISTA survey. Right panel: stellar mass function for the star-forming and quiescent population. (Ilbert et al., 2013)

dark matter potential. The accretion of density turn on the early star formation in the centre of dark matter halos. First step towards the formation of galaxies.

1.2 Statistical properties

In order to analyze galaxies, statistical properties and scaling relations are commonly used. In this section I introduce some someone of them that are useful in the understanding of this work.

1.2.1 Stellar Mass function

The stellar mass function is defined as the number of galaxies at a given mass M in a unit of volume. The most used parametrization is the de Schechter (1976) function:

$$\phi(M)dM = \phi^* \left(\frac{M}{M^*}\right)^{\alpha} e^{-\left(\frac{M}{M^*}\right)} dM \tag{1.1}$$

where M_* is the characteristic mass, α the slope of the function and ϕ_* the normalization factor. This relation is widely studied in literature as a good tracer of the mass assembly across the time. Accretion that is believed to be the result of a combination of mechanisms, such as the star formation

from in-situ or accreted gas, or through gravitational interactions like major/minor mergers. Combining the evolution of the stellar mass density with the integrated star formation across the cosmic time provides a scenario on how galaxies evolve. However the agreement between them is still debated, due to the uncertainties on the contribution of low/high mass galaxies at $z \sim 2$. In particular, while the stellar mass density increases with cosmic time, no strong evolution is measured at the high mass end (Pérez-González et al., 2013). Moreover, the stellar mass density of quiescent galaxies does not show a strong evolution between $1 < z < 0.1$ (Ilbert et al., 2010) while it increases of one order of magnitude at $z > 1$ (Ilbert et al., 2010, 2013). It means that the quenching of star forming galaxies must be extremely efficient at this time, even though the peak of star formation is predicted to be at $z \sim 2$ (Madau & Dickinson, 2014). Ilbert et al. confirm the lack of evolution at the high-mass end for quiescent galaxies at $z < 1$, while a clear flattening of the slope, found at low masses, probably due to the addition of new quenched galaxies. Result that reflect the need of mechanisms to control and to decrease the star formation in this range of masses.

However, the stellar mass density function cannot disentangle which mechanisms are acting during the quenching process. The study of the mass contribution of the different morphologies will give hints on how galaxies are undergoing to a morphological change. A first attempt was done by Fontana et al. [2004] and Bundy et al. [2005]. They found that the early type massive galaxies weakly evolution of from $z \sim 1$ to the present. A further analysis on the abundance of different morphologies was done by Huertas-Company et al. [2016]. They found that, most of the star forming galaxies in the local universe appear as a regular disk systems, while only a small fraction show an irregular shape. Moving to earlier epochs the two abundances are inverted. The strong reduction of the irregulars suggests that a morphological transformation happened across their evolution. The quiescent population, at low redshift, is dominated by two morphological types, spheroids and bulge+disk systems, while the latter class becomes irrelevant at larger value of z.

1.2.2 Mass-size plane

The mass function statistically quantifies how galaxies are accreting mass. However, complementary effects of this accretion/evolution are reflected on galaxies properties. Exploring the relation between masses and sizes, for different galaxy types can give hint on possible different evolutionary paths or accretion processes. The existence of a correlation between these two quantities is already a sign that galaxies are assembling their masses following an ordered path, as predicted by the cosmological model. Shen et al. (2003)

demonstrated that the two main class of galaxies show a different relation between the mass and the size, in the local universe. van der Wel et al., 2014 show that this bimodality is still in place up to $z \sim 2$. The sizes of late type galaxies show a weaker dependence with mass, while the relation is significantly steeper for the early types. Similar results are found also at higher redshift (van der Wel et al., 2012, Whitaker et al., 2012, 2016), confirming that the two main class of galaxies follow different mass-size relations at all epochs but also that early type galaxies are always more compact than the later type (e.g. Daddi et al., 2005, Bernardi et al., 2010, Trujillo et al., 2007, van Dokkum et al., 2008).

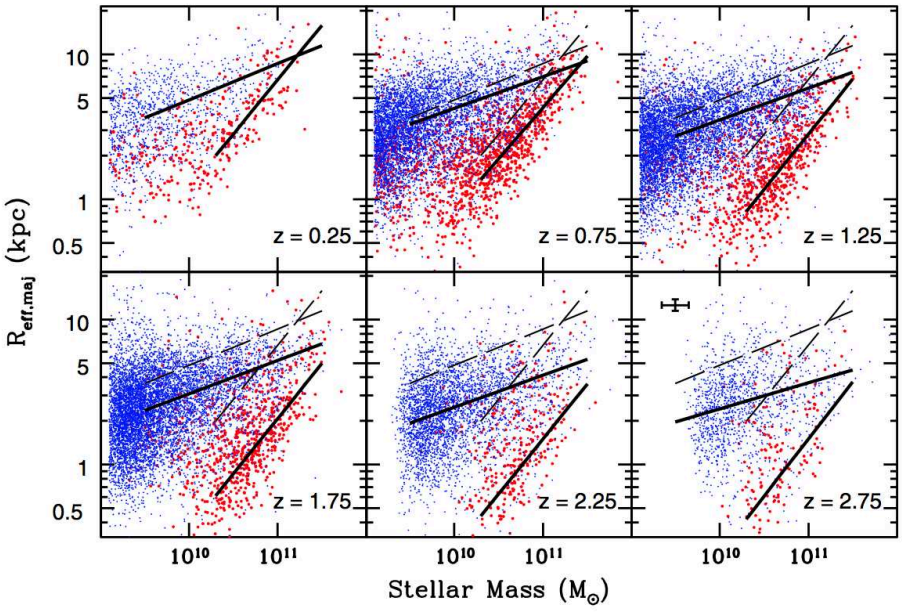

Figure 1.3: Mass-size plane for early (red) and late (blue) type galaxies from van der Wel et al., 2014. Black lines are the best fit relations. In each bin is reported the relation at z=0 (black dashed line) as comparison.

Such evolution can be explained since galaxies are formed by gravitational collapse of the baryons in the dark matter halo. Hence under a set of assumptions their size evolution is expected to be proportional to the Hubble time (see Mo,Mao and White, 1998 and Bryan & Norman, 1998 for more details and demonstrations). While this trend is predicted and confirmed by observations (Trujillo et al., 2006, van der Wel et al., 2012, 2014) for the late type galaxies, the interpretation of the steeper size evolution of the early type population is still debated. Some works pointed out how the measurements can be underestimated due to selection effect or limit of the method

(van der Wel et al., 2009, Mancini et al., 2010). The surface brightness dimming, especially at high redshift, could affect the estimation of the flux in the outskirt, while the mass can be affected by uncertainties on SED fitting. However analysis done using the dynamical masses, confirmed the existence of compact galaxies at high redshift (van Dokkum et al., 2008, van de Sande et al., 2011).

Despite of that, the interpretation is still debated, since the evolution of the median size of the massive population could be not driven by individual growth, but by the addition of newly quenched galaxies at different epochs (progenitor bias effect, Carollo et al, 2013,Lilly & Carollo, 2016). While some works claim that this solution is incompatible with the observations (van der Wel et al., 2012), others are arguing that in this case we should observe a sample of similarly compact galaxies at low z (Poggianti et al., 2013). The absence or the small fraction of this kind of objects in the local universe (SDSS fields)(Trujillo et al., 2009, Taylor et al., 2010), leave space to different interpretations.

Zanella et al. [2016] investigate the relation between the age and the mass-size relation, to estimate the contribution of the new galaxies in the quenched sample, concluding that the dependence is really shallow. This is not excluding the progenitor bias hypothesis, but it is suggesting that the dominant contribution comes from the increase of the individual sizes, in agreement with Belli et al. [2014] .

1.2.3 Star formation rate and stellar mass

Galaxies lie in an equilibrium between gas that is accreted and converted into stars, and a fraction of it that is then ejected and recycled. Consequently the Star Formation Rate (SFR) is linked to the accretion rate.

This is indeed reflected in the existence of the "main sequence" (MS), region in the (SFR) - mass plane where the star forming galaxies are concentrated (Brinchmann et al., 2004, Salim et al., 2007). The presence of this relation can be interpreted as self-regulation of the galaxy in forming new stars. It suggests that the star formation history of a galaxy is preferentially driven by regular mass dependent processes, like gas accretion, instead of stochastic events as mergers. The distribution of galaxies in the mass-SFR plane shows also the existence of a second class of objects, specially concentrated at the high mass end of the plane, with values of star formation several orders of magnitude lower than the ones in the main sequence, the so called quenched population. This duality in the distribution is observed up to higher redshifts (Elbaz et al., 2007, Daddi et al., 2007, Huertas-Company et al., 2015, 2016, Wuyts et al., 2011, Whitaker et al., 2012, 2014).

Many works focused the analysis on the star forming population (Tasca et al., 2015, Whitaker et al., 2012, Tomczak et al., 2016) all finding an evolution of the main sequence with time. The evolution of the zero point of the relation is the result of an overall increase of the SFR across time. Galaxies at high redshift are more "active" in producing stars than their lower z counterparts of similar stellar mass. This trend can be related to a different efficiency of the galaxies in converting gas into stars or simply due to smaller gas fractions in low redshift galaxies (Genzel et al., 2012, Daddi et al., 2010, Tacconi et al., 2010), or a combination of both.

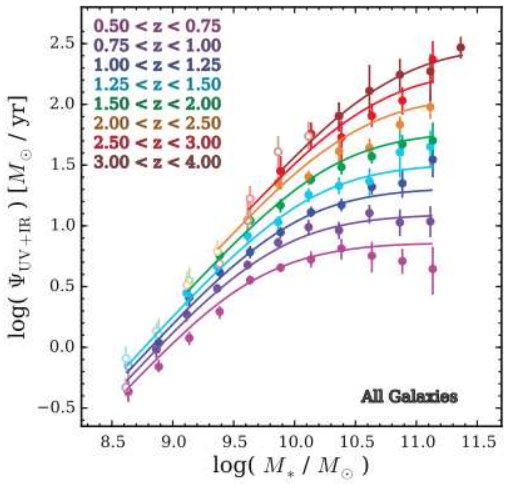

Figure 1.4: Redshift evolution of the star forming main sequence. Points are the stacked measurement in bin of mass. Lines are the result of the best fit. Analysis done for galaxies from the ZFOURGE survey (Tomczak et al., 2016).

Furthermore, a second key result from the analysis of the main sequence consists in the evidence of a variation of the MS slope at the massive end. Possible interpretation of this effect is in an increasing of the fraction of galaxies deviating from the MS since they are decreasing their SF activity. This is what is called "quenching". Taking into account also that passive galaxies tend to appear with early-type morphologies while the star forming one are more disk dominated systems (e.g Wuyts et al., 2011, Whitaker et al., 2012, Huertas-Company et al., 2015, 2016), a second explanation can be found in the link between the morphology and the SF activity. The growth of a central density/bulge could be a possible (Whitaker et al., 2014, Barro et al, 2014) explanation for the evolution between the two class of galaxies. Therefore, if the presence of the bulge is the cause of the quenching or only the direct consequence is still debated. It is also not clear how common is the

rejuvenation process (Fang et al., 2013, Mancini et al., 2015). This point is still under discussion since to be properly tested requires an accurate analysis of the integrated properties of galaxies, but also of their internal components.

1.3 Link between galaxy evolution, morphology and quenching mechanisms

The global picture for galaxy assembly is well constrained by the CDM model. However understanding how they evolve and assemble their mass is one the topic still largely debated in the literature since it reveals how much we already know but also how much still need to be explored.

1.3.1 How galaxies grow and die

The main activity of a galaxy can be schematically resumed in the conversion of gas into stars. Indeed the more gas they have, the more stars they form. A proof of that is in the relation between M_* and the SFR. Despite of that they are not as "efficient" as initial models predicted. Indeed studies of the cosmic star formation rate density (Madau & Dickinson, 2014) reveal that galaxies around 8-10 Gyr ago were forming stars with higher rate than today. The measurement of the star formation activity per volume unity, shows a peak of star formation activity at z = 2 followed by a gradual decline to the present day. Key point is then in the understanding of the physical processes that are responsible of the regulation of the star formation in galaxies but also of its decrease across the time. Many works/simulations tried to match the evolution of the stellar masses and star formation rates of galaxies. The result is an overestimation of star formation activity that proved the need of additional internal mechanisms to regulate and suppress such excess.

The presence of the main sequence can be interpreted as self-regulation of the galaxy in forming new stars. It suggests that the star formation history is preferentially driven by regular mass dependent processes instead of stochastic events (Brinchmann et al., 2004, Daddi et al., 2007). This is supported also by the correlation between the surface gas density and surface SFR (the Schmidt-Kennicutt law, Schmidt, 1959, Kennicutt, 1998), that point to prefer a secular smooth process in triggering the star formation then mergers. The infall of cold gas from the cosmic web structure (Dekel et al., 2009) is a possible explanation. Direct detection of infalling gas still remains ellusive. An alternative approach towards understanding assembly and star-formation efficiency is in the match between the mass of the halo with the stellar mass. While the build up of the dark matter halo is quite

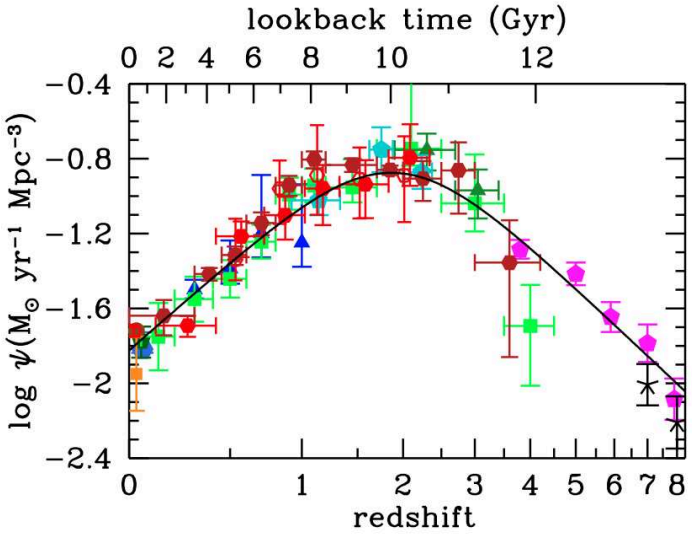

Figure 1.5: The evolution of cosmic SFR density across time from the review of Madau & Dickinson, 2014.

well simulated using the today accepted cosmological model, the assembly of baryons requires the introduction dissipative processes, to match prediction with observations. The combination of the knowledge of the galaxy-halo connection with the mass accretion and merger histories of halos at different epochs allows to constrain the stellar mass assembly in galaxies over cosmic time. One of the most common method used is the abundance matching. This technique allows to connect dark matter halos with observed galaxies trough a one-to-one relation between luminosity and dynamical mass. More luminous galaxies are assigned to more massive halos.

Figure 1.6 shows a recent result from Behroozi et al. [2013] obtained by the implementation of this method. The stellar mass fraction peaks for halo mass of $\sim 10^{12} M_{\odot}$ where the baryon conversion has the maximum of the efficiency (this is the case of Milky Way like galaxies), to then drop at higher/lower masses. However also in the maximum the barion fraction is lower then what is expected, meaning that not all the gas present in galaxies is converted into stars. This is again an evidence of the need of processes (feedback) acing to inhibit the star formation.

One possiblie explanation resides in the theory of the thermal shook heating introduced by Dekel et al., 2009. The decrease is a consequence of the transition between two regimes : i) the cooling time of the infalling gas is much shorter than the compression time. The gas radiates faster than is compresses, thus it remains cold while it is accreted. This condition allows the

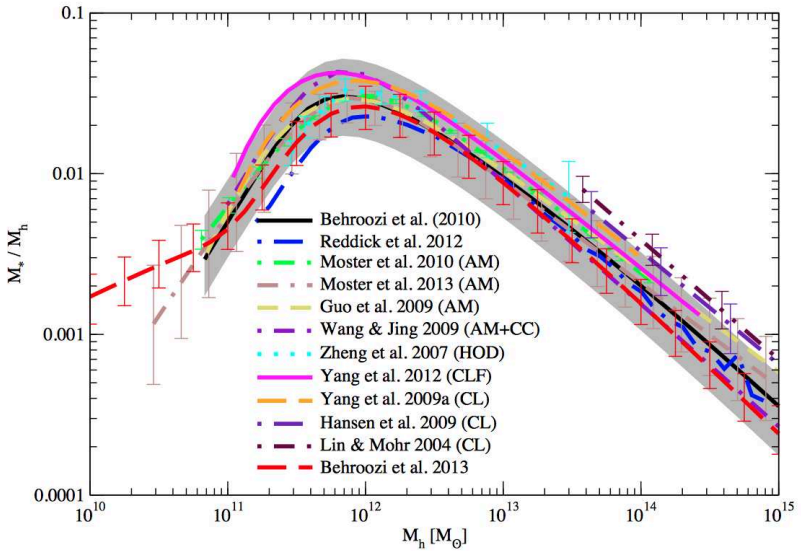

Figure 1.6: Stellar mass fraction in function of the halo mass. Comparison between best-fit results for the stellar mass to halo mass ratio at z = 0.1 done using abundance matching, with previous models and observations (Behroozi et al., 2013).

gas to reach the center of the galaxies to consequently trigger the formation of stars. ii) the cooling time is much longer than the compression time scale. The gas is shock heated. The thermal pression then avoids its accretion into the central core of galaxies. The transition between the two cases is related to the mass of the halo. When it reaches $M_h > 10^{12}$, the infalling of new gas is halted. The shock-heated gas is then kept hot due to feedback from some energetic source, like AGN (Cattaneo et al., 2009). While this regime can explain the drops for massive halos, in the lower mass range the supernova feedback is the dominant effect. Indeed the supernova explosion may provide enough energy to drive galactic winds and outflows in less massive galaxies ($M_* = 10^8, 10^{10} M_\odot$), to expel the gas and reduce the star formation rate.

However internal feedback are possible explanations, they cannot fully explain the quenching of the star formation. Why and how a galaxy moves from the star forming main sequence to the passive region, becoming *red and dead* requires additional processes. Understanding why a galaxy stops to forms stars is obviously related on how stars are 'formed'.

The formation of stars happens inside of rich clouds of gas, where temperature and density are high enough to break the equilibrium. Such equilibrium is a compromise between the rotation, the gravitational force and the thermal pressure. Once it is broken the gas, guided by the gravitational force,

will collapse until it will reach the right temperature and density to activate nuclear reactions. Hence the decreasing of the SFR has to be investigated in the lack of gas, or better in the absence of the required conditions for the formations of stars. There are three possible solutions, removing the gas, make it less dense/hot or inhibit the accretion of new gas from the cosmic web.

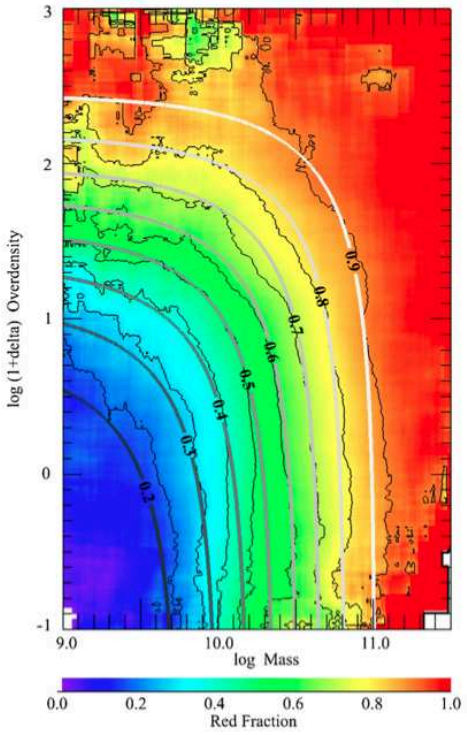

Figure 1.7: Fraction of red galaxies as functions of stellar mass and over density in SDSS (Peng et al, 2010.

Gravitational interactions between galaxy-galaxy or galaxy-cluster, can produce relevant lost of gas due to the ram pressure stripping (Gunn & Gott, 1972), viscous stripping (Nulsen, 1982), thermal evaporation (Cowie & McKee, 1977), harassment (Moore et al., 1996). All these mechanisms are relevant for galaxies in group or clusters (Quilis et al, 2017) and represent different actions of what is called the *environmental quenching*. The mass of the halo (*halo quenching*) also can play a significant role, causing a thermal shock. Once the accretion of new gas is halted, the galaxy, still producing new stars, will consume its internal gas content to slowly quench. This is the strangulation or starvation effect (Peng et al, 2015). Peng et al [2010] found that the fraction of red and passive galaxies is independent of the density at high mass. If the environment is guiding the shooting down of the SFR, also in this mass range, a correlation is expected. The dependence of the passive fraction with the mass suggests the presence of an additional mechanism, called the *mass quenching* related to internal physical processes. Alternatively, mass and environment quenching can be interpreted as two effect of a single physical mechanism, since they have the same effect on the morphology (Carollo et al, 2014, Knobel et al., 2015).

Though, feedback from supernova explosion or the presence of active galactic nuclei (AGN), are both candidates as internal mechanisms acting to affect the budget of gas within the galaxy. The resulting wind, in both cases,

will produce outflows of gas that can have a double effect. It will remove the gas but at the same time it will compress it, increasing the temperature and the density. It will trigger the star formation activity on the short time scale, but it will cause the quenching later. Furthermore, the AGN activity is found to increase strongly with galaxy mass (Rodighiero et al., 2015,Fiore et al., 2008), especially at $z \simeq 1$, in agreement with the idea of mass quenching.

The last effect that should be added to the quenching scenario is the *morphological quenching*. This mechanism is based on the assumption that the growth of the bulge correlates with the decline of the SFR activity. The accretion of a central density, stabilizes the disk, preventing it to fragment into dense clumps and to do not reach as high densities as it is required to form stars (Martig et al., 2009, 2013).

Summarizing, there are many mechanisms that can explain the existence of the duality in the galaxy properties, and that can affect the star formation activity of a galaxy, but their real contribution is still debated.

1.3.2 Link between galaxy evolution and morphology

Eggen, Lynden-Bell & Sandage [1962] were the first to propose a theory for the origin of galactic morphologies. Their work was focused on the Milky Way but could reasonably be generalized to other galaxies. In their picture, galaxies formed through monolithic collapse of large spheres of gas. The gas that made stars very rapidly (on a timescale shorter than the free-fall time) collapse, to firstly form the bulge component (the entire galaxy in the case of an elliptical galaxy), which is denser since reflects the higher density of the Universe at high redshift (Gott & Thuan, 1976), and afterwards on longer timescales it forms the disk component. This model faced two main problems. It predicted that giant elliptical would be rotation ellipsoids with disky isophotes (Larson, 1975) and could not explain their triaxiality/isophotal boxiness. Moreover it did not fit naturally in the hierarchical cold-dark-matter scenario of structure formation, in which the smallest structures collapse first and then merge into larger ones.

In the same years, Toomre & Toomre [1972] demonstrated that major mergers can transform disk galaxies into spheroidal systems with structural properties consistent with those of observed elliptical galaxies. For this reason, the merger model became the standard picture to form bulges in semi analytic models of galaxy formation in a cosmological context (Kauffmann et al., 1993, Baugh et al., 1996). In this scenario spiral galaxies with prominent bulges were explained as merger remnants that had the opportunity to regrow a disk.

However this scenario, with a unique channel for bulge formation, was

not able to reproduce the variety of observed bulges, in terms of mass ratio. Most of the predicted galaxies either had a massive bulge or had no dense core at all. Namely, the majority of disks were predicted to be bulgeless. Particularly for systems with masses comparable to that of the Milky Way or lower. This motivated van den Bosch [1998] and Hatton et al. [2003] to look at disk instabilities as an alternative channel for bulge formation, introducing already the idea of bulge growth within the disk. Most current semi-analytic models contain both channels (Knebe et al., 2015 for an overview).

1.3.3 Mechanisms of bulge formation

Quiescent galaxies are more compact than star forming one (van der Wel et al., 2014), as well as most of the passive galaxies have a spheroidal structure while disks tend to be star forming (Wuyts et al., 2011). This bimodal distribution is reflected in most of the scaling relations (like color-magnitude, M_* -SFR, etc), and reveals that two galaxy populations exists up $z \sim 3$ (Whitaker et al., 2012, 2014, Huertas-Company et al., 2016). Moreover Bruce et al. [2012] show that the majority of the star forming galaxies have a disk dominated profile, while passive are mostly bulge dominated systems. However it does not discard the existence of passive disk and star forming bulge dominated systems (e.g. Bruce et al., 2012, Lopes et al. (2016),Toft et al. (2017)). This set of correlations underly the link between the mass assembly and the building of internal components, but also the connection between the quenching and the presence of the bulge.

The increasing number of observed star forming galaxies with a dense stellar core (Wuyts et al., 2011, Barro et al, 2016, 2015) suggests a scenario in which galaxies starts to grow the bulge while in the main sequence. Indeed Lang et al [2014] found an increase of the bulge fraction (B/T) along the main sequence (figure 1.8, see also Bluck et al., 2014).

A possible explanation of that is the "in-situ" growth of the central density. Disks are rich of gas, but they are also unstable and turbulent, mainly at high redshift (Kormendy, 2015). This condition increases the probability of having events of violent disk instabilities and the consequently formation of new clumps. They can then migrate to the center accreting a dense core of stars. The presence of a central density will stabilize the disk, avoiding the formation of new star forming clumps. Consequently the galaxy will quench (Bournaud et al., 2014, Bournaud, 2016). This theory is supported by the increasing number of clumpy and irregular galaxies at high redshift (Huertas-Company et al., 2015).

Recent high resolution cosmological simulation proposed a different possible path for which quenched galaxies are the results of a ‘wet’ compaction.

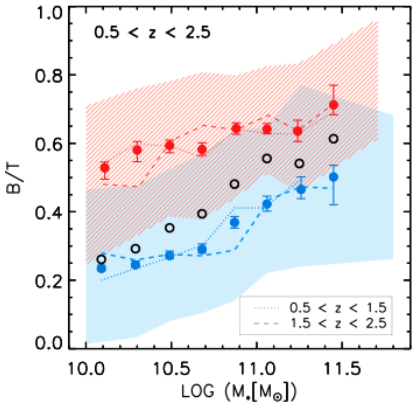

Figure 1.8: Distribution of bulge-over total ratio in star forming and quiescent galaxies in the redshift range of $0.5 < z < 2.5$ in the CANDELS field (Lang et al, 2014)

A star forming gas-rich disk passes trough a sequence of compacting events, like gravitational instability and contraction or minor/major merger. After this phase the galaxy is compact but still star forming, what is called 'blue nugget'. The depletion of new gas in the center by feedback or the absence of further gas inflow due to the thermal shock, will lead the galaxy to start to quench in the central region. (inside-out quenching Tacchella et al., 2016). Once the galaxy definitively ceases the star forming activity will move in the quiescent region as "red nugget" (Dekel et al., 2009, Zolotov et al., 2015, Tacchella et al., 2017).

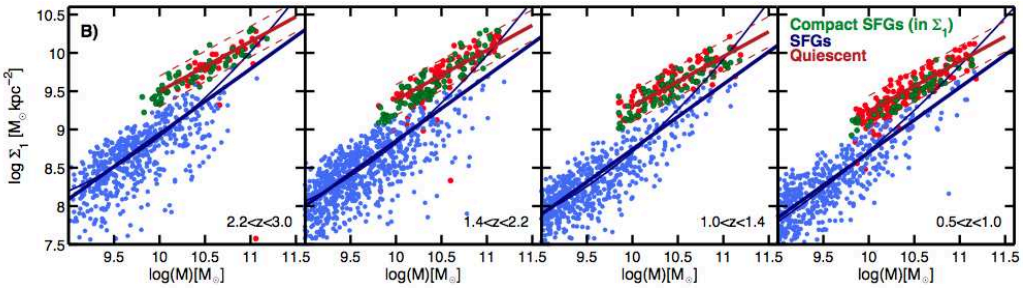

Figure 1.9: Surface density vs. stellar mass for galaxies in the CANDELS/GOODS-S (Barro et al, 2015). $\Sigma 1$ is the surface density within 1 kpc. Blue and red points are respectively star forming and quiescent galaxies. Green point are compact star forming galaxies that show high surface densities similar to those of quiescent galaxies.

Barro et al, 2015 show the correlation between the SFR and the cen-

tral density Σ_1 (where Σ_1 is the density in mass within 1 kpc radii). Star forming and quiescent galaxies follow a different relation in this parameter space. Despite that there is an evidence of a group of dense star forming galaxies (possible *blue nuggets*) with structural properties comparable with the passive population. This is a possible signature of a compaction phase that preceded the quenching. (Barro et al, 2015, Whitaker et al., 2016).

In between the star forming and quiescent regions, there is the 'green valley' with very few galaxies. Are they late-type galaxies being quenched (Schawinski et al., 2014) or early-type galaxies that are experiencing sort of 'rejuvenation', re accreting a star forming disk component? (Fang et al., 2013, Mancini et al., 2015)? Rowlands et al. [2017], claim that to explain the number density of the various populations, a unique way path is not physically reasonable but it requires the contribution of galaxies that may have been rejuvenated. This different approach gives an alternative or complementary explanation on the existence of star forming galaxies hosting a compact central region.

1.3.4 Why studying bulges and disks

The life of a galaxy is a trade off between process that act to trigger or halt the star formation activity. Many processes as well as various models are proposed to explain that scenario, as already discussed in previous sections. However how a galaxy evolves and assembles its mass is strictly linked to the way its internal components are built. Moreover the different mechanisms or combination of processes that are acting to drive its evolution, could leave an imprint on the structure of the galaxy as well as on its internal components. For that reason understanding the link between the quenching process, star formation activities and the morphology requires to resolve properties of bulges and disks. This is the main goal of this work. I want to investigate how bulges and disks form and evolve in different morphologies, as well as how their presence affect the properties of the galaxies. Moreover I will explore the correlation between the growth of the bulge and the decrease of SFR. Are all bulges/disks quiescent/star forming? are their structures similar in star forming and quiescent galaxies?

Many works already studied properties of bulges and disks (Lang et al, 2014, Bruce et al., 2014, Morselli et al., 2017). However this work differs from previous analysis for three main reasons. Firstly the models are done using simultaneously 4 to 7 bands from the CANDELS survey, thanks to the software GALFITM . In addition of that, since a challenge in this kind of analysis is in the selection method, in this work we used a new approach based on deep-learning to estimate the optimal model that should be used to

fit the light profile. Finally the catalog presented in this work is the largest one containing bulges and disks properties.

Chapter 2

Methods used in this work

In this chapter I introduce different methods that are used to obtain the results presented in this work.

2.0.5 Morphological classification

Historically, the first classification was done by Wolf 1908. It was the first attempt to distinguish the different morphological types, starting from objects that appear amorphous and less resolved (type g), to galaxies that show a clear central density and structured spirals arms (type r to w) (see figure: 2.1). Galaxies, indeed, are generally composed by two internal components. The central core, called bulge, is characterized by a spheroidal structure. It is surrounded by a flattened region, usually denominated as the disk component. Hubble (1926) proposed a more accurate classification still used today, based not only on the apparent shapes of galaxies but also on the presence and the strength of internal components. He defined two main classes : early type and later type galaxies (see figure2.2). The first group contains ellipticals and lenticulars galaxies, while the second one all the variety of spiral galaxies. Elliptical galaxies characterized by a central elliptical bulge, without a disk component. They are divided as a function of their ellipticity. There are eight subgroups from E0 to E7. The numbers that follow the E are determined by multiplying ten times their flatness : $n = 10 * (a - b)/a$, where a and b are respectively the semi major/minor axes identified by the projection of the galaxy shape on the ideal plane of the sky. Spiral galaxies are composed by a central spheroidal density, the bulge and an external disk characterized by spiral arms. Observationally this class of galaxies is divided between objects that show or not a central bar, called respectively spiral (S) and barred spiral (SB). Each branch of the sequence is then divided in subgroups, from a to c, as a function of the ratio between bulge

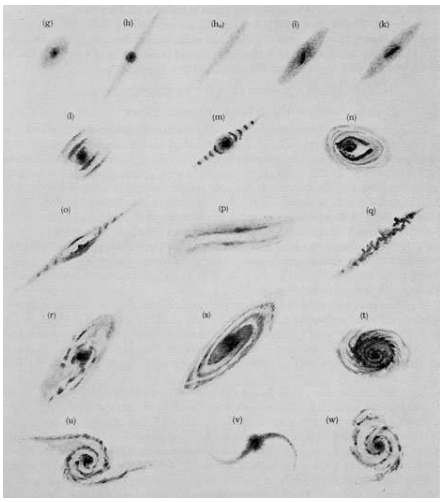

Figure 2.1: Galaxy classification from Wolf 1908. From the top to the bottom galaxies are ordered from amorphous forms to the one that clearly shows spiral arms.

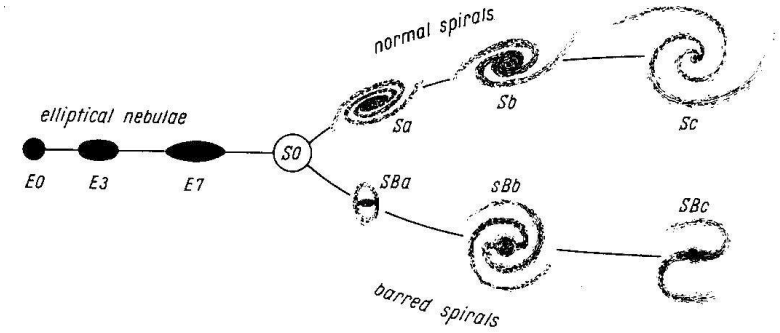

Figure 2.2: Hubble classification, also called 'Tuning Fork' (Hubble, 1936).

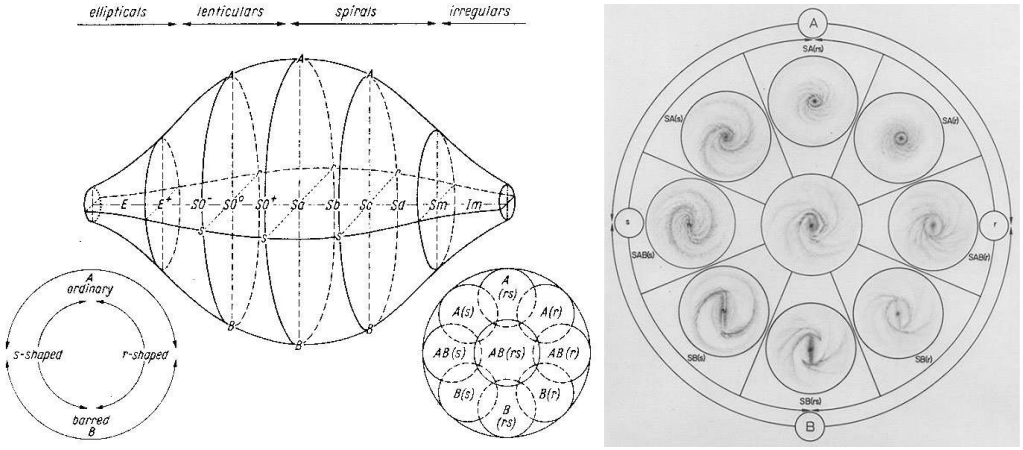

Figure 2.3: Volume classification of galaxies, revised version of de Vaucouleurs classification reported by Buta & Combes, 1996. In the panel on the right is represented the cross-section between the Sb and SBb spirals galaxies, showing the transition between the ordinary (A) to barred (B), passing thought the r and s types.

and disk combined with structure of the spiral arms. The lenticular galaxies are an intermediate case between elliptical and disky galaxies. They have a prominent bulges with a more or less relevant disk that does not show spiral arms. The class of irregular galaxies (Irr) encloses objects that have not symmetrical structure or that cannot be identified as member of the other main classes.

In 1962 Sandage proposed an update version of the Hubble classification. The four main classes are maintained. New subgroups are added to obtain a more accurate classification. de Vaucouleurs,(1959, 1963), correlate the position of the arms respect to the central bar. Spiral barred galaxies appear in two different varieties: with arms tangent to the external radii of the bar (*r type*), or with the arms that begin from the center of the galaxy (*s type*). Figure 2.3 shows a 3D representation of the morphological classification, giving an idea of the transition between the different families and types. Going deeper, analyzing the details of the various morphological types, the classification became more an more complicate.

"If you want to study the variations on the theme Sc [or other types of galaxies], you simply have to take plates and examine them, only then you get the full story. No code system can replace this. The code finally becomes so complicated that only direct inspection helps." (Baade,1963)

High resolution data and deep surveys, like the Hubble Deep Field (Williams et al., 1996), the Great Observatories Origins Deep Survey (GOODS) (Giavalisco et al., 2004) or the CANDELS survey (Grogin et al., 2011, Koekemoer et al., 2011), allow to extend the morphological analysis to higher redshift. It reveals that the fraction of irregular and clumpy galaxies increase at higher redshift while the amount of disk and elliptical decrease (Elmegreen et al., 2007, Mortlock et al., 2013, Conselice, 2014, Huertas-Company et al., 2016, Shibuya et al., 2016, Guo et al., 2015)

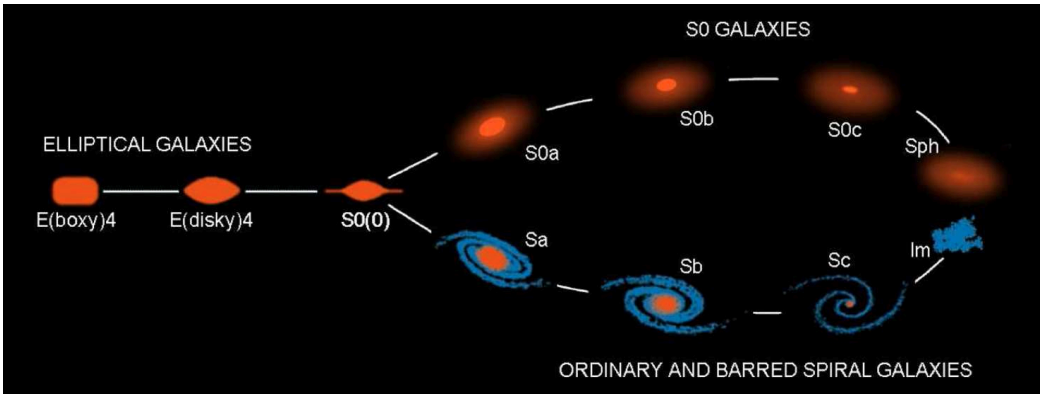

Figure 2.4: Revised Hubble sequence by Kormendy & Bender, 2012

Kormendy & Bender [2012] proposed a revised version of the Hubble fork taking into account of a more accurate morphology combined with galaxy properties (see fig:2.4). The position of a galaxies along the sequence is determined by the bulge over total ratio. Consequently, instead of splitting spiral galaxies into barred and not barred, they introduced two parallel brunches. The first one connect S0 galaxies to pure spheroidal systems. The second one contains galaxies from spiral type to irregular.

Cappellari et al. [2011] classified galaxies as fast or slow rotator. In this scheme, early type galaxies are divided in fast and slow rotator. They introduced the class of anemic spirals (Aa-Ac) (van den Bergh, 1976) that represents the transition between spirals galaxies, with obvious spiral arms and objects that show no evidence of spiral structure in optical images.

Many others recent revision of the Hubble sequence are present in the literature (e.g. Laurikainen et al., 2011, Buta et al., 2015, Kalinova et al., 2017, etc.) that extend the classification taking into account of more morphological features or correlate the galaxy shape with physical properties. The relevance of understanding morphological types of galaxies is not only into developing more accurate and complicate classifications. Indeed, the aim is the comprehension of how galaxies form and evolve to then appear with

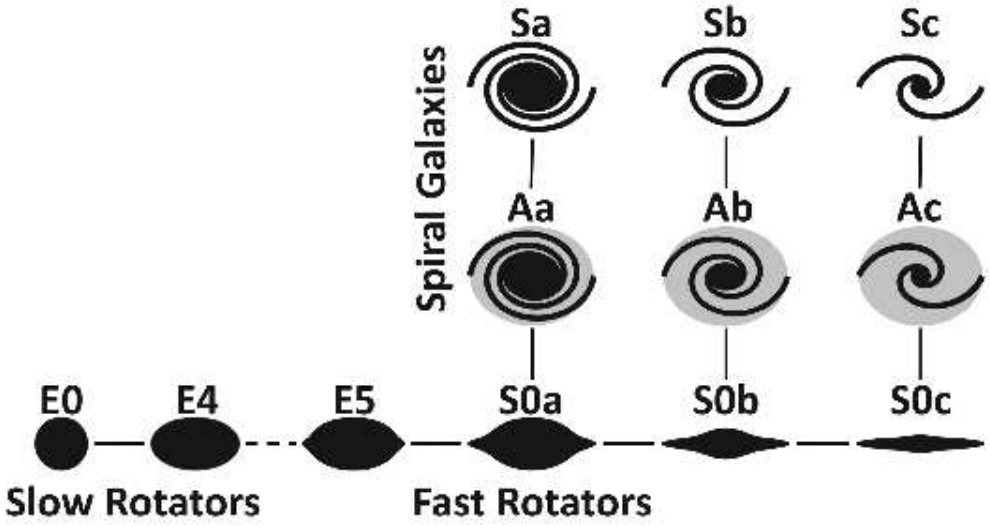

Figure 2.5: Galaxy classification revised by Cappellari et al. [2011]

different properties and morphologies as represented in the Hubble sequence, or in later revised versions.

2.0.6 Surface brightness profile

The knowledge of how the morphology of galaxies changes between different types and across the time can be quantified by the analysis of structural parameters, like the effective radii (i.e. the radius that contains half of the light in projection), the concentration of the light profile (usually identified by the Sérsic index as it will be shown here), the axis ratio, the projected angle.

The usual way to infer the structural parameters is to model the galaxy light distribution, applying analytical profiles. A first model was introduced by de Vaucouleurs in 1959, in which luminosity and size correlate following the relation: $I \propto r^{\frac{1}{4}}$. Few years later, this model was generalized by J.L Sérsic [1968], becoming the today well known Sérsic profile. The two main morphological types of galaxies, ellipticals and spirals, are both quite well modeled by a single Sérsic profile. The analytical expression is reported in the equation: 2.1.

$$\Sigma(r) = \Sigma_e exp[-k(n)(\frac{r}{r_e})^{\frac{1}{n}} - 1] \tag{2.1}$$

where $\Sigma(r)$ is the surface brightness at distance r from the center. For an ellipse the distance is $r = \sqrt{x^2 + (\frac{y}{q})^2}$ where $q = \frac{b}{a}$, the axis ratio. Σ_e is the

surface brightness within r_e (the effective size). n is the Sérsic index and k is the normalization factor coupled with the Sérsic index: $k(n) \simeq 2n - \frac{1}{3} + \frac{4}{405^n}$

The total flux is obtained integrating the profile:

$$F_{tot} = 2\pi r_e^2 \Sigma_e e^k n k^{-2n} \Gamma(2n) q/R \tag{2.2}$$

where $\Gamma(2n)$ is the Eulero gamma function. The dependence of the profile with the index n is reported in figure 2.6.

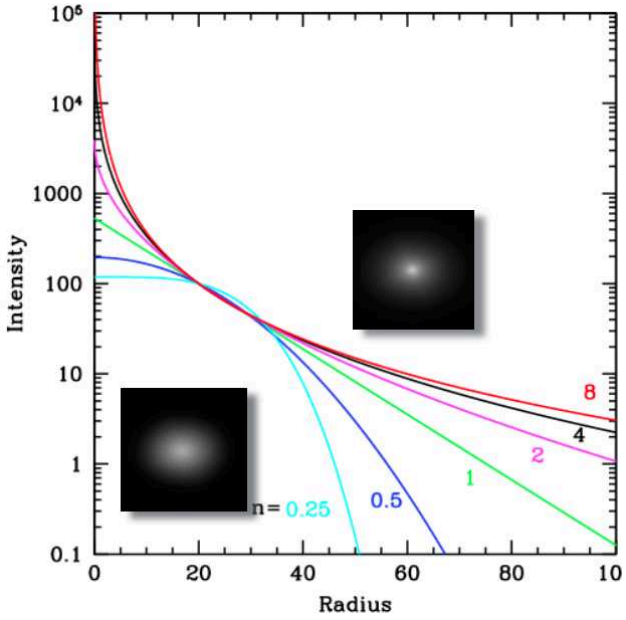

Figure 2.6: Sérsic profile for different values of n. (at fixed Σ_e and r_e)

Note that the larger the index n, the steeper the central core, and more extended the outer wing. A low value of n correspond to a flatter core and more sharply truncated wing. The de Vaucouleurs and the exponential profile are a special cases of the Sérsic profile for $n = 4, 1$, respectively.

Bulge to disk decomposition

Between elliptical and disky galaxies there is a variety of more complex systems that are composed by two components, the bulge and the disk. Since the formation processes and physics are different, they show different projected surface brightness distributions. Thanks to that the light profile of a galaxy can be decomposed by fitting two different analytical models. The disk profile is well rendered by the 2-D exponential profile. The bulge component is typically represented by a Sérsic profile. However the choice of the

range in which the Sérsic index is allowed to vary during the fit is important to obtain an accurate decomposition. Different solutions are adopted in the literature. Often this parameter is fixed to $n = 4$, the de Vaucouleurs profile (ex. Simard et al., 2011, Mancini et al., 2015, Bruce et al., 2014). An alternative choice is in the use of values larger than 2/2.5 or to allowing it to vary between [0,8] (Margalef-Bentabol et al., 2016, Vika et al, 2014).

In some works a third component is also added, to take into account of the bars or a central star burst/AGN (e.g., Laurikainen et al., 2005, Gadotti, 2011). This kind of analysis is quite challenging, since it requires an accurate reconstruction of the models, but also an optimal algorithm that allow to disentangle how many profiles are needed to better reconstruct the surface brightness profile of each galaxy.

2.0.7 Stellar populations models

The light we observe from a galaxy is the sum of fluxes emitted by a large number of stars that may have different ages, colors and metallicities. Besides that the contribution from the dust content has to be taken into account, since absorbing the radiation from young stars and re-emitting it in the infrared, affects the resulting spectrum. Knowing how interpret the Sectral Energy Distribution (SED) allows us to reveal precious informations on the internal stellar populations of a galaxy, such as stellar masses, star formation rates, and metallicities (Walcher et al., 2011).

The first model of stellar population synthesis was based on the linear combination of the SED from observed stars of different types (Faber, 1972). This technique was soon discarded because of the large number of free parameters. Recent methods are based on *the evolutionary population synthesis technique*. The main assumption, on which this approach relies on, is that the properties of the stellar population of a galaxy, with any star formation history, can be expanded in series of instantaneous starbursts. This is the concept of Single Stellar Population (SSP). Consequently, the galaxy stellar content can be approximated by a combination of different SSPs.

The spectrum of a SSP is the sum of the single spectrum of the stars at fixed ages. It is expressed by the following relation:

$$S_{SSP}(m, t, Z) = \int S(m, t, Z)\ \phi(m)\ dm \tag{2.3}$$

where $S(m, t, Z)$ is the spectra of a galaxy with a mass m, metallicity Z, at time t. $\phi(m)$ is the initial mass function that determine the distribution in mass of stars formed at the given time t.

Considering that the blue stars emit more but live less, the final spectrum of a SSP, and consequently also of the galaxy, is red dominated.

On the other side, the model should also take into account of the contribution of the new formed stars. All this factors are implemented in the *star formation history* model, that represent the ratio of star formation as a function of the time. The most commonly used (also in this work) is the tau model:

$$SFR(t) \sim \frac{1}{\tau} exp(-\frac{t}{\tau}) \tag{2.4}$$

where τ is the characteristic time. There are also more complex models, like the delayed declining exponential. Though each galaxy experience different paths, these models are good approximations that allow to model the evolution of the spectrum.

Taking into account this ingredient, finally the observed spectrum is estimated by the following integral:

$$S_{obs} = \int_0^{t_{obs}} SFR(t) S_{SSP}(t_{obs} - t, Z(t))\, dt \tag{2.5}$$

Uncertainties of this method reside in the degeneracy that exist between the age and the metallicity. Increasing the metallicity at fixed age has a similar effect to increasing the age at fixed metallicity.

Chapter 3

Catalog of bulges and disks

Contents

3.1 CANDELS Survey 44

3.2 Modeling the surface brightness profile 44

3.2.1 Comparison with the literature 47

3.2.2 Limits on the bulge-to-disk decomposition 48

3.2.3 Uncertainties on the structural properties 53

3.3 Selection of the best model 59

3.3.1 Brief introduction on machine learning 59

3.3.2 Profile selection with deep-learning 61

3.3.3 Reliability of the model selection 66

3.4 Stellar masses of bulges and disks 69

3.4.1 Uncertainties on the SED analysis 69

3.4.2 Reliability of the mass 72

3.5 Rest frame colors 76

3.5.1 Uncertainties on the rest frame colors 76

3.6 Final catalog 76

The first step towards better understanding of the link between the morphology of galaxies and the quenching process is to resolve their internal components. In this chapter I will summarize the method used as well as the tests done to built the final catalog of bulges and disks that contains structural properties of bulges and disks as well as stellar population properties [Results from this chapter are presented in a paper submitted to MNRAS that can be found in the appendix]

3.1 CANDELS Survey

The dataset used in this work is taken from The Cosmic Assembly Near-IR Deep Extragalactic Legacy Survey (CANDELS, Grogin et al., 2011, Koekemoer et al., 2011). This survey is the largest project done with the *Hubble Space Telescope*. It required 902 orbits that correspond to four months of observing time. The result is a mosaic of images taken with two cameras, the Wide Field Camera 3/Infra-Red channel (WFC3/IR), as well as the WFC3/UVIS in the UV. The entire survey covers five distinct fields of the sky: COSMOS (Scoville et al., 2007), the UKIDSS Ultra-Deep Survey (UDS: Lawrence et al., 2007, Cirasuolo et al., 2007), the Extended Groth Strip (EGS; Davis et al., 2007),GOOD-North and GOOD-South (Giavalisco et al., 2004). To address the different science goals, the CANDELS survey consists of two sets of data: the $Wide + Deep$ imaging. The Deep survey covers 130 square arc minutes with 10 orbit depth within the GOODS-North and GOODS South Fields, while the Wide one covers a total area of 720 square arc minutes within all the five fields.

In this work I used the three NIR images (F105W, F125W, F160W) from the CANDELS survey together with ancillary data in four additional bands for GOODS-N and GOODS-S (F435W, F606W, F775W, F850L) and two in the AEGIS, UDS and COSMOS fields (F606W, F814W). All images are resampled to a common pixel scale of 0.06 arsec/pixel. This is required to perform simultaneous multi-wavelength bulge -to-disk decompositions as it is explained in the following sections.

3.2 Modeling the surface brightness profile

The first step of the analysis consists on modeling the surface brightness profile of galaxies to estimate the structural parameters. For that purpose I used GALFITM and GALAPAGOS-2, from the MEGAMORPH project (Häußler et al., 2013, Vika et al, 2014), revised versions of GALFIT /GALAPAGOS (Barden, 2012, Peng et al., 2002), that allow to fit models in multi-band mode.

GALAPAGOS: Galaxy Analysis over Large Areas: Parameter Assessment by Galfit-fitting Objects from SExtractor, is an IDL code that is performed to process large surveys. Namely, it detects sources in the data, estimates a local sky background, cuts postage stamp images for all sources, prepares object masks, performs Sérsic fitting including neighbors and compiles all objects in a final output catalogue. In order to proceed with this sequence of steps, it uses the SExtractor package (Bertin et al., 1996), for the detection of the sources, and then it calls GALFIT to model the analytic profiles.

During this last step it performs first the 1-component Sérsic fit, then, taking the best model, it sets the initial conditions for the double component setup. In the default configuration the total flux is equally divided between the two components. The axis ratio and the position angles are initialized using the best fit value of the previous step. The radii are multiplied by two empirically set constant factors of 0.3 and 1.2 for the bulge and the disk respectively. Finally, the initial value for Sérsic index of the bulge is always set to 4, while for the disk it is fixed to 1.

The main new feature introduced by GALFITM is the possibility to fit galaxy models on the entire set of filters simultaneously, i.e. in multi-band mode. In other words, the output is not a single model in each filter, but the quantities related to the Sérsic profile are fitted using a family of Chebyshev polynomials, in order to parametrize their wavelength dependence. The advantage of this approach is that, combining data from different filters, effectively increases the S/N, and the fit is better constrained down to fainter magnitudes than when considering all bands independently. Moreover, polynomials can have each one a different order/degree of freedom, defined by the user, allowing the code to be optimized depending on the analysis and data set used. Giving an order of $n-1$ to the function, where n is the number of filters, means that the polynomial has no constraints and the final values are effectively the result of an independent fit in each waveband. The opposite extreme case is a constant function, thus setting zero degree of freedom. The code will fit this quantity and leave it constant over the wavelengths. The right choice of the degree of freedom for each parameter is in between these two limit cases. There is no obvious way of selecting the optimal configuration. The wavelength dependence of the parameters can change galaxy by galaxy. The approach that I used to figure out the best setup was to empirically test different configurations and use them to estimate random uncertainties as discussed in section 3.3. Three different setups are used on the entire catalog. The configurations are summarized in table: 3.1.

The flux of both components are left free in all the three configurations. The centroids of galaxies are set constant, since I assume images were properly aligned. The position angles and the axis ratios are also kept constant, since these quantities are not expected to strongly depend on wavelength. The most critical parameters are the Sérsic index and the effective radius. For the latest one, I explored its wavelength dependence allowing a quadratic variation in the first setup and restricting to constant in the second setup. Higher order polynomials are discarded given the number of bands in different fields (4-7). Regarding the Sérsic index, for the disk, I fixed it to be equal to one since I assumed an exponential profile. Differently, for the bulge component, I allowed it to vary linearly with wavelength. The reason of this

		x	y	mag	r_e	n	q	pa
$setup1$	TOT	0	0	6	2	1	0	0
	BULGE	0	0	6	2	1	0	0
	DISK	0	0	6	2	fix	0	0
$setup2$	TOT	0	0	6	0	1	0	0
	BULGE	0	0	6	0	1	0	0
	DISK	0	0	6	0	fix	0	0
$setup3$	TOT	0	0	6	1	1	0	0
	BULGE	0	0	6	1	1	0	0
	DISK	0	0	6	1	fix	0	0

Table 3.1: Order of the Chebyshev polynomials functions used to run GALFITM on each quantity, in the three different configurations. 0=constant, 1=linear variation, 2=quadratic function, nbands-1=free.

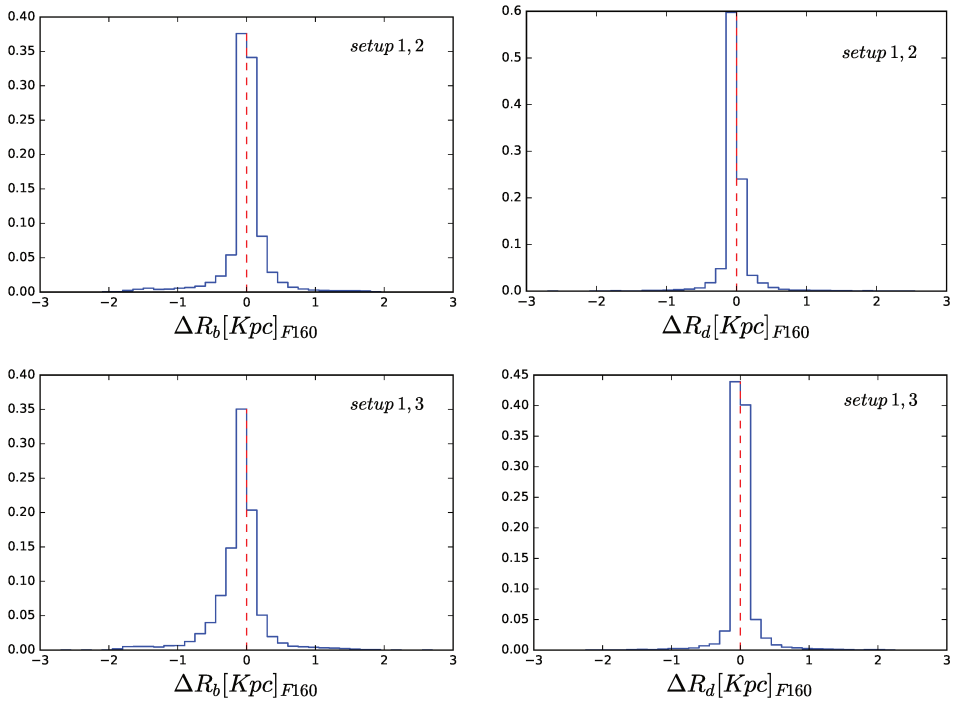

Figure 3.1: Distribution of the difference between sizes computed with different setups. First couple of histograms, on the top, are show how the measure of the size of bulges (left panel) and disks(right panel) changes if setup1 or setup2 are used. The two bottom plots follow the same idea, comparing setup1 with setup3.

choice is related to the fact that bulges are usually dominated by old stellar populations, so a strong wavelength dependence is not expected.

The third step consists in the choice of the range in which each parameter is allowed to vary. This is relevant for the Sérsic index and again it is a delicate choice in the case of the bulge component. In previous works this component is often fitted using $n = 4$, the de Vaucouleurs profile, or at least with values larger than 2/2.5. (Fisher & Drory, 2016, Simard et al., 2011, Mancini et al., 2015). I allowed it to vary between (0-8), since we realized that leaving the model to vary over a wider range of values provides better results in our statistical tests (see section 3.2.2). However there is a larger risk that unphysical solutions are reached due to a wrong light decomposition between the bulge and the disk. For that reason in the third setup I implemented stronger constraints to obtain two clearly different profiles for the two components. Namely I restricted the variation range of the Sérsic index of the bulge to (2.5-8) [1] and I reduced the degree of freedom for the size function. This way of modeling allows to get rid of the possible degenerate solutions caused by the high number of degrees of freedom given to the code using the first setup, but it is too extreme to be used on the entire sample. For that reason in the following analysis I used, as a main catalog, the setup1, combined with the third configuration output, as it will be explained in the section (3.3).

Choosing the first or second setup as primary configuration does not change the main results of this work. The output values are in quite well agreement as shown in figure 3.1. There is no bias and the medium scatter is of the order of 0.1 mag for bulge/disk sizes. For completeness it is shown also the comparison with the third setup. The scatter is larger, as expected since different constraints are applied.

3.2.1 Comparison with the literature

In order to assess the reliability of the 1-component fit, I compared the output models with results present in the literature on the same fields. van der Wel et al., 2012 did a 1- component Sérsic fit to galaxies from all the CANDELS fields in two NIR filters independently: F125W, F160W, down to $mag_{F160} = 24.5$. The method used in our work differs from the one used in the published catalog, in the sense that all bands are fitted simultaneously, thus the results are correlated. Although this technique is intended to benefit from a better S/N, I want to be sure that no systematics are introduced in the process and

[1] Galapagos does not allow to modify the setup at this level. It can be done changing few lines in the code.

	$F160W$	n	$r(")$	b/a
BULGE	18-25*	2-4	0-1.5	>0.5
DISK	18-25*	1	0-3	<0.5

Table 3.2: Range of values used in the simulation for the bulge and the disk components [See text for details]. n is the Sérsic index, r the effective radius, and b/a the axis ratio. * Assigned in function of the B/T and the total magnitude.

that bright galaxies have similar results in both catalogs.

Figure 3.2, shows the comparison between magnitudes, effective sizes and Sérsic index, the three relevant quantities of the Sérsic model. There is a reasonable agreement between the two catalogs, with a systematic difference compatible with zero and a scatter of the order of $\sim 10\%$ increasing at fainter magnitudes as expected.This result confirms then that our procedure works as expected at least for a 1 component fit and that no systematic bias is introduced by using all filters jointly.

3.2.2 Limits on the bulge-to-disk decomposition

From van der Wel et al., 2012 we already know that for galaxies fainter than $mag_{F160} = 24.5$, the statistical errors on the structural parameters, derived from a 1 component Sérsic fit, exceed $\simeq 20\%$. In the case of a double Sérsic fit, a lower limit in magnitude is expected. It needs to be tested through simulations. For that purpose I built a catalog of mock galaxies, following a standard procedure as done in several previous works. (eg. Häußler et al., 2013, van der Wel et al., 2012, Delaye et al., 2014). Namely, I generate galaxy models using two analytical profiles: a Sérsic profile for the bulge and an exponential one for the disk. Each model is then convolved with the PSF and embedded in the real background. An example of a simulated galaxy is shown in figure 3.3.

The key difference between this work and the previous ones is that the fitting procedure models galaxies in all wavelengths simultaneously. This approach has to be reproduced also in the simulations. The profiles of both components for each galaxy need to be simulated in every band. Given that a random distribution of all the parameters as a function of wavelength is not a good approximation of the reality, I simplified the problem by using a real galaxy model as a template. I selected a low redshift galaxy ($z \simeq 0.5$) that clearly presents two components (from visual inspection but also from the CNN classification. See sec 3.3). I obtained a bulge/disk decomposition (see figure 3.4) with GALFITM and then I used the best SED models of the

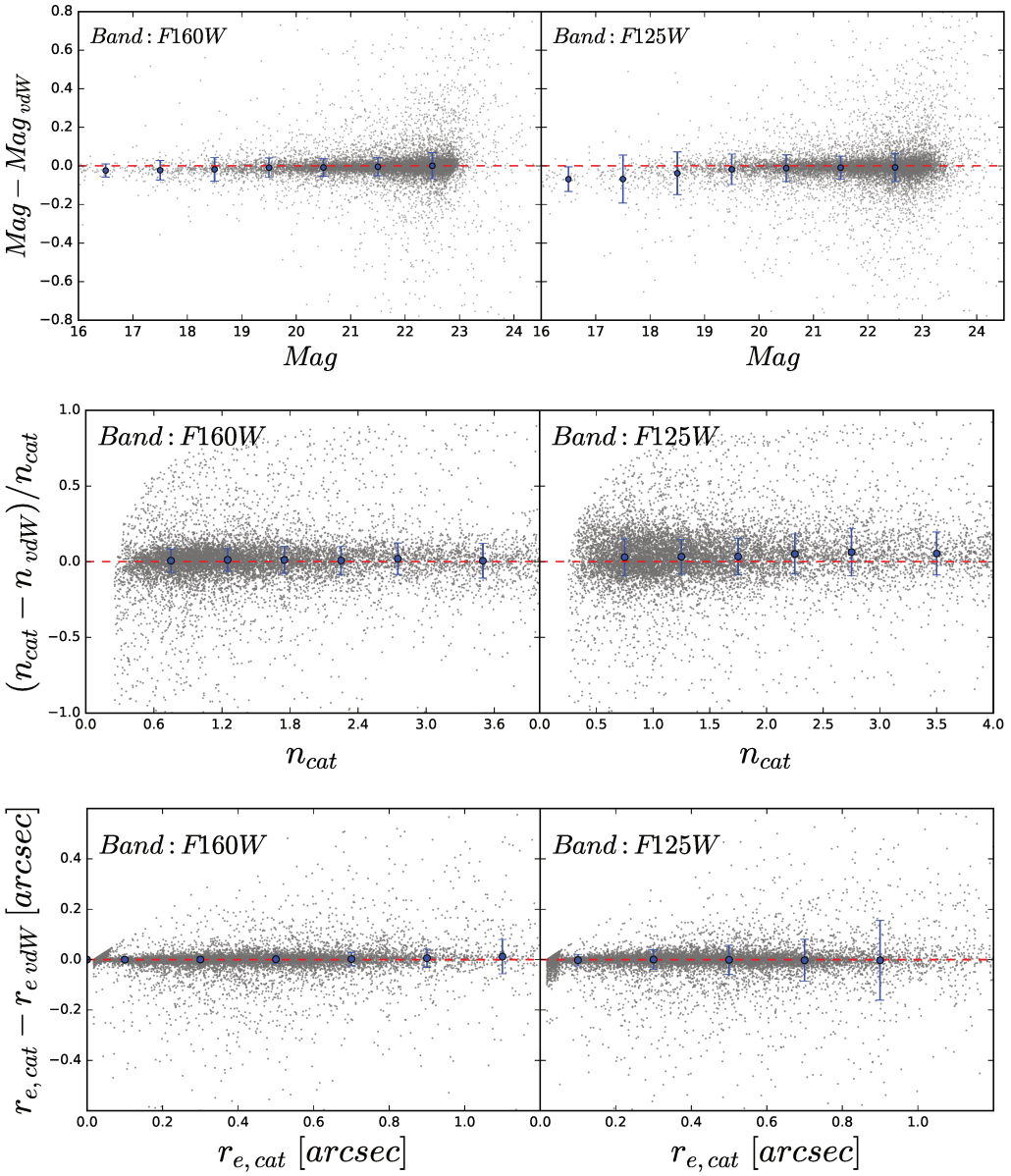

Figure 3.2: Comparison between the 1-component fit from this work and the van der Wel et al., 2012 catalog. Top panel: Magnitude, Middle panel: the Sérsic index. Bottom panel: Half light radii. Grey points are the difference between our measurements and the ones from the published catalog. Blue points are the median difference values and the error bars show the $3-\sigma$ clipped scatter.

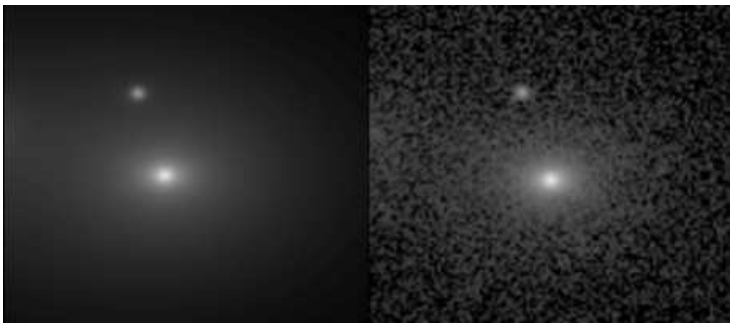

Figure 3.3: Example of a simulated galaxy. On the left there is the model convolved with the PSF, while on the right the same galaxy once it has been placed in the real background.

bulge and the disk as templates for the simulations (see section 3.4 for details on the SED fitting). More precisely, I generated random redshift values for each simulated galaxy in the range $[0.01, 3]$. I redshifted the SED templates described above accordingly to it. Finally I convolved them with the transmission curves of the filters[2] to obtain the values of magnitudes in each band. This allows to associate a realistic magnitude in all the bands with a typical SED of a bulge and a disk taking into account also the redshift distribution of the real data. Should be noticed that the simulations performed here are not representative of the *real* evolution of galaxy SEDs since it was used only one template for the entire sample. However, it should be sufficient to assess the accuracy of the fitting algorithms.

To reproduce the large variety of cases present in the real data, I assigned a random value to the bulge-over total ratio (B/T, in the i-band rest-frame, since this ratio is not constant over the wavelength) and to the total magnitude (in the H band) in the range of $[18-25]$. Random values are also chosen for the b/a ratio, constant over the wavelengths. A summary of the range for all the parameters is reported in table 3.2. In order to have a realistic wavelength behavior for the radii, I used examples from the real data. The surface brightness profile of the disk is rendered using an exponential disk profile, while the bulge component is modeled using a Sérsic profile with a randomly Sérsic index chosen in the range of [2,4], and fixed in all bands. The final simulated sample contains $\sim$ 5000 galaxies. In order to test the magnitude limit of the double component fit method, I run GALAPAGOS-2 with the same settings than for the real data. I compared then the input to

[2]I used the set of transmission curves of the HST filters that correspond to the bands used in this work

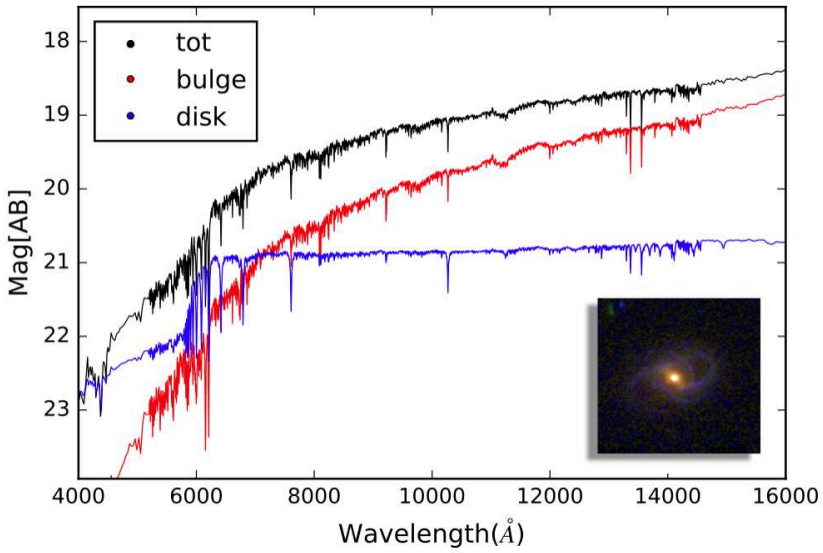

Figure 3.4: Template galaxy used for the simulation. The bulge SED is shown in red and the disk in blue. The black line shows the global SED. Random variations of this template are used to build a simulated sample of galaxies.

the output values to assess the statistical errors.

First panels line of figure 3.5 compares the input/output values of the magnitude (F160W) for bulges and disks. The right panel in each colon shows the median and the scatter of the difference in magnitude bin. The bias is close to zero for bright galaxies, while it starts to deviate for galaxies fainter than $23 - 23.5$. This suggests that the S/N limit above which the statistical errors increase significantly is reached (as pointed out by van der Wel et al., 2012 for 1 component fits). A magnitude cut at $F160W = 23$ is applied to keep a zero bias and a scatter lower than 30%. Only galaxies brighter than this magnitude limit will be considered in the remaining of this work. Figure 3.5 highlights the dependence of the size with the galaxy morphology (quantified through B/T), the total magnitude and the redshift. The different panels show the comparison between the input and output sizes of bulges and disks for two different filters: F850, F160W. As expected, the errors in the structural parameters of the disk (bulge) increase towards high (low) B/T values. When one of the two components dominates over the other one, it becomes more difficult to quantify both components properly. Indeed the uncertainties become relevant for the disk (bulge) in systems with $B/T > 0.8$ ($B/T < 0.2$). It suggests that the model of the bulge/disk in this

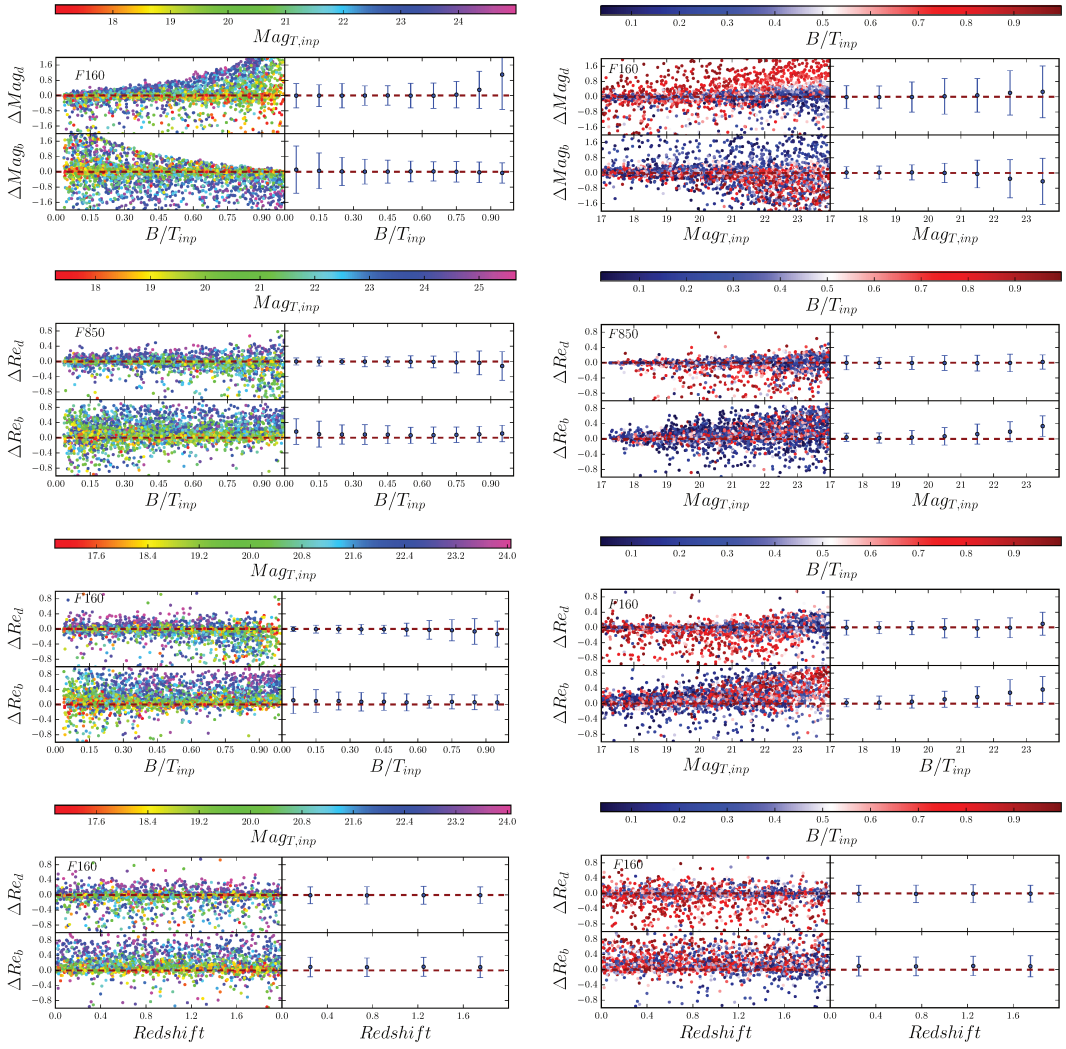

Figure 3.5: Comparison between simulated and recovered bulge and disk magnitude and half-light radii in two filters: F850 (top line) and F160 (middle and bottom lines). All panels show in the y-axis the relative difference between input and output values: $\Delta Mag = Mag_{in} - Mag_{out}$, $\Delta Re = \frac{Re_{in} - Re_{out}}{Re_{in}}$. The results are plotted against B/T (total magnitude) and color coded with total magnitude (B/T) in the left (right) panels. The last line shows the errors against redshift. In each plot we show individual galaxies in the left panels and binned median values and scatters on the right panels.

range is not reliable.

However, excluding these extreme cases, the errors remain globally within $\sim 10-20\%$. Moreover at fainter magnitudes ($F160W > 23-23.5$) the bulge sizes start deviating from the zero bias line. Again this is a signal that the S/N limit is reached. Finally, the bottom panels of figure 3.5 also show that errors do not strongly depend on redshift. However it has to be remembered that the goal of the simulations is to estimate the uncertainties on the structural parameters, so they do not capture any evolutionary trend of galaxy SEDs since a unique template is applied. Moreover the model used is an ideal case since does not take into account of internal additional structures, as spiral arms, or the effect of the surface brightness dimming.

3.2.3 Uncertainties on the structural properties

The analysis done in the previous section tested the statistical accuracy of the method but it did not provide errors on the individual quantities for every galaxy. This quantity is needed for the final purpose of this work. In particular, the SED fitting requires a proper estimation of photometric errors to obtain reliable values. Although the fitting algorithm (GALFITM) already provides errors on the profile, they are known to be underestimated (Häußler et al., 2007). Hence they need to be corrected to obtain a more realistic distribution. Following that purpose I went back on the simulation and I compared the scatter of the flux with the GALFITM error estimation. Namely I computed the following quantity:

$$\Delta F = \frac{F_{in} - F_{out}}{err f_G} \tag{3.1}$$

where F_{in} is the input flux from the simulation, F_{out} is the recovered flux from the output model and err_G is the GALFIT error converted to flux.

If the errors are well calibrated the peak of the distribution is expected to be close to zero, while the dispersion close to one. As can be seen in the top left panel of figure 3.6 it is not the case. In order to rescale them, I divided the sample in bins of err_G and computed the scatter σ. in each one of them. After that I computed a linear fit in the log space, between the mean value of err_G and σ. The resulting function was used to rescale ΔF, and to normalize the errors.

The results of that analysis are summarized in figure 3.6. The panels show the distribution of ΔF (top panels) and GALFIT errors (bottom panels) as a function of the B/T, before and after applying the correction. It is striking that the GALFIT errors do not correlate with the galaxies properties. Even after the correction no correlation is observed between the errors

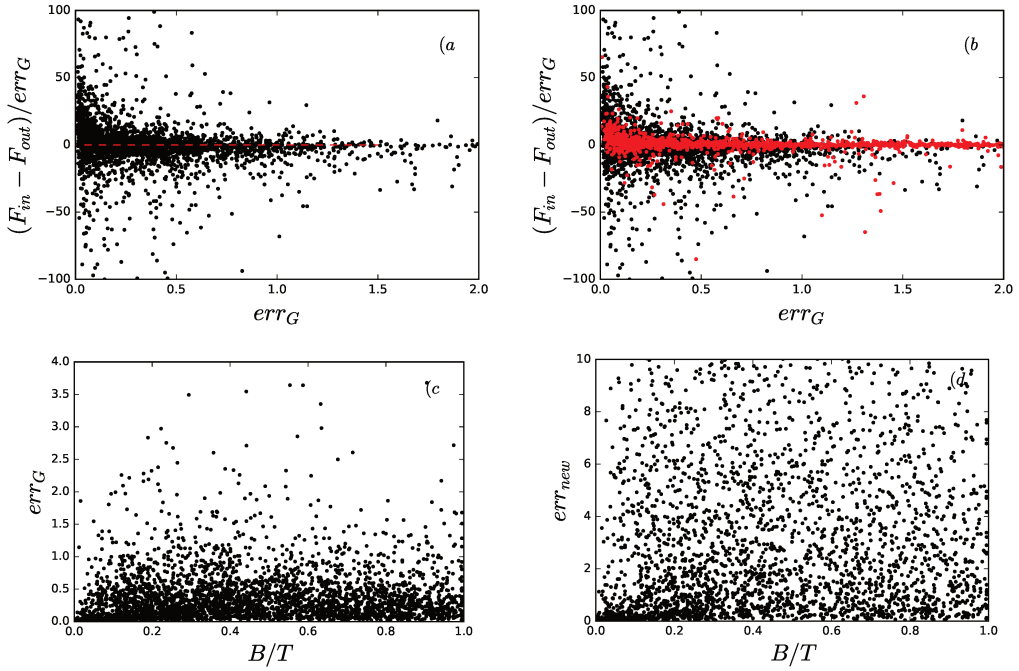

Figure 3.6: Rescaling GALFITM errors. First line. The left panel show the distribution of the quantity: $\Delta F = \frac{F_{in}-F_{out}}{errf_G}$. Red points in the right plot are the same quantity after the correction, in log space. Second line. Left and right panels are showing the correlation of the GALFIT error on the total flux with the bulge-over-total ratio. All these plots are done using the flux of the bulge components, as example. The same trends are observed for the disk.

and the structure of the galaxy (B/T), although it is expected as already assessed by the simulations in the previous section. There are several possible explanations for that. One is that GALFIT assumes gaussian noise to estimate the errors. However, it is known that the HST noise is far from gaussian. Additionally, GALFITM uses coupled constraints, which, as stated in the GALFIT manual (URL) invalidates the error estimation procedure. However the uncertainties provided by GALFITM cannot be used in the following analysis.

van der Wel et al., 2012, already tackled this issue by introducing an empirical approach to estimate uncertainties on each parameter. They assume that similar objects, where similarity here is defined as the Euclidian distance between structural parameters, have similar errors. Consequently they based the uncertainties estimation on the comparison between two fitting results, done with the same GALFIT setup on the same sample but on different data sets (deep and shallow data). Hence they check how, for 'similar' objects, the structural properties change in the two cases.

Recalling that our final catalog consists of three different setups, implemented on the entire sample (see table 3.1), and that the difference between the main setup (setup1), and setup2, resides on the wavelength dependence of the size, we decided to follow a similar approach, comparing the two output models.

We assume that the errors of the one component and two component fits essentially depend on the total magnitude, the Sérsic index, sizes of both components and the relative brightness of the two components measured by the bulge-to-total ratio in a given filter, and on the *visual* aspect of the galaxy. Other parameters such as the position angle and the axis ratio are expected to have little impact. In practice for each galaxy in the catalog, and in all bands, we computed a 6-dim/8-dim vectors $\mathbf{p^{1C}}$ $\mathbf{p^{2C}}$ for 1-component and 2-component respectively:

$$\mathbf{p^{1C}} = (\frac{m}{\sigma_m}, \frac{log(n)}{\sigma_{log(n)}}, \frac{log(R_e)}{\sigma_{log(R_e)}}, f_{sph,disk,irr})$$

$$\mathbf{p^{2C}} = (\frac{m}{\sigma_m}, \frac{log(n)}{\sigma_{log(n)}}, \frac{log(R_d)}{\sigma_{log(R_d)}}, \frac{log(R_b)}{\sigma_{log(R_b)}}, \frac{B/T}{log(B/T)}, f_{sph,disk,irr})$$

where m designates the apparent total magnitude in a given filter, n is the Sérsic index, R_e,R_d and R_b are the effective radii of the total, the disk and the bulge component, B/T is the ratio between the flux of the bulge and the total flux in the same band as m. f_{sph}, f_{disk} and f_{irr} are the probabilities that the galaxy looks like a spheroid, disk or irregular respectively Huertas-Company et al., 2016. Each value is normalized by the dispersion to have

similar variation ranges for all parameters.

Using the vector p^{1C} or p^{2C}, respectively we compute the 6-dim/8-dim Euclidian distance of each galaxy to the others in the catalog. We then select the 50 closest objects to a given galaxy[3], assuming, as in van der Wel et al., 2012, that similar galaxies in terms of relative distance in the 8D space, should have similar errors on the structural parameters. Finally the uncertainties, for each quantity, are estimated as the 3-sigma clipped standard deviation of the difference between the setup1 and setup2.

Results are shown in figure 3.7. In these series of plots we focused on the analysis of typical errors on magnitudes and sizes of both components. The uncertainties on the bulge and disk magnitudes are respectively ~ 0.2 and ~ 0.1. As expected they depend on bulge-to-total ratio. Indeed, objects with $B/T < 0.2$ have errors on the bulge magnitude that increase up to $0.6 - 0.7$ magnitudes, while the same happens on the disk magnitude that rises ~ 0.5 mag for objects with $B/T > 0.8$. This range of values is reasonable since they are the two limit cases in which one of the two component is fainter. There is little or no dependence of the magnitude errors on other parameters such as the size or the Sérsic index of the bulge. Regarding the errors on sizes of both components, the average error for the bulge is $\sim 20\%$ and $\sim 10\%$ for the disks, with again, a dependence on B/T.

Figure 3.8 shows the error dependence on wavelength. Both errors on magnitude and size are larger in shorter wavelengths. This is somehow expected since bluer bands are shallower. It is also easy to explain that bulges are more severely affected since they are expected to be redder and therefore fainter in the bluer wavelengths.

[3]changing this number by a factor of 2, does not significantly alter the results

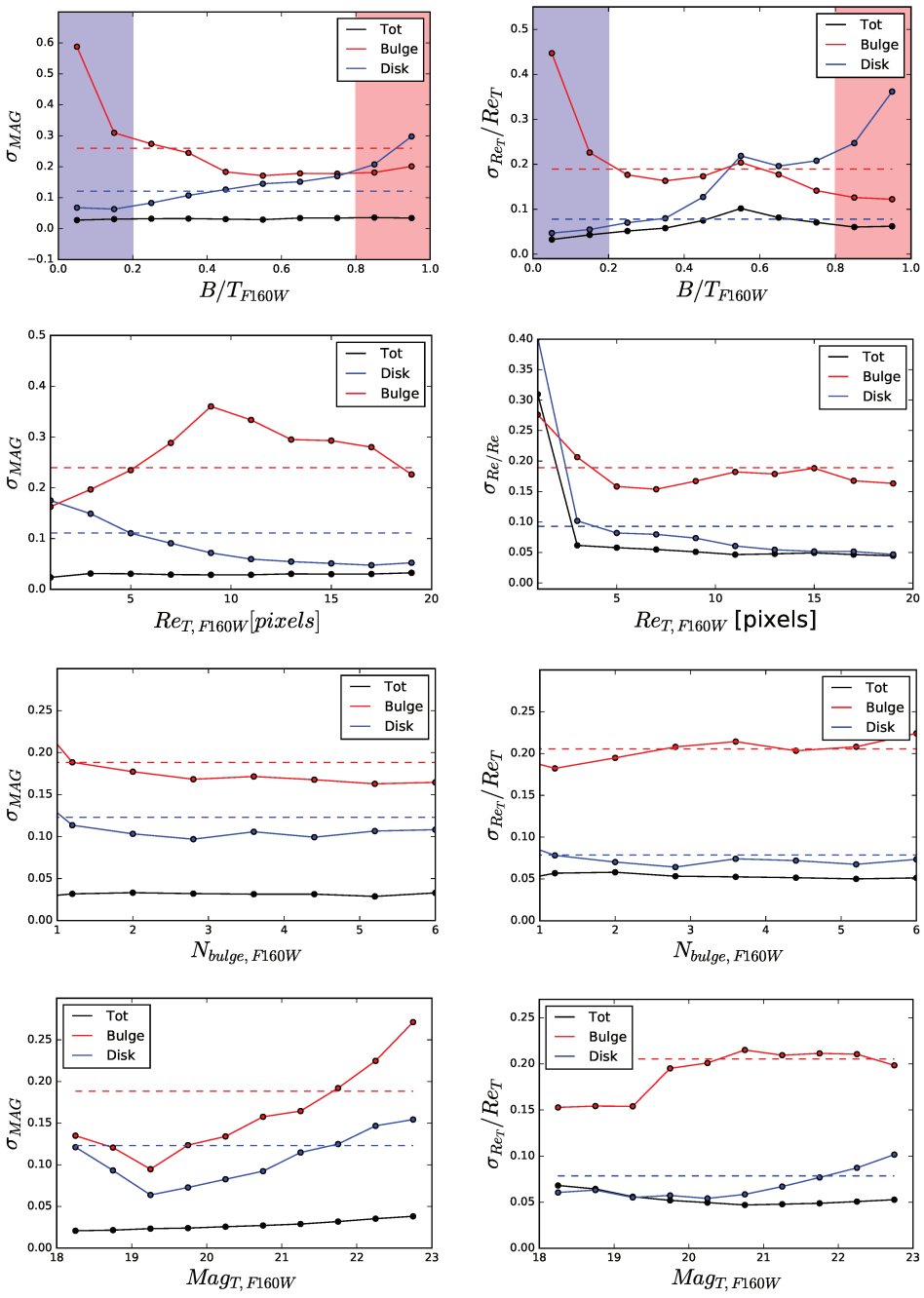

Figure 3.7: Average estimated random uncertainties in the derived structural parameters for bulges (red lines), disks (blue lines) and the full galaxy (black lines). The left column shows the errors on the F160W magnitude and the right column on the effective radius in the same filter. Errors are shown as a function of B/T (top), size and bulge Sérsic index (middle plots), F160W total magnitude (bottom). Errors are estimated by computing the dispersion between measurements on similar objects with different setups as explained in the text. Dashed lines are the median error.

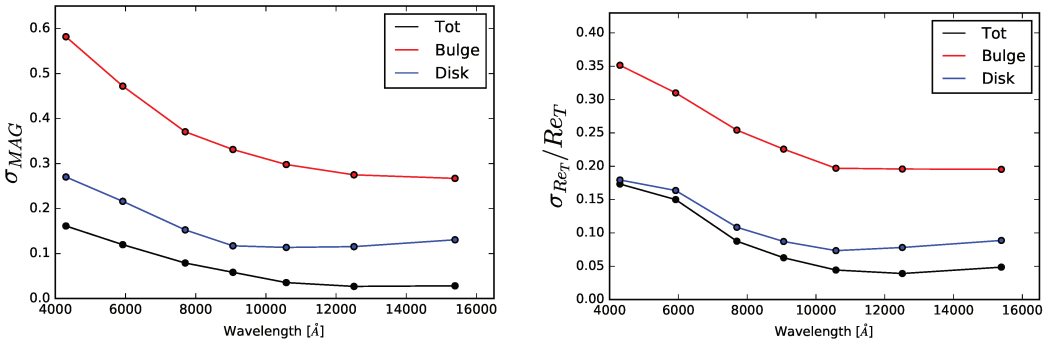

Figure 3.8: Average estimated random uncertainties for bulges (red lines), disks (blue lines) and the full galaxy (black lines) as a function of wavelength. Errors are larger in the bluer bands, especially for the bulge component as expected.

3.3 Selection of the best model

One challenging step in the study of the internal components of galaxies is in the choice of the type of model (number of components) needed. The use of a double profile on the entire sample could introduce contamination from wrong and unphysical component and have an impact on the final results. Indeed the choice of an optimal selection algorithm plays a fundamental role.

Different methods have been explored in the literature. Several works have used a statistical approach, looking at the residuals to establish if the addition of a second a profile actually improves the final results (Simard et al., 2011,Meert et al., 2015). Sometimes this approach is combined with visual inspection (Mancini et al., 2015, Margalef-Bentabol et al., 2016). The behavior of parameters, like the Sérsic index and the half light radii (from the 1-component fit), in different bands (Vulcani et al., 2014) or the fraction of the flux assigned to each component, are other paths explored in the literature to solve this issue. After testing different methods, we moved to a completely different approach, developing a novel algorithm, based on unsupervised feature learning (deep-learning). The main advantage of this kind of method is in making the choice of the best profile a-priori, instead of looking at the output results or at the residual maps.Thus it allows us to have a better control of the systematics, reducing the bias from wrong fits and building clean samples of bulges and disks. In this section I will briefly introduce the concept of Neural Networks to then finally present the new selection algorithm that we used.

3.3.1 Brief introduction on machine learning

The concept of Artificial Neural Network (ANN) was born in the fifties with the aim to bring the computer to learn, mimicking the functionality of the real brain. The first algorithm was called 'perceptrons' and was developed by the neurobiologist Frank Rosenblatt. The idea was to reproduce a system of *neurons*, connected between them like in a real brain, that are able to learn. There are mainly two different approaches: *supervised* and *unsupervised*. In all of them, the user gives to the machine a vector of informations, called 'features', from which the algorithm learns. The main difference between the two methods is based on the knowledge of the output, a priori or not, for the training sample. In the *supervised* approach, the machine learns, from a sample of known features, the information that is needed to predict the output. The opposite idea is applied in the *unsupervised*. In this case the machine is trained on an input set of features, called unlabeled, since the output is not know a priori. Namely what the algorithm does, is to analyze

the data in order to find internal structures or relationships.

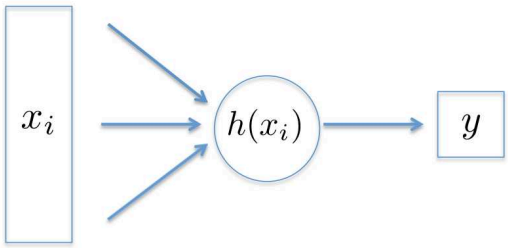

Figure 3.9: Example of the structure of a *neuron*

A standard Artificial Neural Network is composed by set neurons, computational unit, connected each other and organized in layers. Each neutron takes a set of input and output informations, expressed in the following form: $h' = f(Wh + b)$ where f is the activation function, W is the weight matrix, and b is the bias vector. It learns finding the best choice of the weight values that applied to the input data allow to infer the desired output. This is done minimizing the loss function (function that measures how well a given h' represent the output) and thus optimizing the weights and biases parameters (see Lecun 1989 for more details). The training of the network is then an iterative process. Starting from the input layers, activated directly from the input features, each neuron provides new estimations of the weight values that are then passed to the following layers (hidden layers) until the output layer.

Convolutional Neural Networks (CNN) are part of what is known as deep-learning. They have been proven to be very effective in image recognition and classification. The main difference is in the use of convolutional layers instead of fully connected neutron layer. Each neuron is locally connected to a subsample of the input instead of the entire layer. Each subsample, called filters or kernel learns different features to then produce a *feature map*. The CNN itself decides which filters are required during the training process. Anyway the numbers and the size are setted by the user. A typical CNN architecture contains also one or more pooling steps. The main idea is to reduces the dimensionality of each feature map but retains the most important information. The last fully connected layer acts as a classical ANN that collect all the recovered informations for the final output.

The CNN used in this work has 4 convolutional layers of increasing depth (from 16 to 64) and 2 fully connected layers. A 3x3 max pooling is performed after each convolutional layer to reduce the number of parameters and a 10% dropout is applied during training to avoid over-fitting. Additionally, a 1% gaussian noise is added in the first layer to avoid that the network

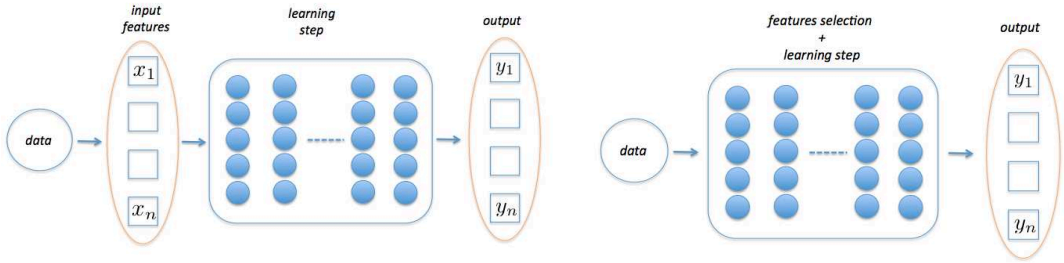

Figure 3.10: Different machine learning approaches. On the left panel, it is presented the basic scheme of a classical machine learning algorithm. On the right panel the steps that compose the deep learning method.

learns features on the noise pattern. The model configuration was established after testing different architectures. Slight modifications do not change the main results. The model is trained until convergence and evaluated on the validation dataset.

3.3.2 Profile selection with deep-learning

The model selection is done using the algorithm based on unsupervised feature learning (deep-learning) introduced in the previous section. The first step consist on training the machine on simulated galaxies.

The training sample is composed by $\sim$ 100.000 synthetic galaxies, done using GalSim [4], with a set of values that spans the entire range of the expected parameters (as for the simulation in sec: 3.2.2). The images are convolved with the PSF and a real noise from the CANDELS fields is added. We used only one filter, the $F160W$, since it is the best one available to detect the bulge, the final aim of this analysis.

The main purpose of our algorithm is not to obtain a morphological classification, but to understand which profile is the best one to fit each galaxy. For that reason we defined four different classes of galaxies among the training sample, defined as follow:

- *Pure Sérsic*: $B/T > 0.8$ and $n_b > 2.5$ Galaxies for which the surface brightness profile should be well described by a single Sérsic model.
- *Pure Exponential disk:* $B/T < 0.2$ or $B/T > 0.8$ and $0.5 < n_{bulge} < 1.5$ Galaxies for which the light profile is well captured by a single exponential profile or a single Sérsic model with a low Sérsic index.

[4] http://galsim-developers.github.io/GalSim/index.html

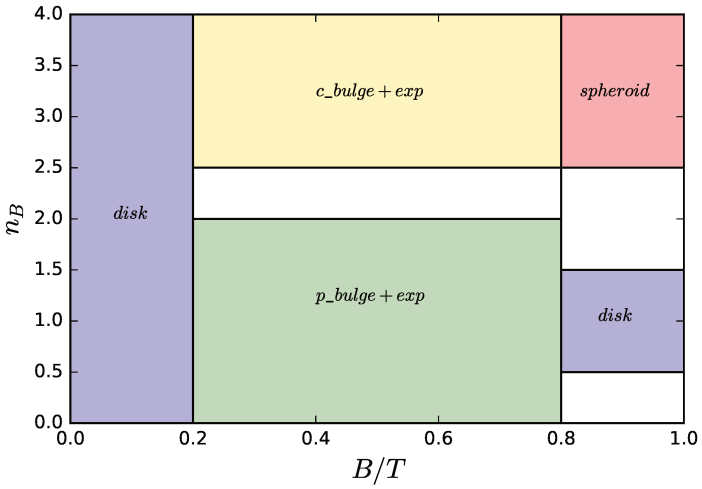

Figure 3.11: Parameters range used to define the model used to select the profile.

- *Bulge + Exponential disk:* $B/T > 0.2$ and $B/T < 0.8$ and $n_{bulge} > 2.5$ Systems for which the resultant model is clearly the sum of two components, an exponential disk and a Sérsic profile with large Sérsic index.
- *Pseudo-bulge + Exponential disk:* $B/T > 0.2$ and $B/T < 0.8$ and $n_{bulge} < 2$. Systems that still require a double components model, based on two profiles characterized by a low values of the Sérsic index.

Obviously galaxies in the real data do span the entire range of parameters. The main idea of this classification is to define models that the algorithm will use as a comparison to understand which profile is the closest one to describe the light distribution of real galaxies.

For each defined class, a CNN was independently trained, in a binary classification mode, to isolate the given profile from all the others. We thus train four different machines with the same architecture. The input of the network is a simulated 2D image (with noise and PSF) centered on the galaxy (64x64 pixels) and the output is a probability that the image is described by the model it was trained to identify. Hence at the end of the process, each galaxy has associated four probabilities, corresponding to the four classes. The sum of the four probabilities will not add to one since they come from independent estimates/machines. In the following step, we give as input to each network a second sample of simulated galaxies, in order to test the results. We quantify the ability of the CNN to distinguish between different profiles using two standard indicators:

- *Purity* (P): measure of how contaminated is a selection, for a given

model, by galaxies not belonging to that model. This is quantified as the fraction of galaxies rightly classified as not belonging to this type.

$$P = \frac{TN}{TN + FP} = 1 - \frac{FP}{TN + FP} \tag{3.2}$$

- *Completeness* (C): measure of how good the machine is to recover all galaxies belonging to a given model:

$$C = \frac{TP}{TP + FN} \tag{3.3}$$

where TP, FP are true and false positives respectively, and TN, FN are true and false negatives.

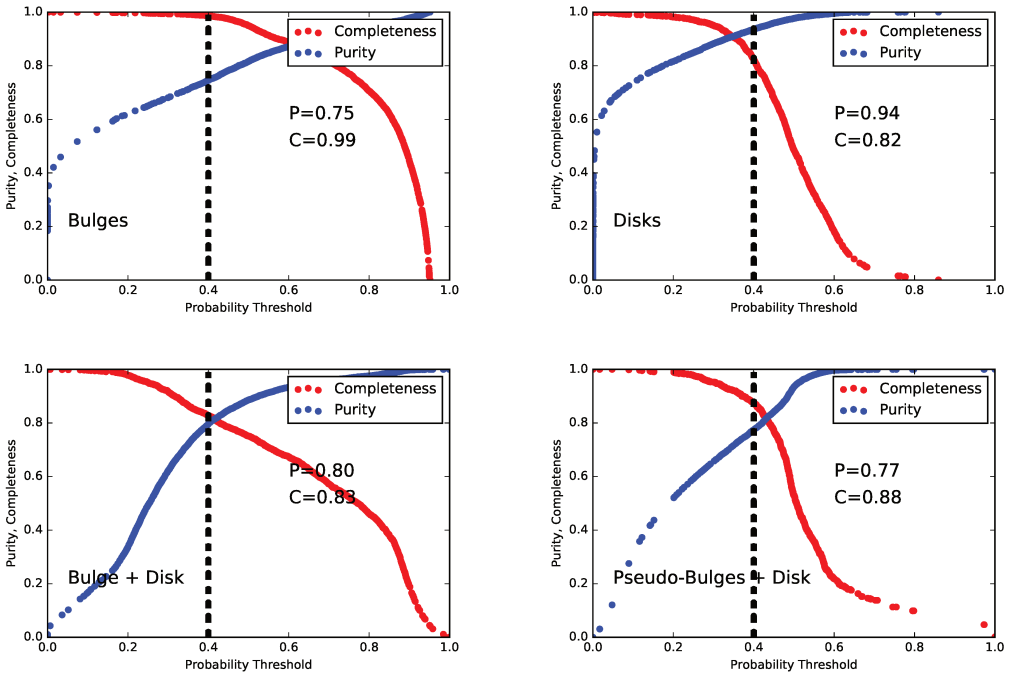

Figure 3.12: Purity and Completeness as a function of the probability threshold for the 4 types of models considered in this work. The labels in each plot show the values for the adopted threshold of P=0.4 (black dashed line).

Figure 3.12 shows the accuracy reached on the second dataset which was not used during the training phase. This ensures that our model is not over-fitted. As expected, the larger the probability, the purer the sample is, but also less complete. A probability threshold of $p = 0.4$ results in a

reasonable trade-off between purity and completeness, around $80\% - 90\%$. This threshold will be used to select the right profile. In the following step, the four trained CNN models are used to classify the catalog of real galaxies. The results consist in a set of four probabilities that tell us which given model (between the ones defined before) is preferred to describe the surface brightness profile.

The performance of the algorithm on real data is more difficult to evaluate. The "truth" is not known a-priori, like in the simulations. There is a risk that the machine, trained on mock galaxies, does not provide reliable results. Even though we used real noise and instrumental effects, we did not take into account possible companions. That can introduce a bias in the resulting probabilities. In order to minimize this effect, the size of the stamps, used in the training step, are kept small (64x64 pixels that correspond to 3.8x3.8 arcsec). Finally to verify that the resulting set of probabilities properly represents the reality, the only alternative is to perform some posterior sanity checks. The visual inspection of a subsample representative of each class is one of the possibilities. Figure 3.13 shows some examples of galaxies classified according to the probability threshold. When more than one probability is larger than the threshold, we associate the profile with the largest one. This case is allowed since the four probabilities are estimated independently.

Class	Perc.
$Disk$	14%
$Bulge$	17%
$Bulge + Disk$	51%
$PBulge + Disk$	13%
$n.c.$	5%

Table 3.3: Results of the deep-learning classification. Fraction of galaxies classified in each morphological types on the real data.

The results of the classification are reported in table 3.3. Almost all the galaxies have at least one of the probabilities above the threshold, $p = 0.4$. This is good indication that the network did not find drastic differences between the training/test simulated samples and the real data. Only $\sim 5\%$ of the sample have all the four probabilities below the threshold, so their surface brightness profile is not properly described by any of the considered models, according to our definition. After the visual inspection (and in agreement with the morphological classification from Huertas-Company et al., 2015),

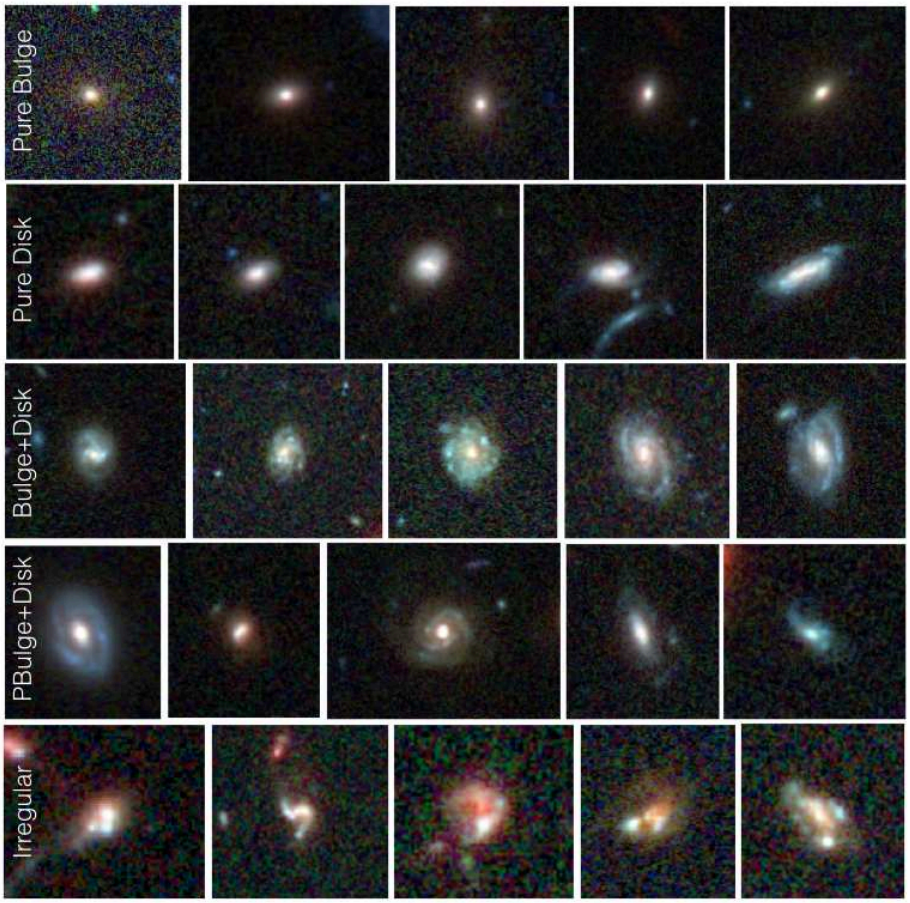

Figure 3.13: Color images created from the F160W, F775W and F606W bands (where not present, F775W is replaced by F814W). The sample is representative of the four classes of galaxies selected by the CNN algorithm. From top to bottom: galaxies for which a pure disk model is fitted, galaxies for which a pure bulge model is preferred, galaxies for which a 2 component model with $n_b > 2.5$ is preferred, objects for which a low Sérsic index bulge is the best solution. The bottom line shows irregular/unclassified galaxies.

indeed, the majority of them ($> 80\%$) are classified as irregulars (see also the examples shown in figure 3.13). Despite of that, a significant fraction of irregulars are anyway classified and a disk like model is the preferred solution to describe their surface brightness profile as expected.

The majority of the sample prefers a two component model: 51% is preferentially modeled by a classical bulge+exponential disk, while 13% are preferentially fitted with 2 low Sérsic index components. This is in good agreement with the expectations. 17% of the sample is well described by one Sérsic model with $n > 2$, while the 20% of galaxies prefer an exponential disk profile.

3.3.3 Reliability of the model selection

In order to further assess the goodness of the selection algorithm, I compared the output from the CNN with the structural parameters distribution from GALFITM . If both procedures are working well, the results should be in reasonable agreement.

Figure 3.14 shows the distribution of the Sérsic index values in the $F160$ band. Colors correspond to different classes as selected by the CNN. Obviously, galaxies for which a single profile is preferred (like pure bulges and pure disks), are here represented by the global Sérsic index, while for the double components models, we show the Sérsic index of the bulge. Each class has a different distribution, and they reflect quite well the expected behavior. Pure disks and pseudo-bulges have almost all Sérsic indices lower than 2, while pure bulges, peak at values of $n \sim 3 - 4$. Differently, galaxies that require a 2 component fit show a broader distribution, spanning a large range of values for n. Inside this class there is a fraction of objects for which the CNN predict a profile with a high Sérsic index bulge while the fitting procedure converges to a solution with a lower value (dashed orange line in figure 3.14). In order to test if whatever it is a problem of GALFIT converging to a local minimum because of too many degree of freedom given to the model, I compared the result with the one obtained with third setup (see table: 3.1).

For approximately half of the selected *ambiguous models*, the new fitting procedure converges to a profile with a value of n_b that is exactly 2.5, the lower limit imposed by the constraints. This suggests that the code assigned to these galaxies the lower limit because it is not allowed to go beyond. Therefore for them we considered the previous (Setup1) results as the best profile. However, for the other half of the sample, the new setup provided a solution with $n_b > 2.5$. Taking into account the CNN classification, we decided that these new models (Setup3) are the more appropriate to describe the surface brightness profile of these galaxies, and we used them in the following anal-

ysis. After applying this correction, the distribution of the Sérsic indices for double component systems peak for large values of n as expected. The two orange lines in figure 3.14 represent the distribution before (dotted line) and after the correction. As a second check,we explored the distribution of the size of bulges and disks. Figure 3.15, shows the distribution of the difference between the size of disks and bulges. As expected, for the vast majority of the objects, the disk component has a larger effective radius than the bulge. As a comparison it is also shown the distribution of galaxies classified as pure disks (the dotted line). The peak of the curve is close to zero. The majority of the population has a bulge larger, or at least of comparable, size than the disk proving that for this class of objects the second profile is not needed. The decomposition gives unphysical results. Including the bulges of these objects in any scientific analysis would definitely introduce a systematic error that can potentially bias the results. The use of the CNN selection allows to improve the results reducing this effect.

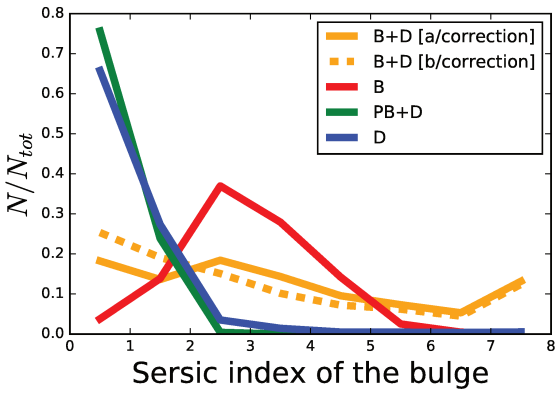

Figure 3.14: Test of the model selection: Top panel: Distribution of the Sérsic index in the different profile as selected by the CNN. Colors correspond to different classes. Red: bulges (B), Blue: disks (D), orange: bulge + exponential (BD) (before/after the correction), green: pseudo bulges + exponential disk (PB). For B and D the global Sérsic index is plotted.

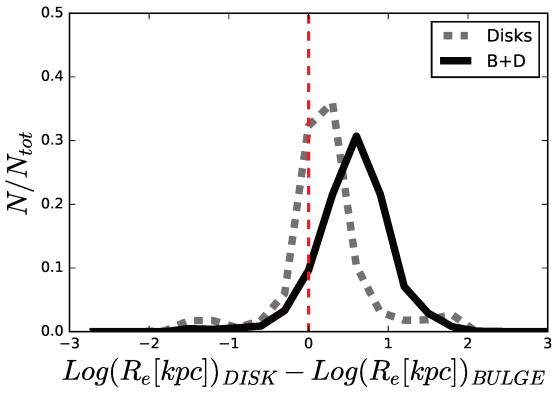

Figure 3.15: Distribution of the difference between sizes of bulges and disks. The black line shows the behavior for the 2 component systems. As expected for most of the galaxies the size of the disk is larger than the on of the bulge. Different trend is observed for galaxies here plotted with the dotted line. They are galaxies classified as pure disk from the CNN. For roughly half of the them, the fit converges to a solution in which the bulge is larger than the disk. This confirms that the second component are probably not needed for these systems

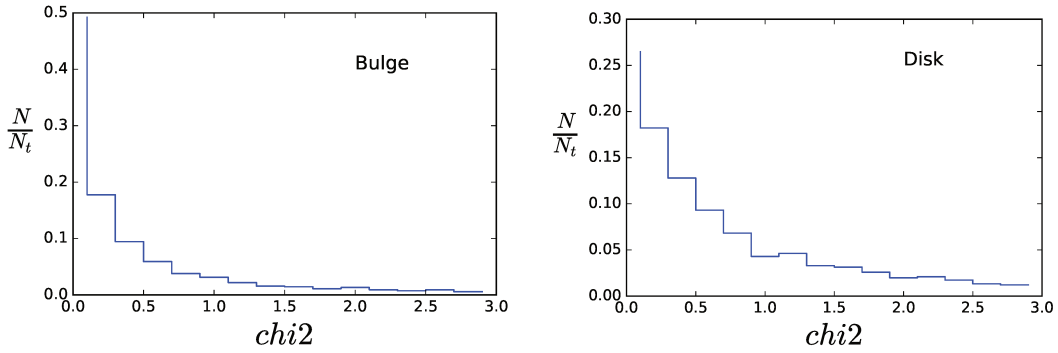

Figure 3.16: Distribution of the chi2 from the SED analysis on the bulge and disk component.

3.4 Stellar masses of bulges and disks

The result of the bulge-to-disk decomposition, and of the following profile selection, applied on a sample of $\sim$ 17600 galaxies, is a final catalog containing the structural properties of bulges and disks. In the following step I performed a 7-4 points standard SED fitting. For that purpose, I used the FAST code (Kriek et al, 2009). The input model are grids of Bruzual & Charlot, 2003, assuming a Chabrier et al, 2003 IMF and Calzetti et al., 2000 extinction law. For the star formation history (SFH) we applied an exponentially declining model, with tau in the range of $10^{8/10}$ yrs.

3.4.1 Uncertainties on the SED analysis

Reliable SED fitting requires an accurate estimate of the photometric errors. The goodness of the uncertainties is reflected in the chi2 distribution. The use of the GALFIT errors results in a broad distributions of the chi2. It means that the uncertainties are underestimated and consequently stronger constrains are applied on the SED fitting. A proof of the fact that they cannot be used in this analysis. I used the errors estimated with the method introduced in the section 3.2.3. The resulting chi2 from the SED analysis on the two components, are reported in the histograms of figure 3.16. Smaller values are found for the bulge, since the errors on that component are larger than the one on the disk, as it is found also from the simulations.

Uncertainties on the stellar population parameters are estimated by FAST itself implementing 500 Monte Carlo simulations for each galaxy.

Figure 3.17 shows some examples of the best-fit templates for the 4 types of profiles defined in this work. From the top left panel to the bottom right

one, there are respectively, pure spheroid, pure disk, bulge+exponential disk and finally pseudo bulge + exponential disk. More examples can be checked on line in the public release of the catalog[5].

[5] https://lerma.obspm.fr/huertas/form_CANDELS

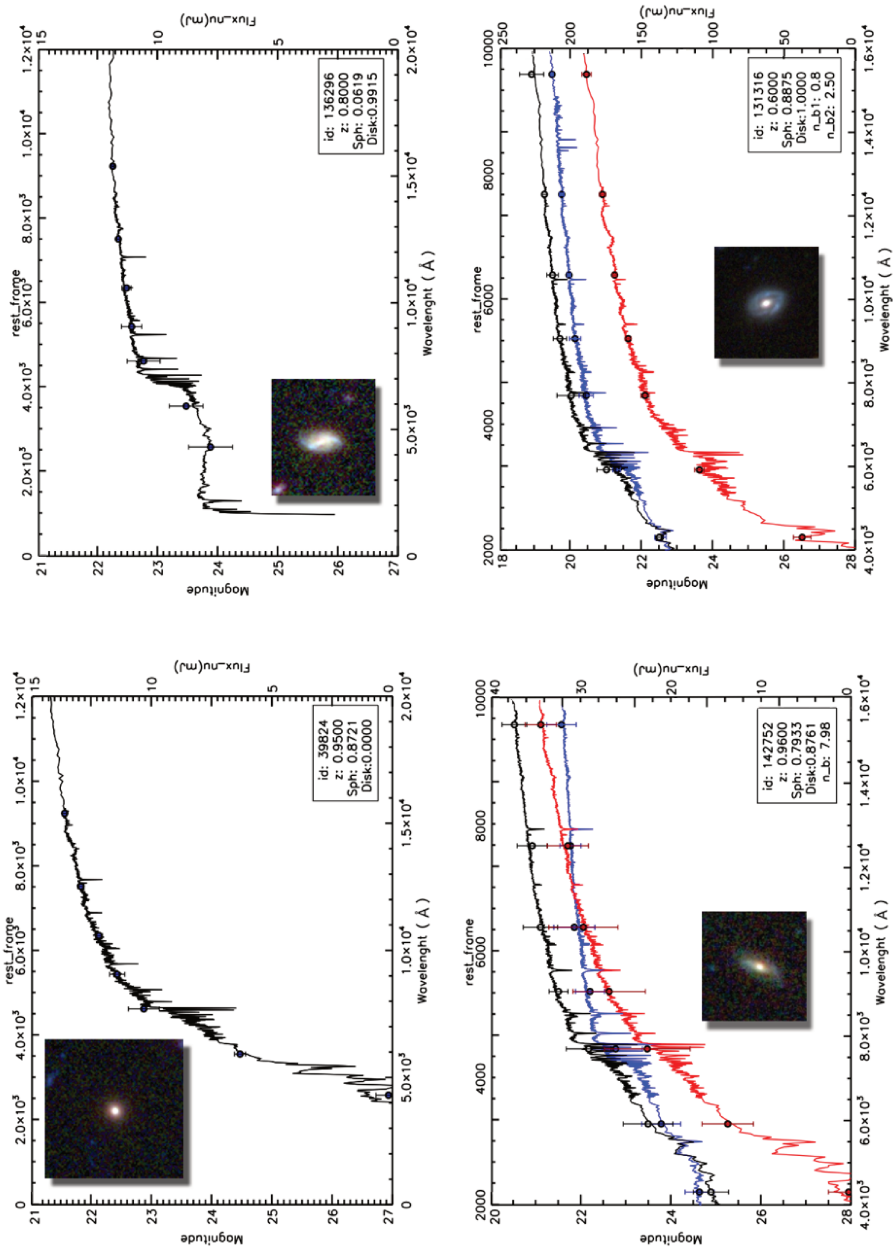

Figure 3.17: Examples of different morphologies, classified as explained in section 3.3. Top: pure bulge galaxy on the left and a pure disk one on the right. For both just a single profile is required. Bottom: Bulge+Exponential on the left and a Pseudo-Bulge+Exponential on the right. The color code is the same than for figure 3.4. Results from single Sérsic fits are shown in black. In red and blue are the bulge and the disk components respectively. The points show the measured flux in the 7 bands. The solid line are the best fit models obtained with FAST. In the legend is also reported the morphological classification from Huertas-Company et al. [2015], and the Sérsic index for the bulge. (see text for more details)

3.4.2 Reliability of the mass

The main quantities used in this work are the masses of bulges and disks. To asses the accuracy of such estimations I used again the simulation. I first run FAST on the SEDs of bulges and disks from the mock sample. I performed then a second run on the fluxes recovered from GALFITM model.

A comparison of both estimations is shown in figure: 3.18. The distribution of the difference between the input mass from the simulation, and the output one, shows a bias close to zero, with dispersion of the order of $\sim 0.2 - 0.3$ dex, which is the typical error expected for SED based stellar masses. Thanks to that it is possible to obtain an unbiased estimation of the stellar-mass bulge-to-total (B/T) ratio with a typical scatter of ~ 0.2 (bottom panel of figure 3.18). The goodness of this result does not mean that the *true* stellar mass is recovered, but that GALFITM recovers well the fluxes of the internal components of galaxies without introducing additional systematics. This is confirmed by the bottom panel of figure 3.19. The stellar masses obtained from the Single Sérsic (SS, global SED fitting) model are compared with the total mass done as the sum of masses of bulges and disks. The two results are in agreement within ~ 0.2 dex uncertainties. However this error estimation is a lower limit of the uncertainties on the stellar masses since mock galaxies used in this work are ideal cases that do not account of substructure, as spiral arms, bars, etc.

An other issue that need to be taken into account, computing the uncertainties on the mass, is the spectral coverage. In order to estimate the impact of that on the results, I did some additional tests. Using a selected sample of galaxies, for which all the 7 bands are available, I performed different run of FAST, reducing each time, the number of input bands, from 7 to 4. The removed bands are respectively the F606W in the first test (6-bands), F105W (5-bands) in the second run and the F435W (4-bands) in the last test. The results are shown in figure 3.20. In the x-axis are reported the stellar masses computed with the entire set of filters, while in the y-axis, in each panels, represent the results from the different tests. The scatter increases as expected, but the results remain unbiased. This can be seen also in the two top panels of figure 3.19. These two plots show the difference between the mass from the CANDELS catalog and the one from this work (the stellar mass from the SS fit and the one from the sum of bulge and disk components, are respectively on the left and right panel). The sample is divided between galaxies covered by four bands (grey points), and the others for which the full set of the 7 bands is available (red points). Generally our estimates are in agreement with the one from the CANDELS catalog with a scatter of ~ 0.4. This factor should be a combination of model dependence (I did not

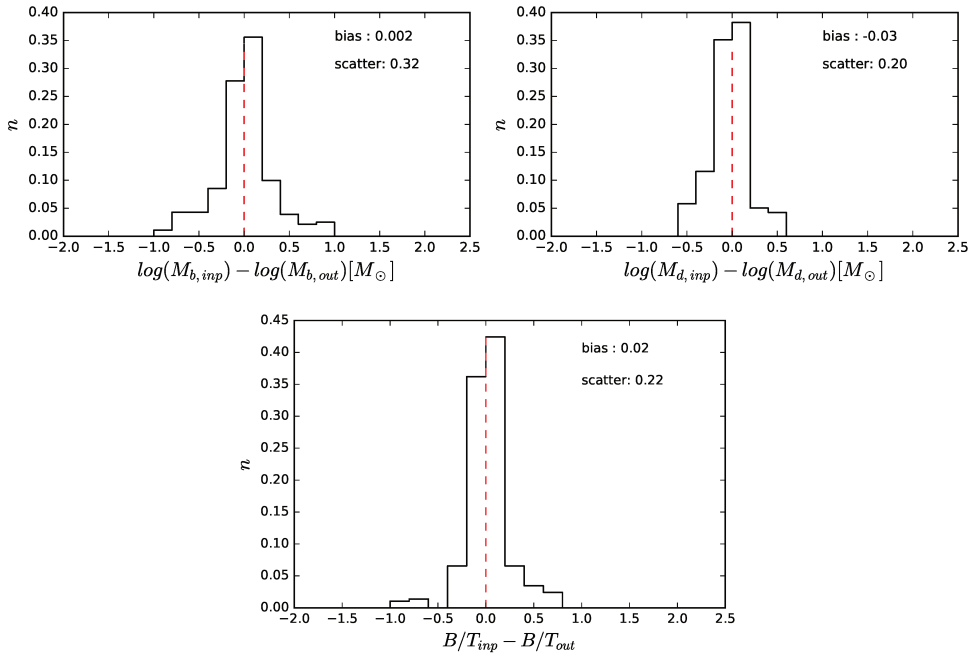

Figure 3.18: Uncertainties on the mass estimation. Distribution of the difference between the stellar masses estimated using the simulated photometry and the ones obtained with the recovered fluxes from the GALFITM model. Top left panel: bulge mass. Top right panel: disk mass. The bottom panel shows the error distribution of the stellar mass bulge-to-total ratio.

use the same stellar populations models) and spectral sampling (as we saw in the previous test). A proof of that is found in computing the bias and the scatter for the two groups independently. The results are still unbiased, using different numbers of bands, while the scatter increase from ~ 0.3, for the sample in red, to ~ 0.4 for the other one.

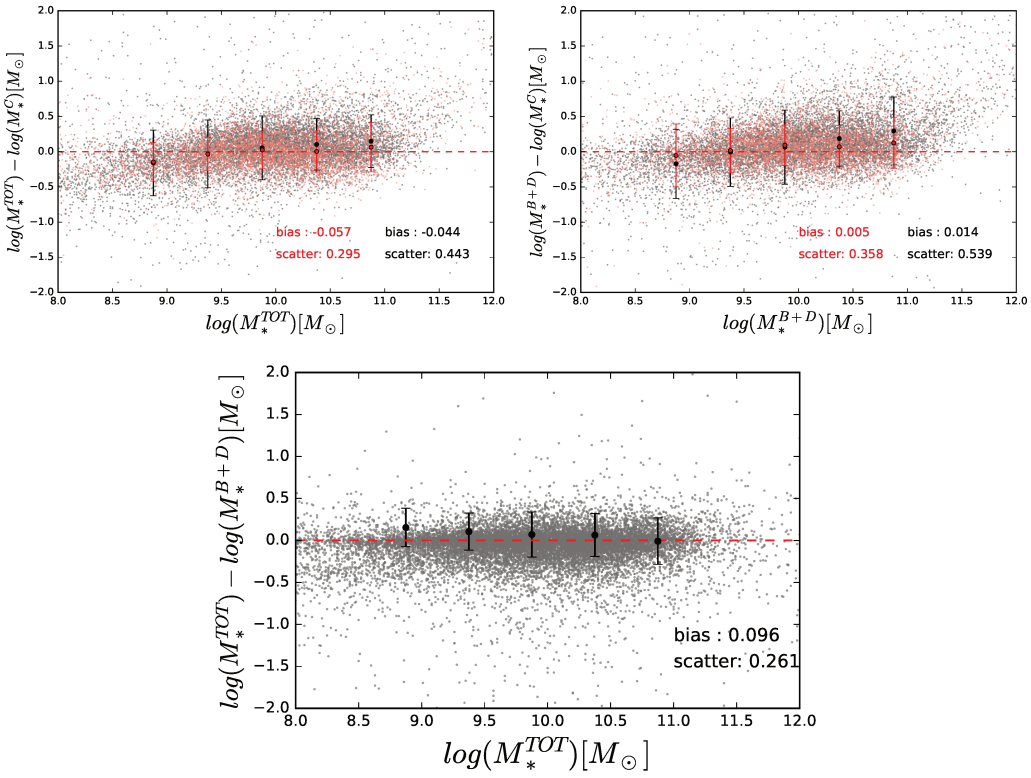

Figure 3.19: Comparison between our results with stellar masses in the CANDELS catalog. Top left panel: Difference between the stellar masses in CANDELS (M_*^C) and our estimates based on the photometry from a 2-dim Sérsic model (M_*^{TOT}).Top right panel: The same comparison but using the stellar mass estimated by adding the masses from the bulge and disk components (M_*^{B+D}). The red sample are galaxies whose SED are done using all 7 filters. The grey sample are galaxies covered by 4 bands. The bias and the scatter are estimated independently for the two sample, and reported with the same color code. Bottom panel: Comparison between the total mass, obtained from the single Sérsic fit, and the mass estimated by adding the masses of the two components.

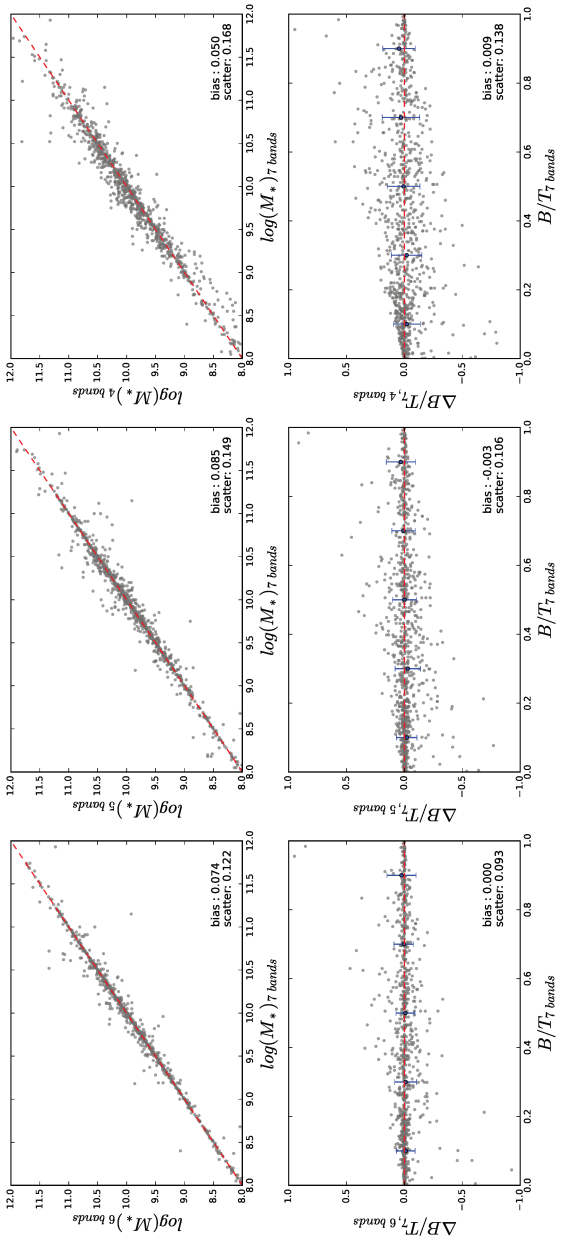

Figure 3.20: The stellar mass and the B/T estimated with different number of filters. From the left to the right respectively 6, 5 and 4 bands. The removed bands are F606W (6-bands),F105W (5-bands), F435W (4-bands).

3.5 Rest frame colors

An additional set of quantities that is relevant in the analysis of the stellar population properties are the UVJ rest-frame colors. For their estimation I relied on the theoretical profile of the Spectral Energy Distribution obtained by FAST. Namely I convolved the SED model with the transmission curves of the U , V, J,I HST filters in order to derive fluxes which are then converted to magnitude.

3.5.1 Uncertainties on the rest frame colors

The errors on the color are estimated following the same procedure that is used by FAST. For each galaxy I generated 100 mock SEDs, taking random fluxes values generated by the equation :

$$f_{MC} = f_0 + rd\, f_{err} = f_0 + 10^{\frac{23-mag}{2.5}}\, rd\, \frac{err\_mag}{1.086} \tag{3.4}$$

where rd is a random number from a uniform distribution between (0,1), f_0 the original flux and err_{mag} is the error on the magnitude as computed in section 3.2.3. I then used FAST to estimate the best fit SED model. The result is that for each galaxy I obtained a set of 100 SED models from which I interpolated the rest-frame colors. The uncertainties on the final color are then computed as the median of the distribution.

The error distribution for each components are shown in figure 3.21. Different colors represent respectively the U-V,V-J,V-I. It is worth noticing that for both components the U-V color is well constrained and the distribution peak is reached for values lower than 0.1. The same trend is observed for the V-I, while the V-J color shows a broader distribution. The reason of that is in the method used. The model recovered by the SED fitting analysis is less constrained outside of the dataset coverage. This is the case of the J band that at $z > 1$ falls outside of the well fitted region and present larger errors and bias. This is also observed when comparing results from this work with the colors from the CANDELS catalog (see figure 5.5 in section 5.2). For that reason as discussed in the section 5.2 also the I band is computed, and used instead of J in that range of z.

3.6 Final catalog

The final catalog contains all the structural parameters, for the available filters, resulting from the Sérsic and Sérsic + exponential disk fits done using

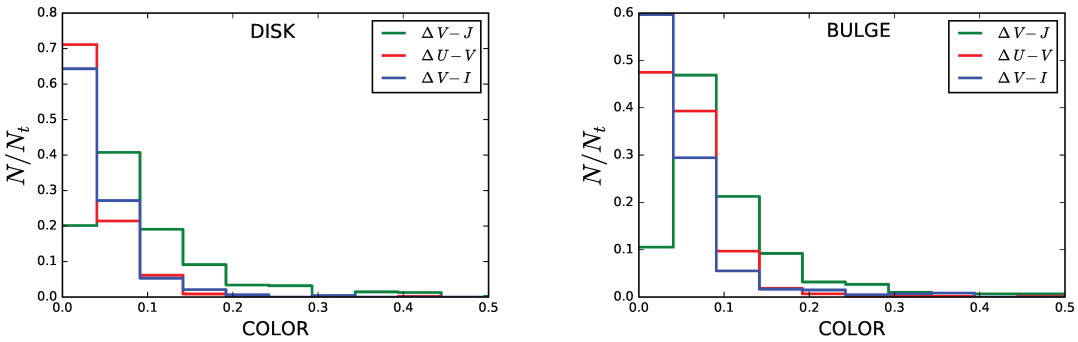

Figure 3.21: Distribution of the error on the rest-frame colors for bulges (right) and disks (left). Red lines are the errors distributions for the U-V, while green and blues represent respectively the V-J and V-I errors.

the three setups, along with the random uncertainties. In addition of that also the derived stellar population properties for bulges and disks resulting from the SED fitting, as well as the U,V, J, I rest frame colors and all the errors estimated with the MonteCarlo simulations, are provided.

Completeness

The catalog contains $\sim$ 17.300 galaxies out of 19.000 as expected from the CANDELS survey. The difference comes from the fact that there is not a perfect overlap between the fields in the different filters. To keep the reliability of the results I restricted the analysis on galaxies observed at least in 4 filters. Since the CANDELS catalog is several magnitudes deeper than our selection, the stellar mass completeness is estimated by computing the threshold above which at least 80% of galaxies from the deep catalog at a given mass and redshift are selected (see also Huertas-Company et al., 2016). The resulting threshold is at 10^{10} solar masses at low z , up to $10^{10.7}$ at z$\simeq$ 2. As a double check a second completeness estimation was done following the methodology of Pozzetti et al. [2010]. It consists firstly in computing the lowest stellar mass (M^*_{lim}) that can be observed for each magnitude. The distribution of lower limit masses is given by the following formula: $log(M^*_{lim}) = log(M_*) + 0.4(m_{F160} - 23)$. The completeness is estimated as the 90th percentile of the distribution of M_{lim}, that correspond to the stellar mass that has higher limiting threshold. This mass limit ensures that in each redshift bin at most 10% of the low-mass galaxies are lost. . Completeness thresholds at the redshift bins used in this work are summarized in table 3.4, as well as reported in figure 3.22. The sequence of panels show the

distribution of the final sample in the $M_* - z$ plane. The red line is tracing the completeness of the catalog as a function of the redshift (top panel). The two following plots are showing the same, respectively, for the star forming (middle) and quiescent (bottom) population. We assumed that the mass completeness limit for bulges and disks is similar to the one of passive and star-forming galaxies respectively. An additional restriction is applied on the bulge and the disk populations taking into account of the results from the simulations. The size of the bulge starts to be biased with a larger errors in disk dominated galaxies (B/T <0.2) while the same trend is shown by the disk radii in galaxies with B/T >0.8. For that reason a lower/upper limit in B/T is considered when properties of bulges/disk are used in the following analysis.

z	All	Q	SF
0-0.5	9.0	9.16	8.98
0.5-1.0	9.75	9.91	9.79
1.0-1.4	10.3	10.38	10.28
1.4-2.0	10.7	10.72	10.69

Table 3.4: Mass completeness thresholds in different redshift bins, for quiescent and star forming galaxies used in this work.

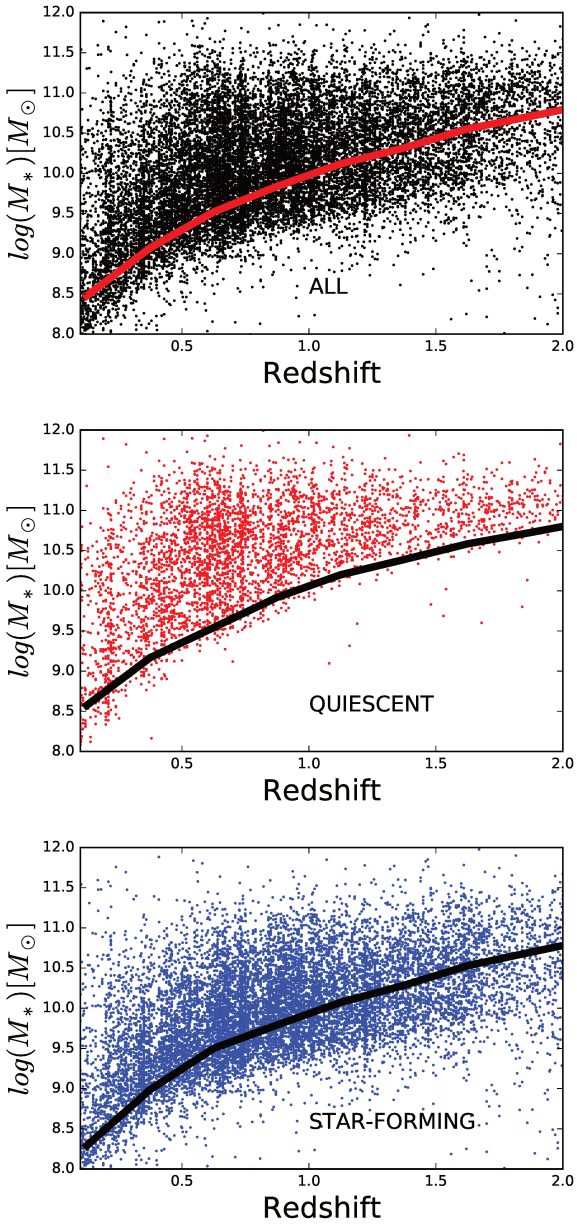

Figure 3.22: Mass completeness of the sample. Panels are showing the relation between the mass and the redshift for the final selected sample with $mag_{F160} < 23$. Top panel: all galaxies. Middle panel: quiescent population. Bottom: star forming galaxies.

Chapter 4

Unveiling how galaxies quench through the analysis of structural properties

Contents

4.1 Sample selection 82

4.2 Mass-size relation 82

4.2.1 Parametrization of the mass-size distribution . . . 83

4.2.2 Mass-size relation of quenched and star-forming galaxies 84

4.2.3 Mass-size relation of bulges and disks 86

4.3 Bulges and disks in different morphologies 91

4.4 Effect of quenching on bulges and disks structure 96

How galaxies assemble their mass or why they cease the star formation activity are the most important but still not completely solved questions in galaxy evolution. In the following 2 chapters I will use the produced catalog of accurate bulge-disk decomposition to explore resolved properties of galaxies and their evolution, to address these questions. Indeed, most of the published works use integrated properties. Our measurements allow to go a step beyond resolving the internal components of galaxies. This chapter is focused on the study of the mass-size relation of bulges and disks combined with morphological informations (B/T , Sérsic index, etc.), with the aim to put constraints on quenching processes.

4.1 Sample selection

I describe in the following the different selections applied to our analysis sample:

- the analysis is focused on galaxies with $logM_{*,tot} > 10.3M_{\odot}$. This is a trade-off between statistics and completeness. Up to $z \simeq 1$, this stellar mass limit is larger than the completeness limit. At higher redshift, some galaxies might be lost as seen in table 3.4. We will discuss the impact on our results in the forthcoming sections.

- The setup1 is used as the primary setup (see table 3.1) for deriving the structural parameters. As explained in the previous chapter, setup2 is used to estimate the uncertainties on the sizes that are used for the fits.

- The choice of the best profile (1 or 2 components) is done using the output of the CNN selection algorithm, taking into account the probability threshold (defined in figure 3.12). In the cases in which more than one probability is larger than the threshold I selected the model with highest probability. I define as pure bulges (disks) objects for which PB>0.4 (PD>0.4). For these galaxies a single Sérsic fit is used and the B/T is set to 1 (0). For objects with PBD>0.4 or PPB>0.4, I used a 2 component model and the B/T ratio is computed by dividing the mass of the bulge by the total. An additional correction is applied using setup3 on particular *ambiguos* cases of double component systems in which the Sérsic index of the bulge is measured to be <2 by GALFITM while the machine learning algorithm provides a probability PBD larger than 0.4. To be sure that is not a problem of the GALFIT model in such cases I compared the two catalogs. If the galaxy in the setup3 has n_b equal to 2.5, the lower limit imposed in the fit, it means that GALFIT assigned that value only because it was forced to be in that range but the profile would be better fitted with a lower Sérsic index model. If instead the value of n_b is larger than 2.6 in the setup3, I choose this model as the better profile for that galaxy. Consequently also all the other properties, like sizes, mass, colors, are replaced by the values from setup3.

- finally whenever I plot individual components (bulges or disks), I restrict the analysis to objects with B/T>0.2 for the bulge and B/T<0.8 for the disk since our simulations show that above these limits the structural parameters are affected by large uncertainties.

4.2 Mass-size relation

In this section I analyze and discuss the mass-size relations of galaxies and their individual components obtained with our catalog for a selected sample

as explained in the previous section.

4.2.1 Parametrization of the mass-size distribution

In order to quantify the different relations we fit models to the distributions of galaxies in the mass-size plane. In particular we follow the same method and parametrization as van der Wel et al. [2014]. Namely, we assumed a log-normal distribution for the size $N(log\, r, \sigma_{log\, r})$, where $log\, r$ is the mean and σ_{logr} the intrinsic dispersion (without measurement errors). The semi major axis r is parametrized as a function of the stellar mass with the following formula :

$$r(m_*) = Am_*^{\alpha} \tag{4.1}$$

where $m_* = M_*/7\text{x}10^{10}M_{\odot}$. The model distribution $N(log(m_*), \sigma_{logr})$ provides the probability of observing a galaxy with size R_e for a given mass m_*. Assuming the distribution of the uncertainties $\sigma log(R_e)$ (see section: 3.2.3) to be Gaussian, then the probability of this observation is the result of the inner product of two Gaussians:

$$P = N(logR_e, \sigma_{logRe}), N(log(m_*), \sigma_{logr}) \tag{4.2}$$

We used our measured sizes for both populations (/components) together with the computed uncertainties, $\sigma log(R)$ to estimate the probability. The same relation is used to compute the probability on the star forming (P_{SF}) and the quiescent (P_Q) population (as well for bulges and disks). An additionally random uncertainty of 0.2 dex on the stellar mass, is also included as an additional source of uncertainty in the R_e estimation. To keep the probability P of one dimension, we assumed the errors on masses and sizes to be proportional : $\sigma\, log\, m_* = \alpha\, \sigma\, log\, R$. We adopted a constant $\alpha = 0.2/0.5$ respectively for the star forming and the quiescent population (i.e. also for bulges and disks) which are close to the expected slopes of the mass-size relation. Finally, in order not to be dominated by low mass galaxies which are more numerous, we weighted the probability value for each galaxy by the inverse of the measured number density $W = 1/(n(z, m_*))$ at a given mass m_* and redshift z (Muzzin et al, 2013). As done in van der Wel et al. [2014]), a 1% of possible outliers is also included. The final likelihood of the six model parameters (intercept A, slope α and intrinsic scatter $\sigma log\, r$ respectively for star-forming and passive galaxies/ bulges and disks) is described by the function:

$$L = \sum ln\big[WP_Q + 0.01\big] + \sum ln\big[WP_{SF} + 0.01\big] \tag{4.3}$$

The final likelihood is then maximized in order to estimate the best-fitting values for the parameters. The same analysis is used for quiescent and star forming galaxies, as well as for bulges and disks, as detailed in the following.

4.2.2 Mass-size relation of quenched and star-forming galaxies

I first start by analyzing the global mass-size relation of star-forming and quenched galaxies. This allows to compare with previous published results. In this particular case, I use single Sérsic profiles to be consistent with the literature. Star-forming and quenched populations are selected according to their rest-frame UVJ colors. Fits are done in different ranges of mass to be able to then compare the results with the ones from van der Wel et al. [2014]): [9.5,11.5] for star forming galaxies, [10.3,11.5] for the quiescent population. The mass-size relations are shown in figure 4.1 and the best fits values are reported in table 4.1.

	Quiescent			Star-forming		
z	$log(A)$	α	$\sigma log(R)$	$log(A)$	α	$\sigma log(R)$
0.25	0.66	0.57	0.18	0.69	0.16	0.21
0.75	0.49	0.48	0.18	0.66	0.13	0.20
1.2	0.40	0.46	0.20	0.59	0.05	0.19
1.8	0.33	0.35	0.22	0.58	0.06	0.19

Table 4.1: Results from the parametrized fit on the mass size relation for the star-forming and quiescent populations ($M_*/M_\odot > 2 * 10^{10}$).

	Quiescent [vdW]			Star forming [vdW]		
z	$log(A)$	α	$\sigma log(R)$	$log(A)$	α	$\sigma log(R)$
0.25	0.60	0.75	0.10	0.86	0.25	0.16
0.75	0.42	0.71	0.11	0.78	0.22	0.16
1.2	0.22	0.76	0.12	0.70	0.22	0.17
1.8	0.09	0.76	0.14	0.65	0.23	0.18

Table 4.2: Results from the parametrized fit on the mass size relation for the star-forming and quiescent populations from van der Wel et al., 2014.

It is interesting to notice that the best fits done on the quiescent and the star forming populations differ from the ones estimated by van der Wel et al., 2014 and the difference increases with redshift, as can be seen in the figure

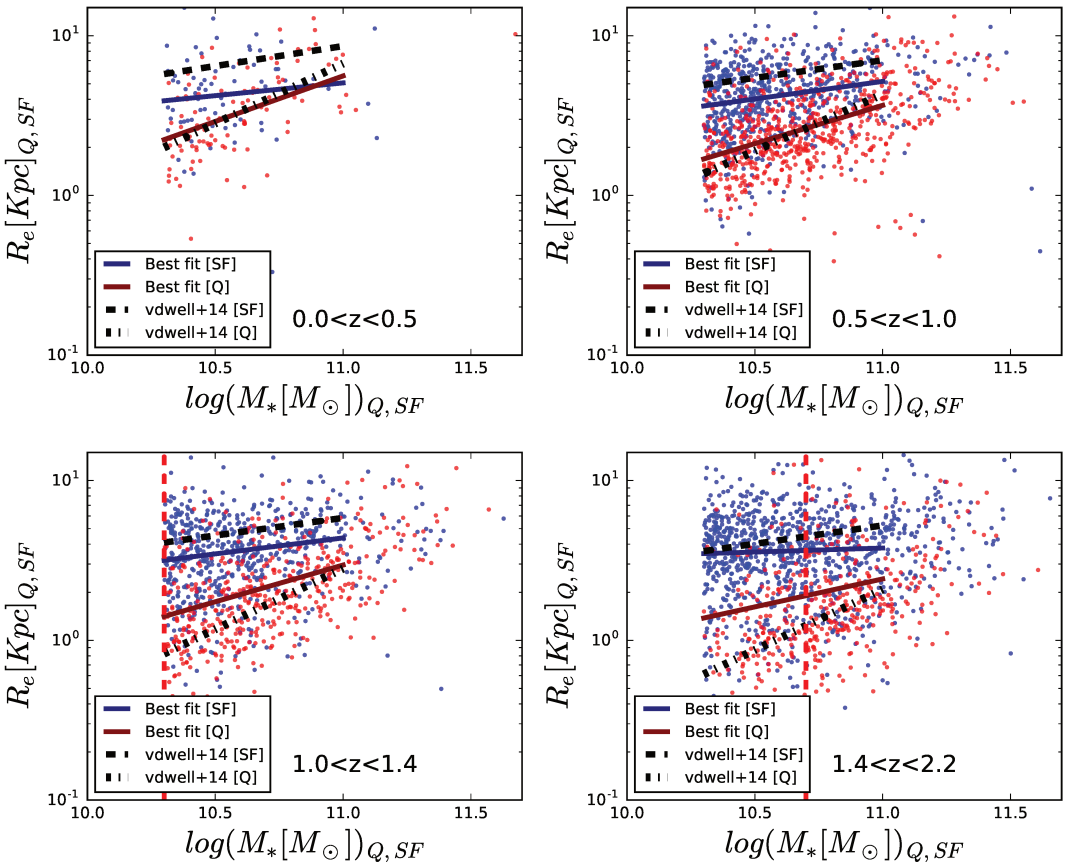

Figure 4.1: Comparison between the mass-size best fit relation from van der Wel et al., 2014 (black dotted lines) and the one from this work, both done for star forming and quiescent galaxies in four redshift bins. Blue and red points are respectively the star-forming and quiescent galaxies. The red dashed lines represent the completeness limit.

4.1 but also comparing the tables 4.1, 4.2. In particular I find a shallower slope (α) at all redshifts, while van der Wel et al. found values of $\alpha = 0.7, 0.2$ respectively for the quiescent and the star forming populations. Also, van der Wel et al. does not find any significant evolution of the slope, while in the present fits I do find a decrease with redshift for both populations. The other difference is in the intrinsic scatter. van der Wel et al. found values for the intrinsic scatter that are smaller for the quiescent galaxies than for the star forming ones. Our results are in agreement with this trend. Though the estimated values are larger. The method used to infer the best fit and the sample are the same, hence similar results are expected. The reason of this disagreement might be a consequence of the different methods used to estimate the sizes. Just to recall, in this work a multi wavelength approach is used while van der Wel et al. [2014] modeled profiles independently in each band. However a comparison of the results is done in section 3.2.1. Figure 3.2 shows that the two distributions are in agreement with zero bias and a scatter of the order of $\sim 10\%$. Another difference between the two works resides in the way errors are computed. As explained in the previous chapter (3.2.3), I computed errors by comparing the results from two different settings. van der Wel et al., uses the comparison between 2 identical runs on objects with different S/N.

Finally the difference in completeness between the 2 samples can also contribute to explain the diversity of the results. In the present work a selection was done for $m_{F160} < 23$ while in the van der Wel et al. [2014] the magnitude limit is fixed at $m_{F160} < 24.5$. Consequently the diversity in the selection can affect the distribution of masses and sizes which can eventually explain the difference in the fits. In order to test this effect, I show in Figure 4.2 the ratio between the number of galaxies in our catalog and van der Wel's for a given size range. As expected, a fraction of galaxies is lost in each bin. However no significant trend with size is observed. No evidence of a strong bias. Although for the quiescent populations there is a drop at larger radii that increases at $z > 1$ that could explain the deviation from the best fit in this range of z. In the following, I will use as reference our own measurements to compare with other relations, for consistency.

4.2.3 Mass-size relation of bulges and disks

The mass-size relations for bulges and disks is now shown in figure 4.2.3. The colors define the different components/systems. Red points are bulges while the disk components are represented in blue. The two populations contain also pure bulges and pure disk galaxies. They are represented by the size and the mass from the single profile while for galaxies classified as a double

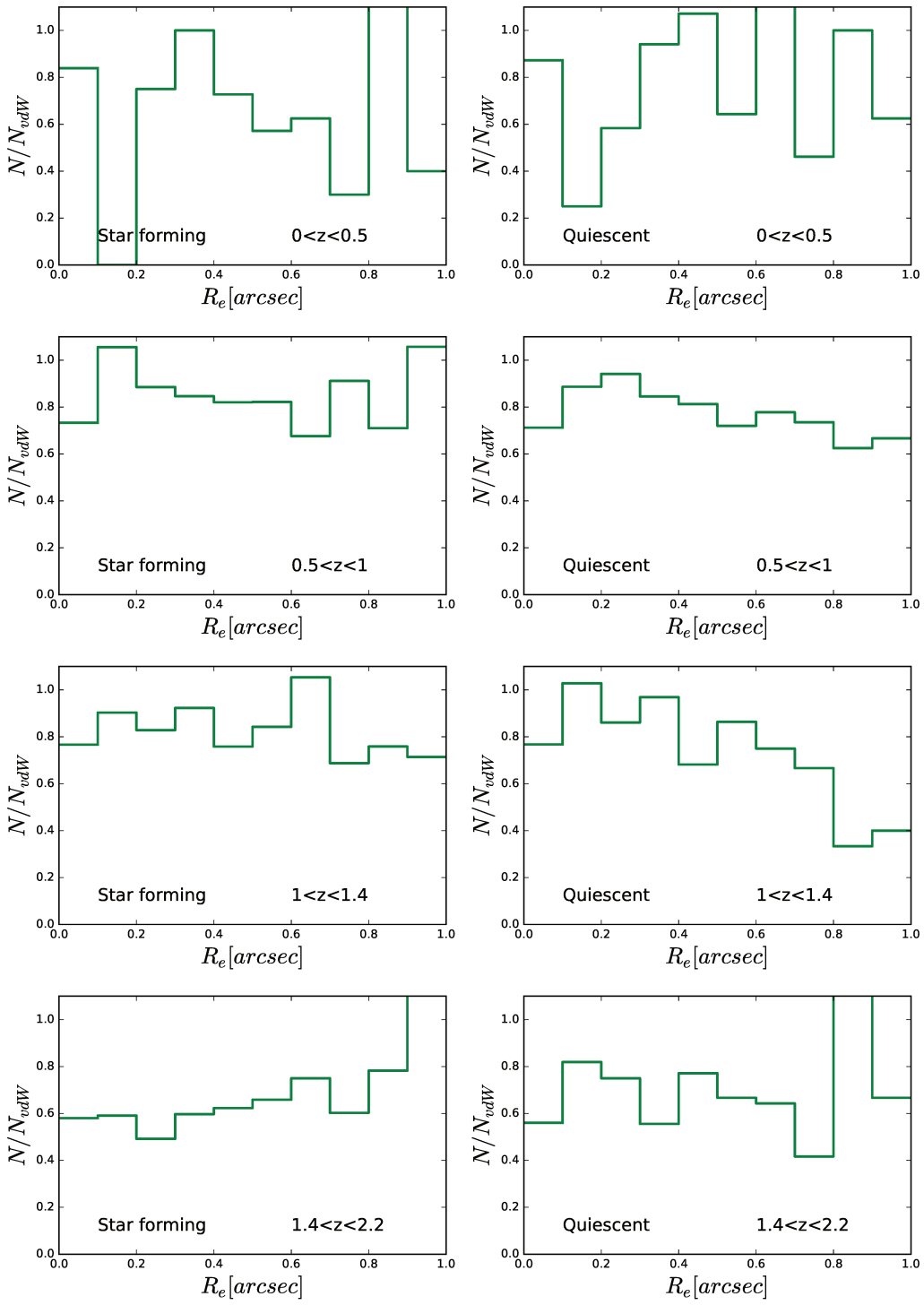

Figure 4.2: Comparison of sizes distribution between the catalog presented in this work and the one from van der Wel et al., 2014. In the y-axis is reported the fraction of galaxies for a given size bin.

systems, the values from the two components are used. Bulges identified as pseudo-bulge are not considered here.

Both components follow clearly two different relations at all epochs. The distribution looks remarkably similar to the plots of figure 4.1, showing quiescent and star-forming galaxies. This result is remarkable, considering that all bulges/pure spheroid systems and disk/ pure disks are represented here without applying any selection on the star formation activity of the host galaxy.

Recall that the fit of the mass-size relations for bulges and disks is done accounting only for objects with $logM_* > 10.3M_\odot$. Results are reported in Table 4.3 and shown in figure 4.2.3. For comparisons best fits, done for the star forming and quiescent populations are also reported. They confirm the similarity between the relations of quenched/star forming galaxies and the bulges/disk distributions.

This agreement could simply reflect that the majority of quenched galaxies are completely bulge dominated and that the majority of star-forming galaxies are disk dominated. Since I am using light weighted sizes, it can also indicate that, for star-forming galaxies, the size is driven by the star-formation, which most probably comes from the disk and therefore drives the relation. For quiescent galaxies however, the size is more driven by the mass distribution which is concentrated in the bulge component. In order to better understand these trends, I performed two additional fits to the mass-size relation. First I fitted only quiescent bulges and then bulges living in elliptical galaxies (B/T>0.8). A similar approach is followed for disks, selecting star forming disks and then only disks in galaxies with B/T<0.2. Results are shown in tables: 4.3,4.4.

	Bulge								
	$M_b > 2*10M_\odot$			Q_{Bulge}			$BT > 0.8$		
z	$log(A)$	α	$\sigma log(R)$	$log(A)$	α	$\sigma log(R)$	$log(A)$	α	$\sigma log(R)$
0.25	0.49	0.53	0.23	0.49	0.61	0.20	0.51	0.53	0.20
0.75	0.43	0.54	0.22	0.40	0.61	0.19	0.44	0.49	0.16
1.20	0.33	0.43	0.23	0.30	0.49	0.21	0.36	0.40	0.18
1.80	0.27	0.24	0.27	0.19	0.25	0.22	0.33	0.02	0.29

Table 4.3: Results from the parametrized fit on the mass size relation for bulges wit different selections. 1: all bulges with $M_b > 2*10^{10}M_\odot$. 2: Bulges in quiescent galaxies. 3: Bulges within galaxies with B/T >0.8.

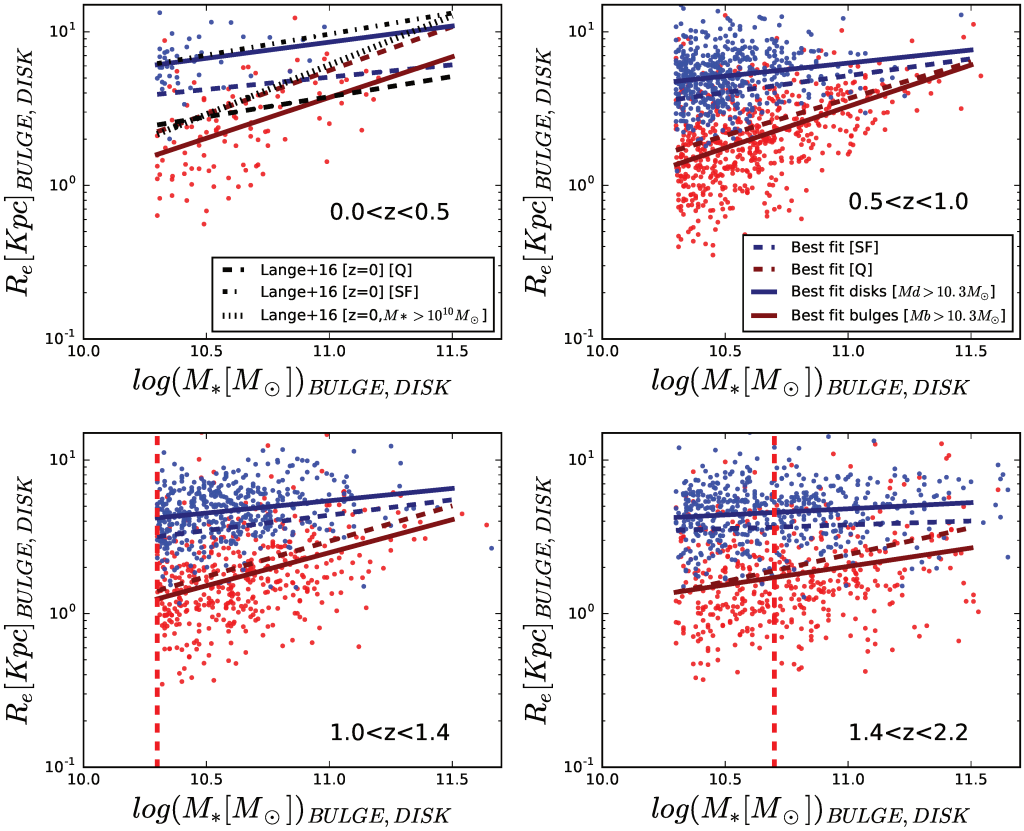

Figure 4.3: Distribution of bulges and disks in the mass-size plane. Blue points are disk components as well as pure disk systems. Red points are bulges and spheroidal systems. Lines are representing the best fits on passive(red) and star forming(blue) distribution while dotted lines are the best fits done on the disks and bulges (respectively blue and red) using different selection as explained in the legend and in the text. Vertical dashed lines are representing the completeness for the bulge and disk sample. In the first panels the dashed-dotted (dashed) black lines show the mass-size relation for all ($M_*/M_\odot > 2 * 10^{10}$) embedded and pure bulges at z $\simeq$0 from Lange et al., 2016.

	Disk								
	$M_d > 2 * 10 M_\odot$			SF_{Disk}			$BT < 0.2$		
z	$log(A)$	α	$\sigma log(R)$	$log(A)$	α	$\sigma log(R)$	$log(A)$	α	$\sigma log(R)$
0.25	0.90	0.21	0.15	0.93	0.33	0.16	0.87	0.13	0.14
0.75	0.77	0.17	0.17	0.77	0.19	0.16	0.74	0.19	0.15
1.20	0.71	0.16	0.17	0.70	0.12	0.16	0.67	0.11	0.16
1.80	0.67	0.08	0.16	0.68	0.10	0.16	0.67	0.04	0.15

Table 4.4: Results from the parametrized fit on the mass size relation for disks wit different selections. 1: all disks with $M_d > 2 * 10^{10} M_\odot$. 2: Disks in star forming galaxies. 3: Disks within galaxies with B/T <0.2.

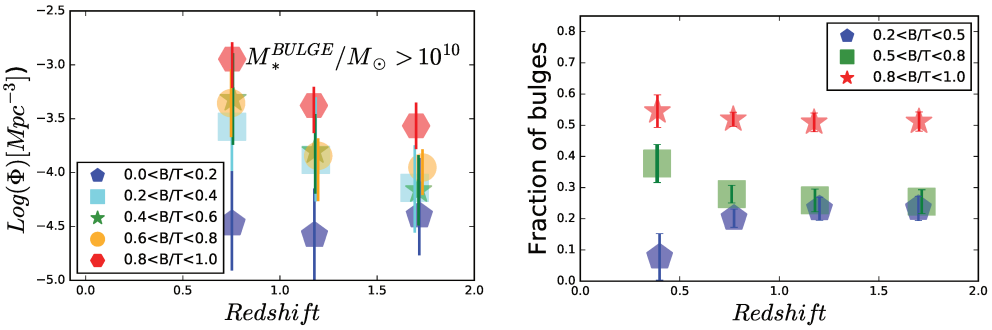

Figure 4.4: Evolution of the number density of bulges ($Log(M_*/M_\odot) > 10$) as a function of B/T. Left panel: Number densities are divided in bins of B/T as labelled. Errors bars are estimated through bootstrapping 1000 times. Right panel: Fraction of bulges at fixed stellar mass in disk dominated and bulge dominated systems. About 25% of bulges with $Log(M_*/M_\odot) > 10$ live in disk dominated galaxies ($B/T < 0.5$).

4.3 Bulges and disks in different morphologies: same formation mechanism?

Massive bulges are present in galaxies with a large variety of morphologies (B/T). This is quantified in figure 4.4 that shows the evolution of the number densities/fraction of massive bulges ($M_*/M_\odot > 10^{10}$) as a function of galaxy morphology. A majority of bulges (∼60%) are in elliptical galaxies (B/T >0.8), while the remaining ∼ 40% of them with similar mass are embedded in disk-dominated galaxies ($B/T < 0.6$). Are their structural properties similar? (some example of bulges in the B/T bin used in this analysis are shown in figure 4.5). Moreover, the number density increases with the redshift for all morphological types, confirming that massive bulges are commonly hosted in galaxies with large disks at all cosmic epochs.

This section is focused on the analysis of bulge and disk properties in different morphologies to investigate whatever there are signs of different formation mechanisms.

Figure 4.6 shows the distribution of bulges and spheroidal systems in the mass-size plane. The different colors indicate different bins of B/T . For galaxies, classified as pure bulges the B/T is set equal to one. The line is the best fit done selecting bulges within galaxies with $B/T > 0.8$.

The following analysis is focused on bulges with $M_* > 2 * 10^{10} M_\odot$, since we assume that this population should be close to the definition of "classical bulges". Taking that definition as a reference, it is interesting to see if there

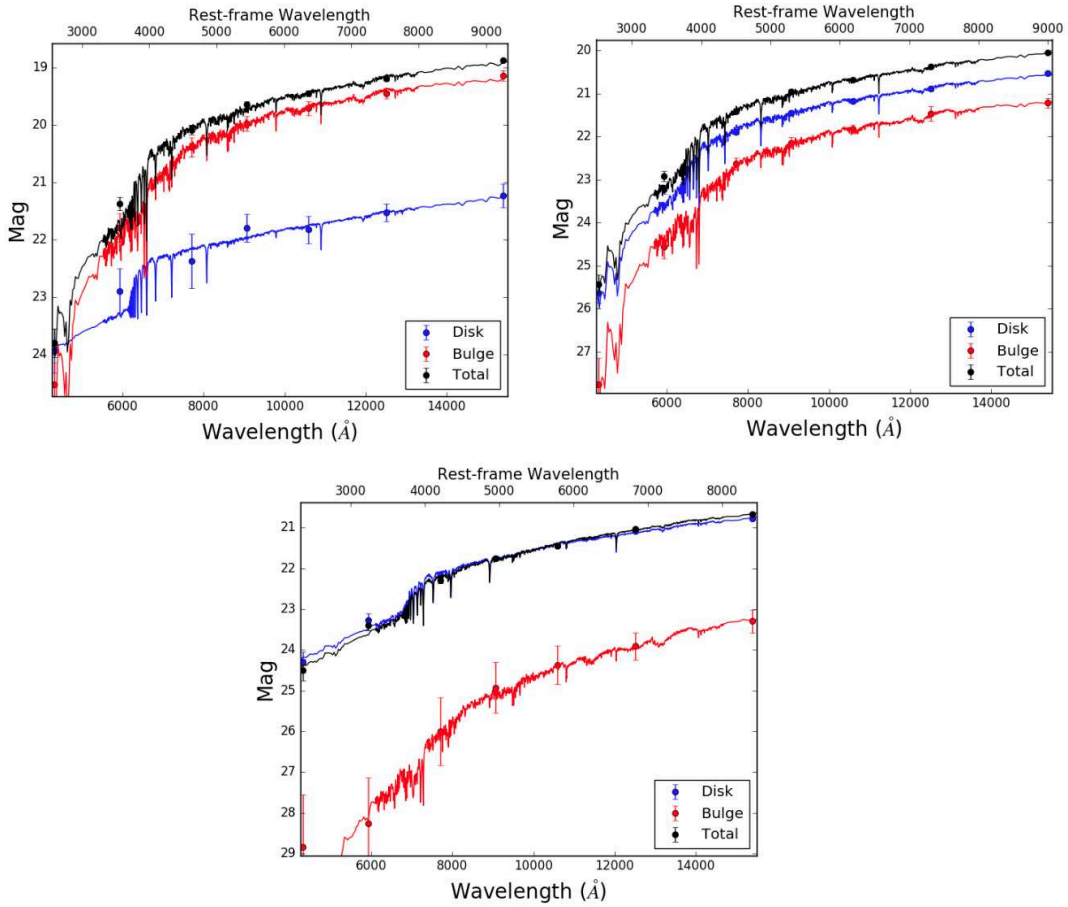

Figure 4.5: Examples of galaxies with different B/T. Top left panel : B/T =0.9 n_b= 6.6, $LogMb_*$=10.8$M_\odot$, top right panel : B/T =0.46 n_b=2.6, $LogMb_*$=10.24 $M_\odot$, bottom panel B/T =0.3, n_b=3.45, $LogMb_*$=10.1 $M_\odot$.

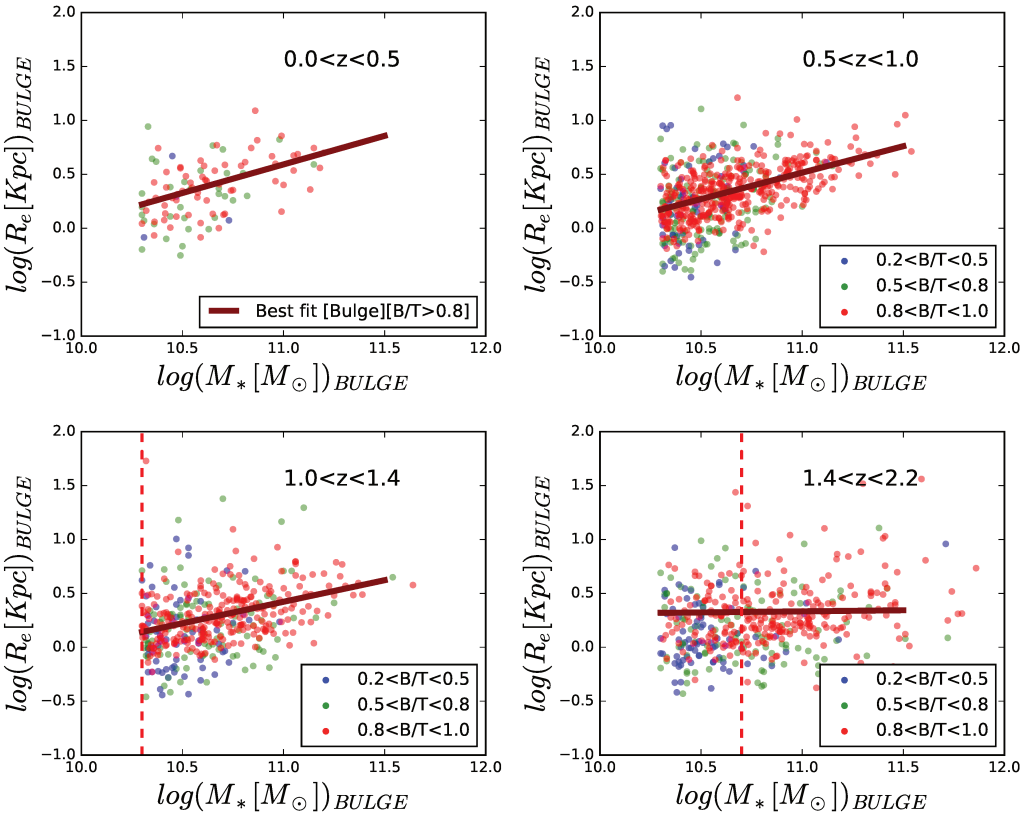

Figure 4.6: Mass-size relation for bulges. The different colors show different bins of B/T as labelled The squares are bulges classified as pseudo-bulges. The solid line shows the best fit done on the bulges within galaxies with B/T >0.8. The vertical red dashed line indicates the completeness limit for the bulge population in each bin.

is any difference on the bulge properties with respect to the morphology of the host.

The distribution of B/T shows a correlation with the stellar mass of the bulge. Galaxies with low B/T tend to have lower mass bulges than galaxies with larger one. This is expected since the sample is mass limited. However, at fixed stellar mass, the half light radii shows a weak correlation with the morphology (B/T).

This result is better quantified in the analysis shown in figure 4.7. Different shapes and colors represent the half light size in bins of B/T at different redshift. The measured size of each galaxy is divided by the expected value from the best fit of bulges in elliptical galaxies (B/T >0.8) at the same mass

and redshifts. This removes the mass dependence and allows to quantify the difference between "classical bulges" and bulges living in more disky systems. By definition the star symbols (B/T >0.8) in the figure are expected to lie in the constant unity line. Every deviation indicates a statistical difference in size between the populations. We found that the size of the bulge, at fixed stellar mass for galaxies with the B/T within the range of [0.2 , 0.8], is independent from the morphology, i.e. it is independent from the disk mass, as can be seen in figure 4.7. However a $\sim$ 20% of systematic difference is measured for bulges in galaxies with $B/T > 0.8$. A possible explanation of that trend can be related to systematic errors in our bulge-disk decompositions. Recall that for objects with B/T>0.8 we used a single Sérsic model while all galaxies with $B/T < 0.8$ are fitted with 2-component models. We checked however that if we remove objects with one component the trend does not change. Moreover the analysis done on the simulation did not show any specific bias for sizes at different B/T . Consequently that results is unlikely related only to a fit problem. An other possible justification can be in the different stellar mass distributions of the bulges. Bulges embedded in disks tend to be less massive than pure bulges. In addition to that at z>1 and $M_* > 2 * 10^{10} M_\odot$ the sample is not complete. To quantify the impact of this effect we test how the trend changes restricting the sample to the more massive systems. Results are shown in the different panels of figure 4.7. The trend remains the same also if we take into account only galaxies with $M_* > 5 * 10^{10} M_\odot$. A possible interpretation is in different formation processes.

Classical bulges are generally assumed to be formed by mergers. Other in-situ processes like violent disk instabilities, especially at high redshift, have been also shown to produce bulges. If different mechanisms are acting at different morphologies (as suggested by several works, i.e. Hopkins et al., 2012), a signature can be left in the structure of the resulting bulge. Indeed the fact that bulges embedded in disks are slightly (20%) smaller at fixed stellar mass than pure ellipticals could be a signature of different formation processes. A comparison with hydrodynamic numerical simulations containing different types of bulges would be an interesting path to follow. I did not have time to properly realize this comparison. Another possible explanation is that pure ellipticals have larger envelopes which create a larger size, because they experienced more merger events. This could be partly probed through the analysis of the Sérsic index. Numerical simulations predict it to be very sensitive to merger events (e.g Nipoti et al 2012), namely it is expected to increase significantly due to (dry) minor mergers. Consequently, if galaxies, with different bulge-to-total ratios, have experienced different merger histories, it might be reflected in the Sérsic index of the bulge compo-

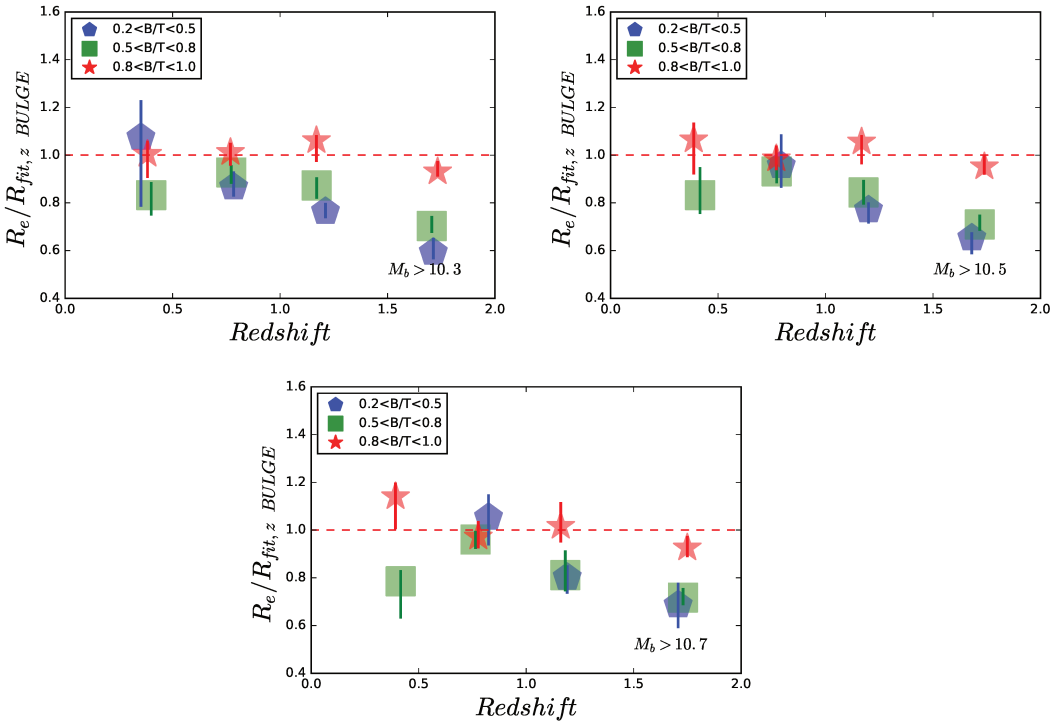

Figure 4.7: Bulge sizes as a function of the redshift. Colors and shapes represent the normalized size for different B/T in redshift bins. The normalization is done dividing each size by the expected value from the best fit (done on the bulges population within galaxies with B/T >0.8).

nent. Figure 4.8 shows the redshift evolution of the median Sérsic index for bulges (F160W) with $log(M_*/M_\odot) > 10.3$ from our catalog. The different symbols represent the various morphological types. An overall increase is observed, from z=2 to z=0.for systems with $B/T > 0.8$, that support the hypothesis of a merger driven growth of the outer envelopes (van Dokkum et al., 2015). However the median Sérsic index of galaxies with lower values of B/T shows a weak if not absent increase with redshift. It suggests either that they had a different formation/evolution but also that they are bulges that rebuilt a disk component with the surrounding gas, decreasing the bulge-to-total ratio. Testing these hypothesis require the knowledge of ages of the internal components. It will be discussed in the next chapter. However, this does not rule out the contribution of merger also for this class of galaxies since several numerical simulations have shown that large disks can survive to these events (e.g Hopkins et al., 2010).

Following the same approach used for the bulge, the analysis is now fo-

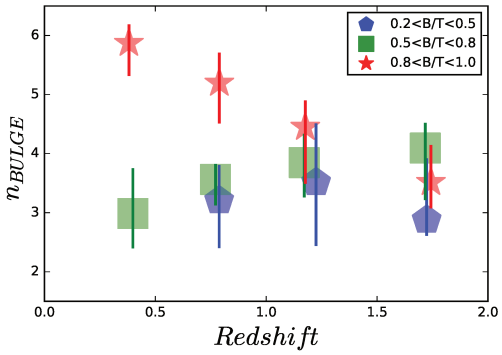

Figure 4.8: Evolution of the median Sérsic index of the bulge in bins of B/T . Errors bars are estimated through bootstrapping (68% confidence level).

cused on the study of the disk structure in different morphologies. Figure 4.9 shows the distribution of the disks in the mass-size plane for three bins of B/T. Galaxies classified as pure disks, are represented here by the half light radii from the 1-component fit and the total mass, and the bulge-to-total ratio is set equal to zero. The red dotted line shows the mass limit for the completeness. The distribution of B/T through this plane shows that massive disks are mostly present in galaxies with low bulge-to-total ratio. While this trend is expected, it is interesting to notice that there is no evidence of a clear correlation between the size and the morphology, at fixed stellar mass. This can be seen also in figure 4.10 which reports the evolution of the size of disks, in bins of B/T. As in the similar previous plot the mass dependence is removed dividing each disk size by the expected value from the best fit done using only disks hosted in galaxies with B/T <0.2. The different symbols indicate different morphologies. Although disks in systems with values of $B/T > 0.5$ appear slightly larger, the measurements are still compatible, indicating that there is no relevant difference in size for disk in different morphology. These results suggest that the presence of the central component, the bulge, does not seem to have an impact on the properties of the disks since no strong difference is observed between pure disks and disks embedded in two component systems.

4.4 Effect of quenching on bulges and disks structure

The second key question is how the bulge growth is related to the shutdown of star-formation and how the quenching affects the inner structure of galaxies.

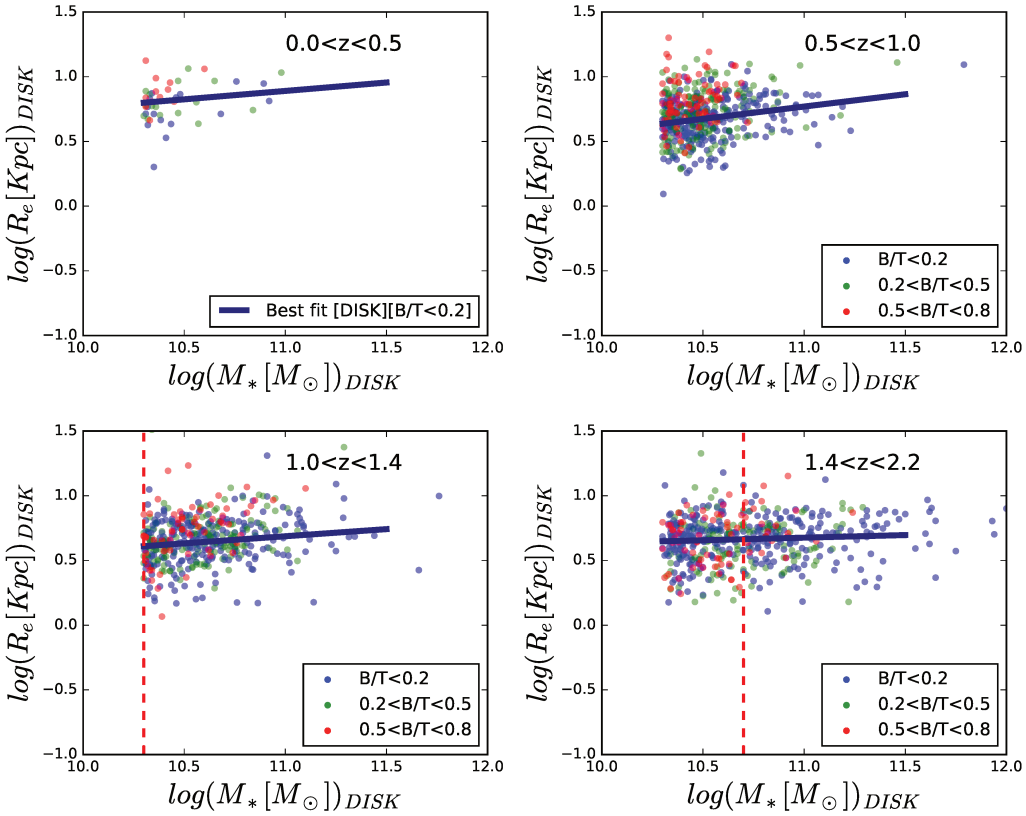

Figure 4.9: Mass size relation for disks. The color code is done using the stellar mass bulge-to-total ratio. The line shows the best fit done on the disk within galaxies with B/T <0.2.The vertical red dashed line indicates the completeness limit for the disk population in each bin.

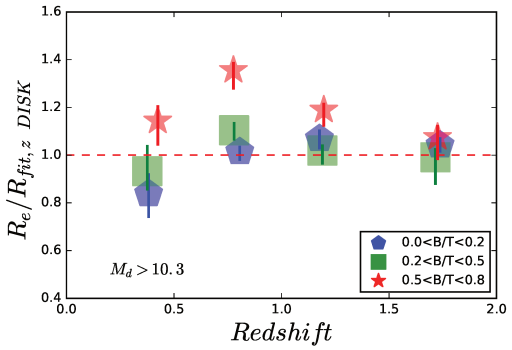

Figure 4.10: Disk sizes in different redshift bins. Colors and shapes represent the median normalized size for different B/T in each redshift bins. The normalization is done dividing each size for the expected value from the best fit (done on the distribution of disk components of galaxies with B/T <0.2).

The following analysis is focused on the study of the properties of bulges and disks hosted in star forming or quiescent galaxies, applying a similar approach as in the previous section.

Figure 4.11 shows again the mass-size relation for bulges, this time divided between star forming and quiescent systems according to the star formation activity of the host galaxy. The selection is done using the UVJ rest-frame color classification (eg.Whitaker et al., 2012). As expected, most of the massive bulges are in quiescent galaxies, while the less massive ones can be found also in star forming systems. The two populations show different distributions. Bulges in quiescent galaxies tend to appear with smaller sizes while the distribution of the ones in star forming systems is extended also at larger sizes. This result is confirmed in figure 4.12. Points here are the median half light size for bulges in star forming (blue) and quiescent (red) galaxies at different redshifts. As in the previous similar plots, each size is normalized by the expected value from the best fit. In this case, since the comparison is between bulges hosted in galaxies with different star formation activities, the best fit is done accounting only for bulges in quiescent systems (however the selection in B/T as discussed in section 3.6 is always applied in order to ensure the completeness and the reliability of the results). A systematic difference is measured between the two populations. Bulges in star forming galaxies are always larger ($\simeq$ 20 - 30%) than the ones in quiescent systems. A first explanation can be the presence of a bias in the fit. Since most of the star forming galaxies are disk dominated systems, the model of the bulge component can be contaminated by a fraction of the light from the bright disk. However the simulations show that the uncertainties on the size

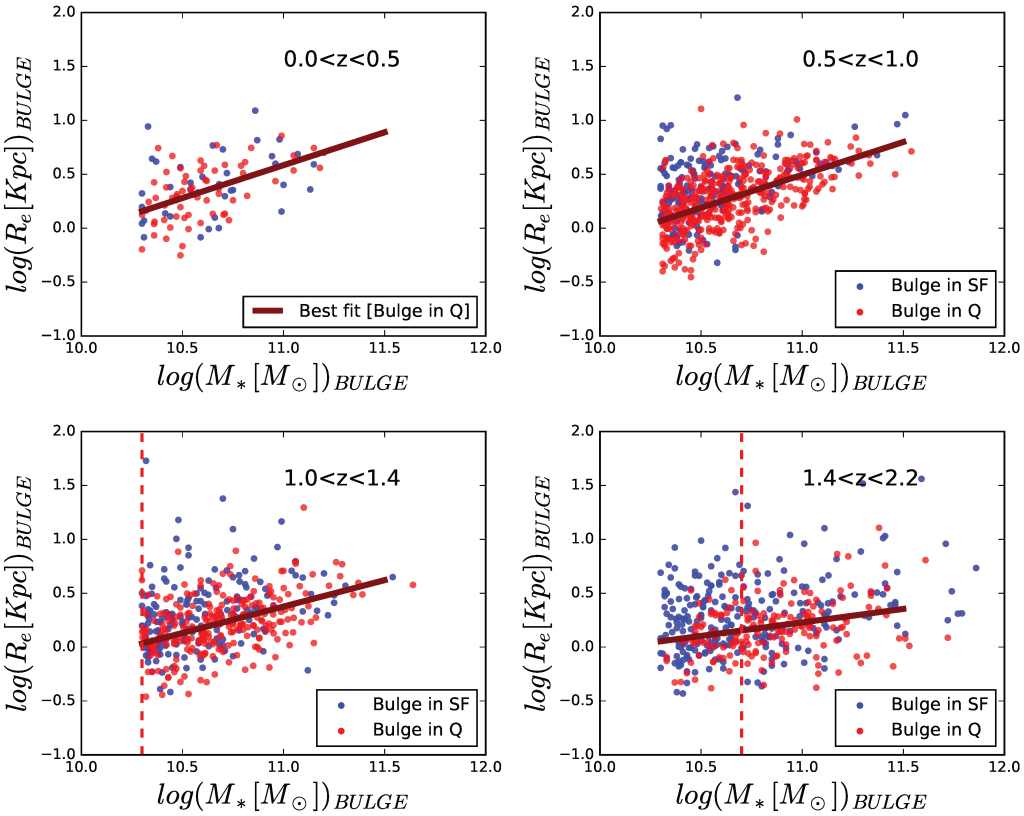

Figure 4.11: Distribution of bulges in the mass size plane. The colors represent the star formation activity of the host galaxy. The red line shows the best fit done on the distribution of bulges within quiescent galaxies.The vertical red dashed line indicates the completeness limit for the bulge population in each bin.

estimation in these cases is lower than 20%. Since the shift observed is larger, the uncertainties of the method cannot be the only explanation. As discussed before such difference can be enhanced by the mass distribution of bulges in star forming and quiescent galaxies. We tested that restricting the analysis to more massive galaxies the general trend does not change. Before moving to the interpretation of this result I will analyze the properties of the disk in order to have a complete picture.

Figure 4.13 shows the distribution of disks, represented here in red and in blue depending on whether they are hosted by a quiescent or star-forming galaxies. Lines are the best fit done on disks from star forming galaxies. Again in this series of plots, there is a lack of correlation between the disk structure and the properties of the entire galaxy, in this case the star forma-

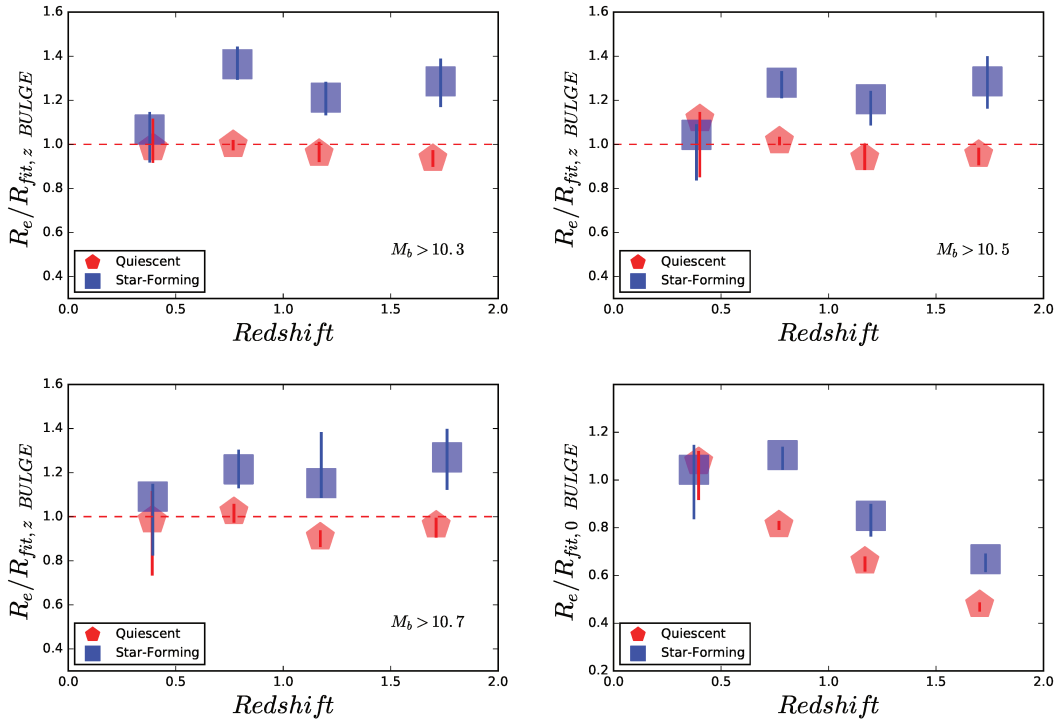

Figure 4.12: Bulge sizes as a function of the redshift. The two panels are showing the comparison between normalized bulge sizes in star forming and quiescent galaxies. The normalization is done dividing by the expected value from best fit of the distribution of bulges within quiescent galaxies. Right panel shows the same analysis with sizes normalized using the best fit at z=0 in order to show the deacrease with the redshift.

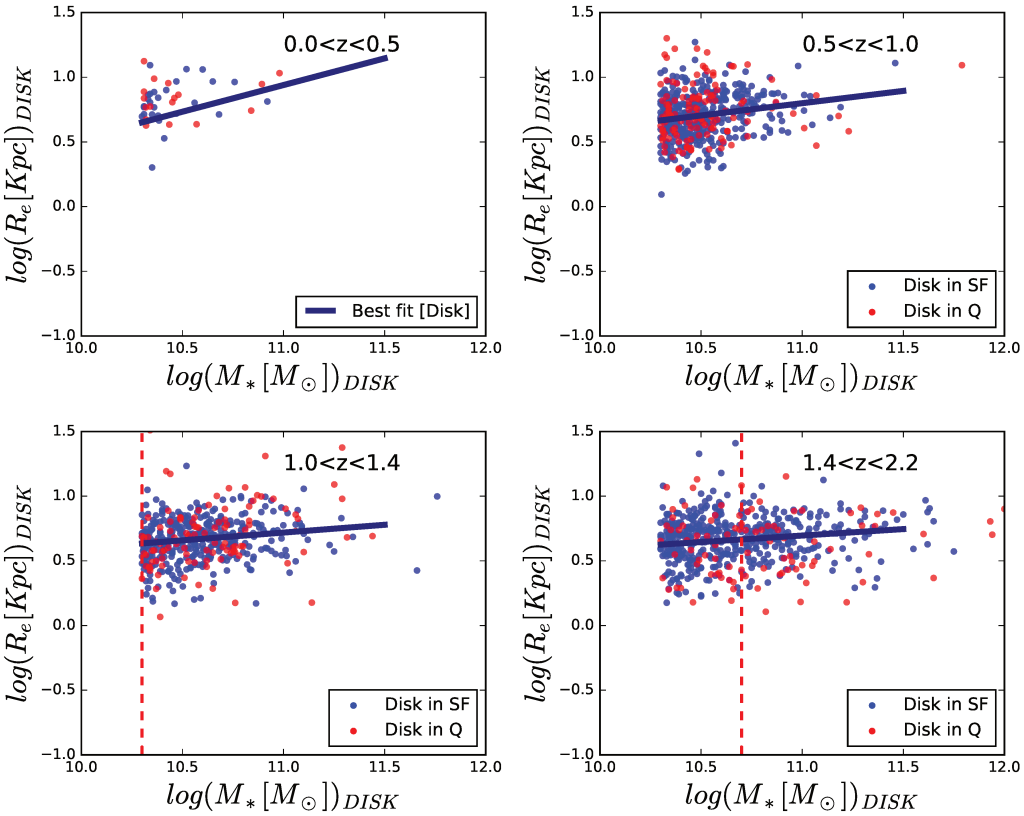

Figure 4.13: Mass-size relation for disks. The disk population is divided in star forming (blue) or quiescent (red). The classification is done using the standard UVJ color of the host galaxy. Lines are the same of the previous figure (4.9)The vertical red dashed line indicates the completeness limit for the disk population in each bin.

tion activity. The same result is also found in the analysis shown in figure 4.14. The left panel represents normalized sizes in redshift bins. Overall the sizes of the two populations are compatible in the redshift range probed by our data.

Summarizing, bulges are systematically smaller in quiescent galaxies than in star forming systems. The disk component does not show any structural change if the host galaxy is star forming or quenched. It suggests that the eventual structural changes due to quenching are confined in the bulge component. If the disk is present, it does not seem to be affected.

The right panels of figures 4.12, 4.14 show the median size normalized by the best fit at z=0 in order to estimate the size increase as a function of

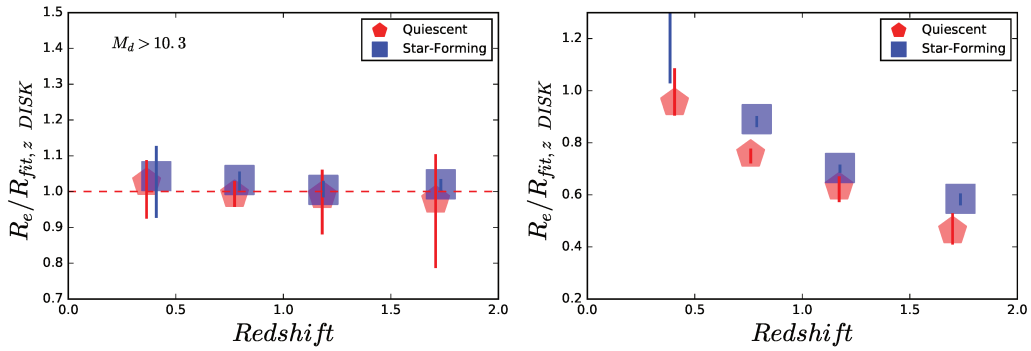

Figure 4.14: Median size of disks in star forming and quiescent galaxies. The normalization is done dividing each size by the best fit of the distribution of disk within star forming galaxies. Right panel shows the same analysis with sizes normalized using the best fit at z=0 in order to show the decrease with the redshift.

redshift. Bulge sizes either in star forming or quiescent systems increase by a factor of $\simeq 0.5$ between $0 < z < 2$, while there is a constant size difference between the two populations. For the disks no clear difference is seen between the two trends.

A possible interpretation is that bulges experience an additional morphological transformation during or after quenching. Indeed bulges in quiescent systems come from galaxies that were star forming in the previous epochs, thus the comparison of the sizes in star forming and the quiescent systems in bins of redshift, support the interpretation for which moving to the passive region they reduce the size passing through phase of morphological transformation.

However results shown here can also be affected by the progenitor bias effect (Carollo et al, 2013, Lilly & Carollo, 2016). Observed bulges in passive galaxies at a given epoch are more compact because they arise from a population of bulges in star forming systems that quenched few Gyrs back and therefore were more compact. Hence the size evolutions is dominated by observational effects.

Chapter 5

Constraints on the formation processes of bulges and disks using the stellar population properties

Contents

5.1 Star forming main sequence 103

5.2 Colors as a proxy of the star formation activity . 107

5.2.1 Comparison with CANDELS 111

5.2.2 Colors of bulges and disks 111

5.3 Discussion 112

The analysis of the previous chapter was focused on comparing structural properties of bulges and disks living in galaxies with different morphologies and star-formation rates. Following the same purpose in this chapter I will analyze the stellar population properties, like mass, ages, colors, for bulges and disks in star forming and quiescent systems to investigate their role in the quenching process and to put constraints on their formation timescale.

5.1 Star forming main sequence

There are different methods to estimate the SFR of galaxies. One of them is trough the fit of the Spectral Energy Distribution (as introduced in chapter 2). It requires an optimal set of data covering large range of wavelength

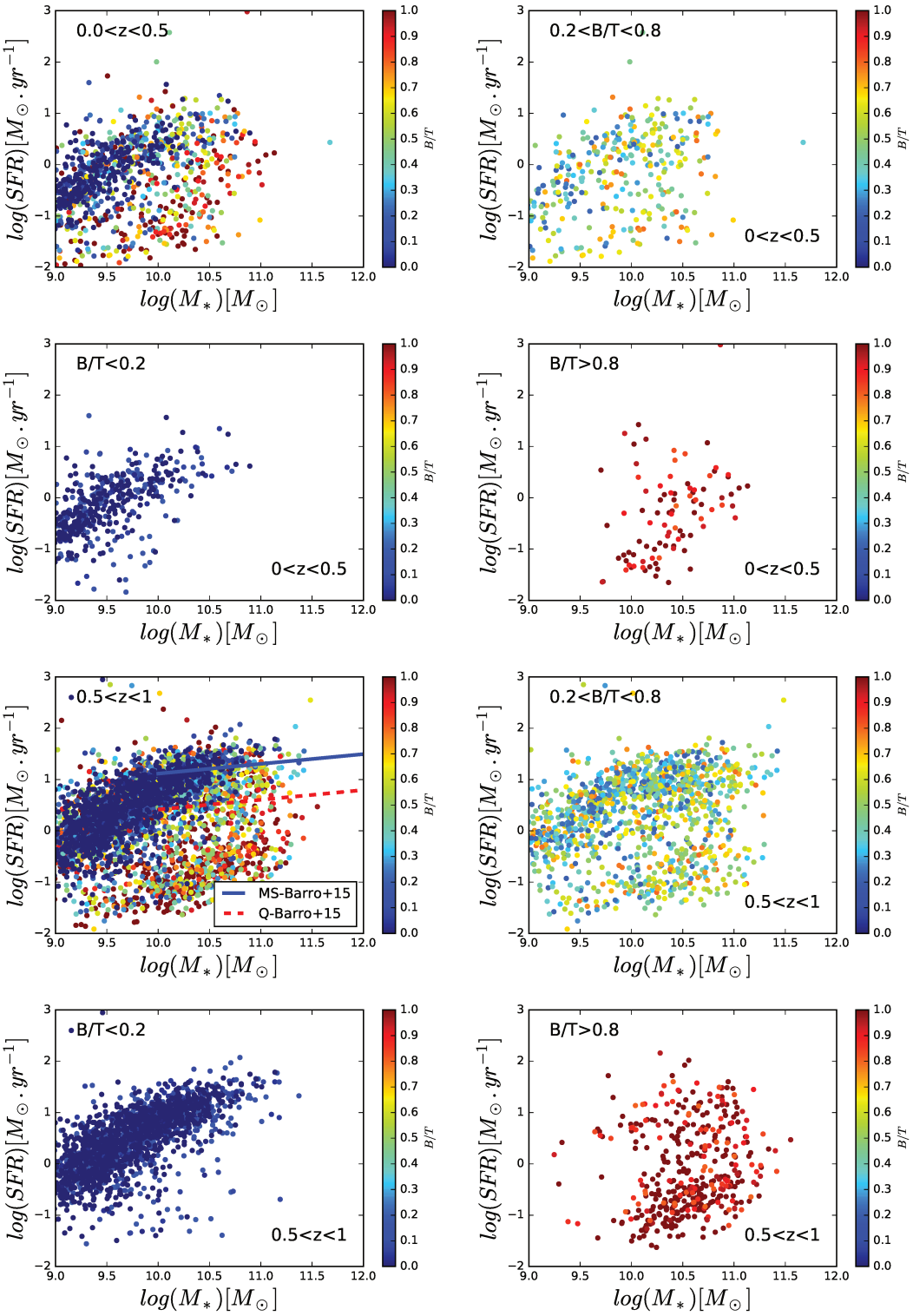

Figure 5.1: Distribution of galaxies in the $M_* - SFR$ plane. The color code indicates the Bulge-over-Total ratio in mass. Different panels show various selection in B/T as explained in the labels.

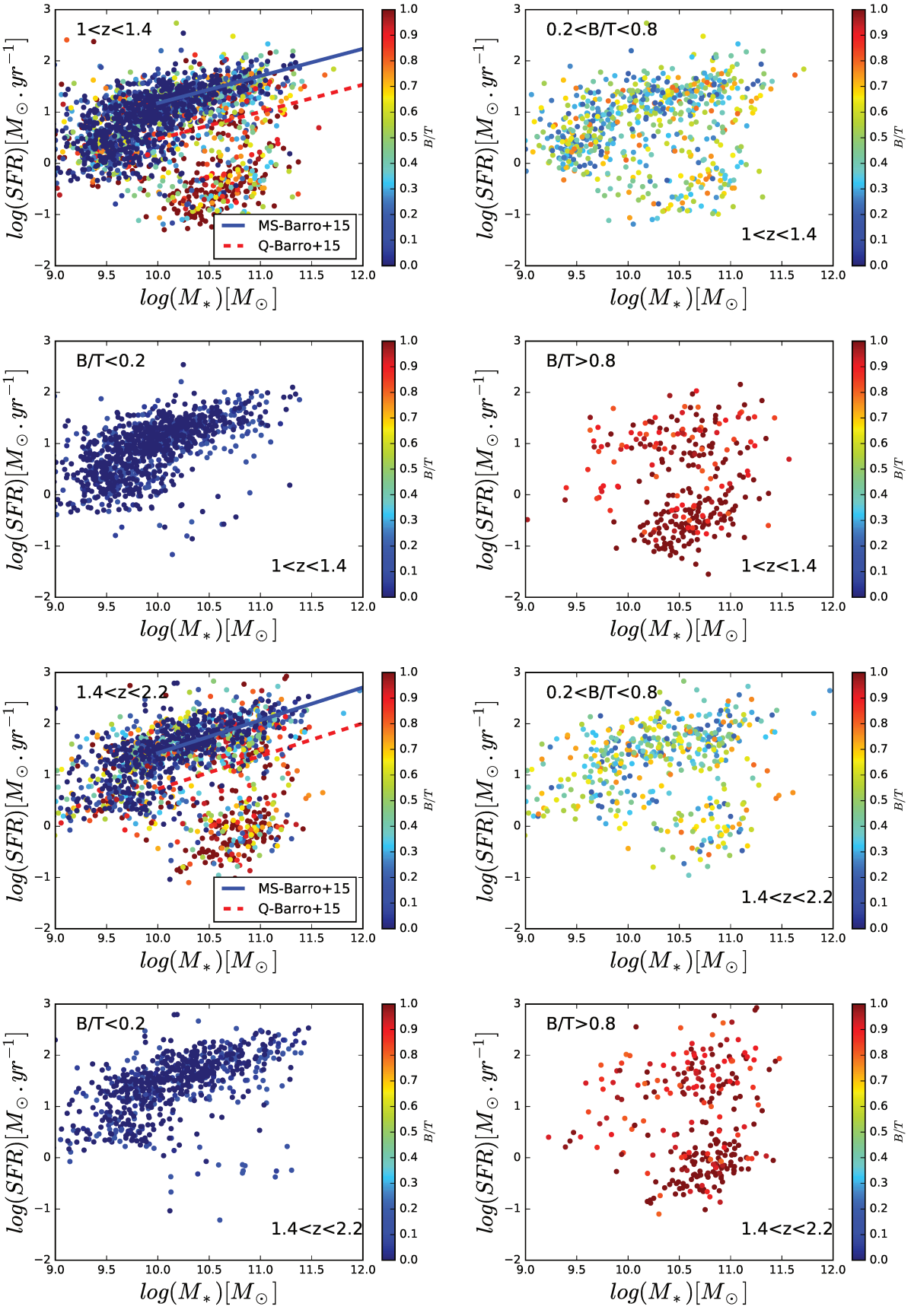

Figure 5.2: Distribution of galaxies in the $M_* - SFR$ plane. The color code indicates the Bulge-over-Total ratio in mass. Different panels show various selection in B/T as explained in the labels.

from the IR to UV. However infer directly the star formation activity from the SED fitting is challenging due to the degeneracy that exist between the specific Star Formation Rate (sSFR) and the dust. The dust absorbs light from the young stars to then re-emit it in the infrared reddening the profile. Hence a galaxy can be star forming but its spectra is reddened by the dust. The SFR, used in the following analysis, are global values taken from the CANDELS catalog. They are estimated from the SED fitting as explained in Barro et al., 2017. Namely they are computed by combining IR and UV rest-frame luminosity as described by the following equation: $SFR_{UV+IR} = 1.09 \cdot 10^{-10}(L_{IR} + 3.3 \cdot L_{2800})[M_{\odot} yr^{-1}]$

Galaxies in the $M_* - SFR$ plane follow a bimodal distribution. Star forming galaxies populate the main sequence while the quiescent one dominate the massive region. This is represented in the ensemble of figures 5.1-5.2. The color code indicates the B/T, representative of the morphology. From these sequence of panels we notice that almost all the disky galaxies (B/T <0.2) lie in the main sequence while the majority of the spheroidal systems (B/T >0.8) are in the quiescent region. This division can be interpreted as a signature of mechanisms that destruct the disk lading to quenched bulge dominated galaxies, like major mergers. However there is a population of "blue" purely bulge dominated systems. They are candidate to be the blue nuggets. As already seen in previous works (Dekel et al., 2009, Zolotov et al., 2015, Barro et al, 2014), they are interpreted as the results of a compaction phase that precedes the quenching. Both results suggest that the growth of the bulge component somehow precede the quenching as also discussed in Lang et al [2014]. In this work they show that the B/T ratio increases along the MS, pointing out that the bulge growth precedes quenching of the star formation activity. In agreement with that, in the chapter 4 it was already shown how the structure of the internal components differs depending on the star-formation activity of the host galaxy, suggesting a possible morphological transformation connected to the quenching phase.

Speculating a bit more on that, we can also say that the absence of pure disks galaxies in the passive region suggests that a quenching channel without any bulge growth is not a common channel at least in the general field environment probed by our data. However it does not discard the existence of passive disks observed in other works (see for example Toft et al. [2017]) and predicted by simulations (halo-mass quenching scenario Dekel & Burkert, 2014, Cattaneo et al., 2008) in groups and clusters.

Between these two extreme cases there is a population of intermediate B/T systems. Their distribution on the SFR-mass plane reveals a class of objects that host a bulge component while they are still in the main sequence.

While this result is somehow expected for classical spiral galaxies, it is interesting to notice that in this range of B/T galaxies are distributed either in the star forming or in the quiescent region. Hence, at fixed stellar mass, they appear with the same morphology, in terms of B/T , but they have different star formation activity. This result first supports what it is suggested in the previous chapter, that massive bulges hosted by a disky galaxy are common cases, independently of whether the host galaxy is star-forming or not. However they can be either star forming galaxies that are growing a central density, but also bulges, already formed and quenched, that are re-accreating the disk component. A deep analysis in this sense requires the knowledge of ages for both components.

5.2 Colors as a proxy of the star formation activity

In the previous section I analyzed the relation between integrated SFR and morphology. The aim of this section is now to resolve the star-formation activity within the galaxies. Our catalog, described in chapter 3, contains the SED derived properties of bulges and disks. As previously explained, a proper estimation of SFR requires wavelength coverage from FIR to UV, which is not available for our decomposed SEDs. Indeed the analysis is restricted to optical - NIR bands (430-1600 nm). An alternative proxy for the sSFR, which is less affected by modeling uncertainties, are rest-frame colors. However they are affected by the existing degeneracy between the sSFR and the dust. Hence a galaxy can be star forming but its spectra is reddened by the dust. To solve this issue the UVJ selection is often used. The gradient that dust and the sSFR show on this plane defines a star forming and quiescent region that allows to classify galaxies depending on their position in the plane (see fig 5.3). For that reason the rest-frame colors can be used as a proxy of the specific star formation rate.

To estimate the colors I relied on the theoretical profile computed by FAST, I convolved the SED model with the transmission curves of HST filters to recover the flux that corresponds to the U,V,J,I wavelength rest-frame. In this analysis I decided to restrict the sample. I used only galaxies from GOODS-N/S fields since they are covered by seven filters instead of four. This condition provides more constraints on the Spectral Energy Distribution.

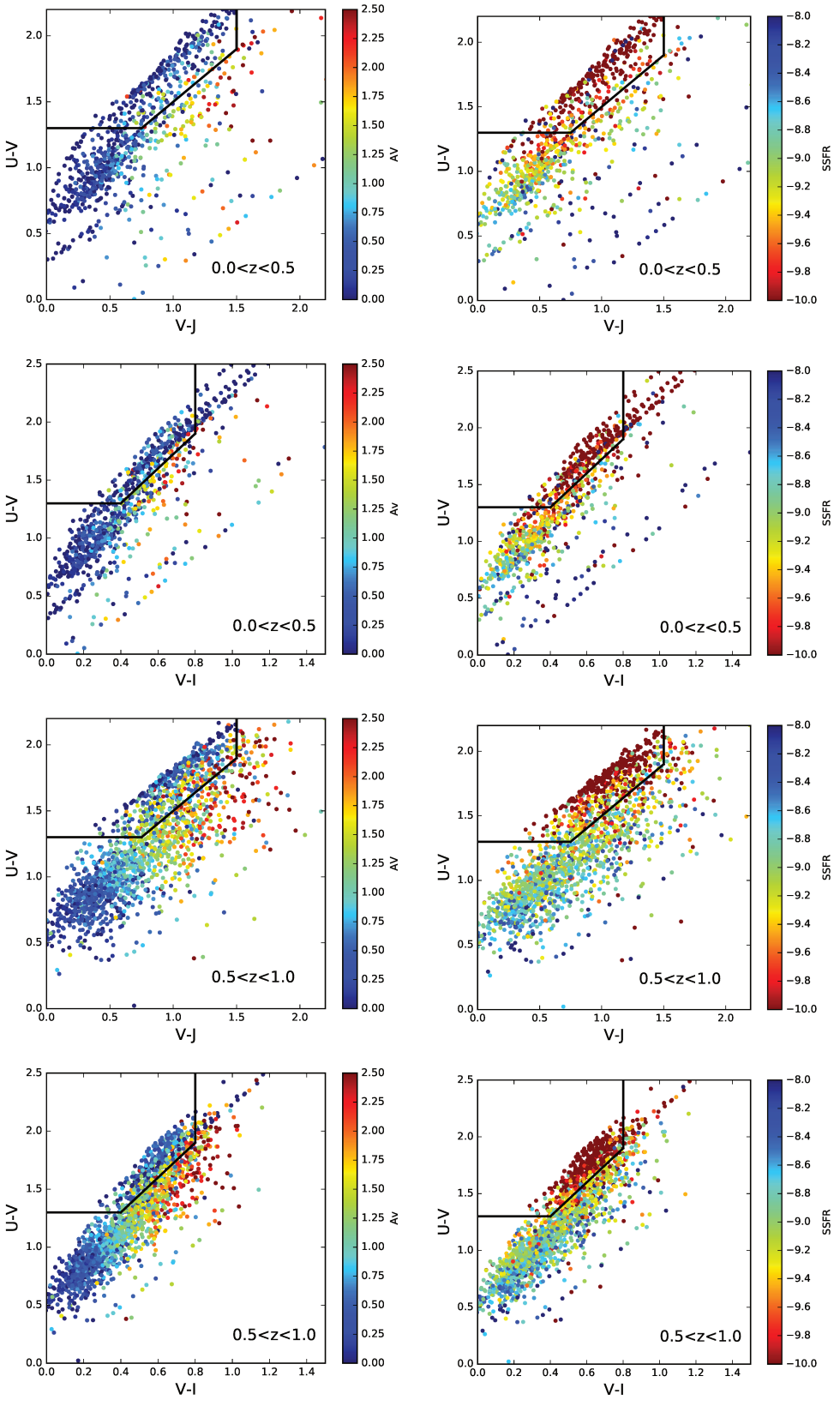

Figure 5.3: Color diagrams for GOODS-N/S sample. Rest-frame colors are extrapolated from the SED model computed by FAST. The color code is done using the extinction (A_v) and the sSFR taken from the CANDELS catalog. Black lines are the boundary to define the star forming and the quiescent region.

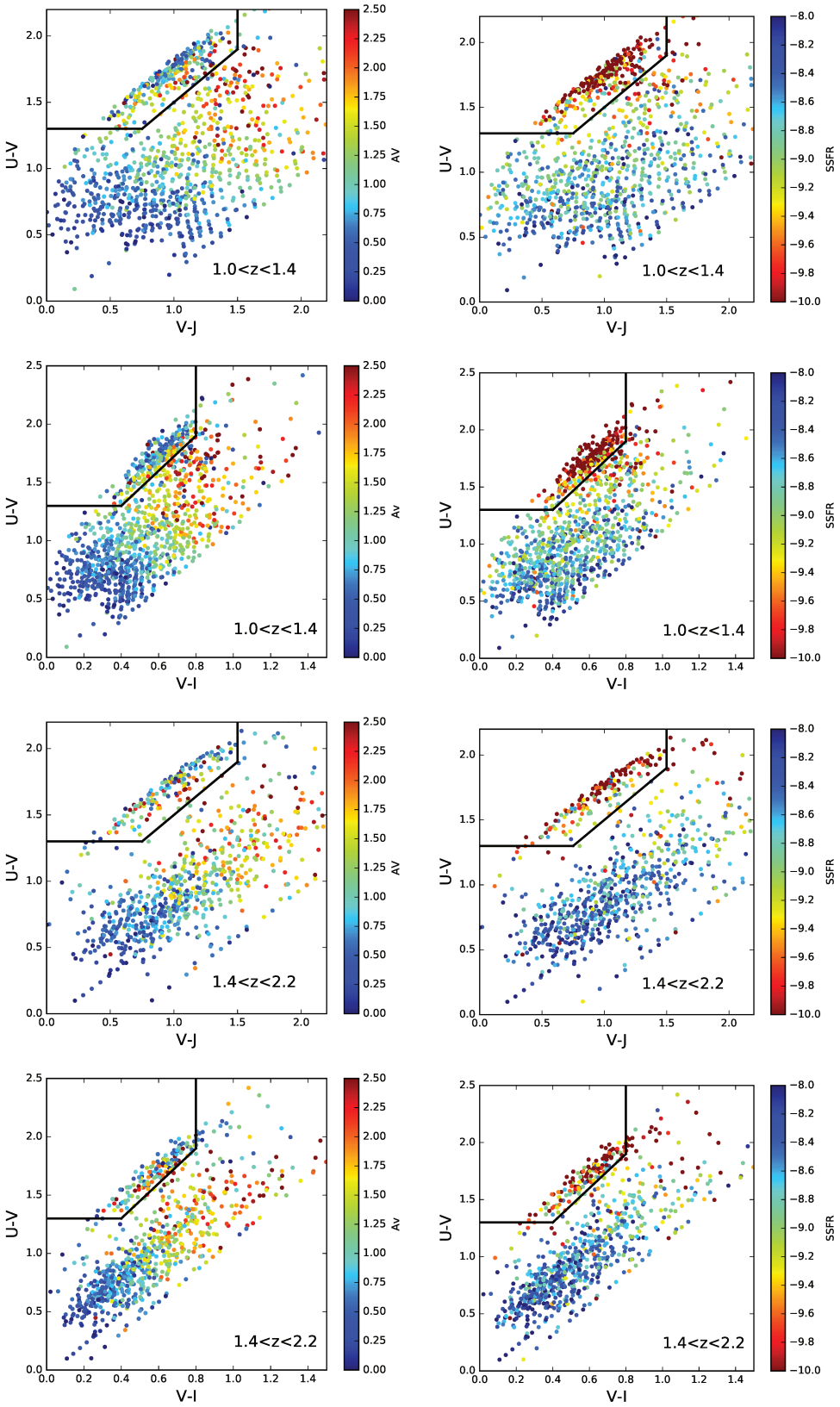

Figure 5.4: Color diagrams for GOODS-N/S sample. Rest-frame colors are extrapolated from the SED model computed by FAST. The color code is done using the extinction (A_v) and the sSFR taken from the CANDELS catalog. Black lines are the boundary to define the star forming and the quiescent region.

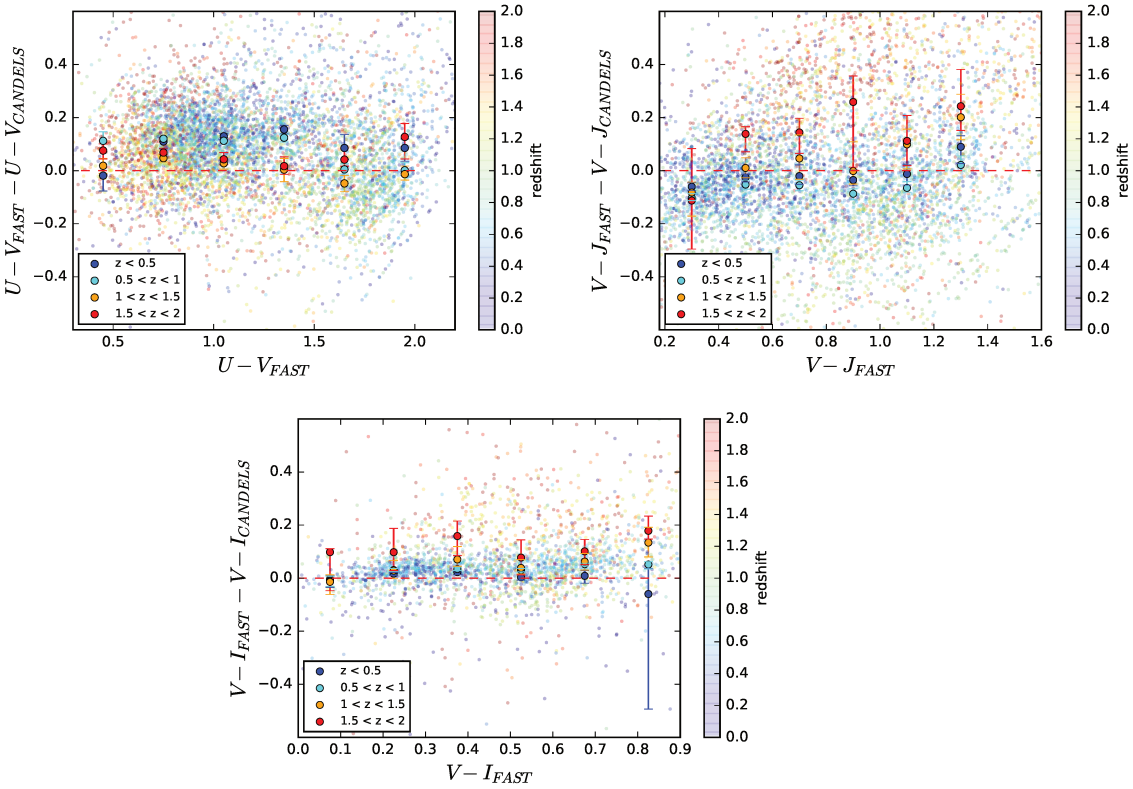

Figure 5.5: Comparison between U-V (left), V-J (right) and V-I (bottom) rest-frame colors from the CANDELS catalog and the one estimated in this work.

5.2.1 Comparison with CANDELS

As a preliminary sanity check, I compare the U-V, V-J and V-I colors of the full galaxies derived in this work to the ones from the CANDELS catalog (larger wavelength coverage). The color code is representative of the redshift bins (see figure 5.5). The U-V color is well recovered in all the redshift bins. Although there is a bias of $\simeq 0.1$ at lower redshift. The V-J value instead is well estimated at low redshift, while for z>1.5 the measurements start to be biased by more than 0.2, and it increases at high redshifts. This trend is expected since the method used to infer the colors is based on the interpolation from the theoretical profile produced by FAST. The J band rest frame, in the high redshift bin probed (z=2) in this work falls at 3600 nm while the last band available is the H-band (1600 nm), thus since it is outside of the observed data, the SED in this range is not well constrained. To solve this issue I used an alternative color diagram replacing the J band with a bluer one, the I band, as it is done in Wang et al. [2017]. Indeed, using the present method the I band rest frame is better constrained in the SED fitting thus better recovered than the J band as can be seen in the bottom panel of figure 5.5. The UVI plane has similar properties than UVJ as shown in figures 5.3-5.4. Each figure is done for a given redshift bin and contains a sequence of four panels that show the UVJ and UVI plane color coded by the extinction and the sSFR (the latter quantities are taken from the CANDELS catalog). It can be seen that both quantities show the same trend in the two color-color planes, as well as it can be noticed that the distribution of galaxies in the UVI plane is less scattered due to the fact that the I band rest frame is better recovered than the J band rest frame in the last redshift bin.

5.2.2 Colors of bulges and disks

This section is focused on a selected sample of galaxies that have $0.2 \leq B/T \leq 0.8$. As previously shown they appear with similar morphology, i.e. the same bulge fraction, but they show different star formation activities. It is indeed interesting to investigate the state of the star formation activity of bulges and disks among this population, since they are optimal candidates to explore how the quenching is acting within galaxies. Figure 5.6 shows the color distribution of bulges and disks in the UVJ/I plane. The sample is divided between star forming and quiescent using the UVJ selection on the color of the host galaxy. Hence the sequence of panels on the left and on the right represent respectively bulges and disks in star forming and quiescent galaxies. The star symbols are the median value of the distribution. The

black stars values are estimated using the color on the full galaxies , while the grey symbols are the median colors from the CANDELS catalog and they are here reported as a comparison. It is interesting to notice that the total color is always in between the median color of the two components. This is expected, since the final color is the result of a combination of the contribution by the internal components. Indeed it is a good test to check the reliability of the measurements.

Recall that only galaxies with $log(M_*) > 10.3 M_\odot$ are considered in these series of plots, in order to not to be affected by incompleteness. Different color distributions are observed between the two components and also for the same component hosted in star forming or passive galaxies. Disks are generally blue in star forming galaxies, but also close to the quiescent region in the UVJ plane. This is expected since we are considering massive galaxies. Bulges tend to be redder and dusty. However, the fact that they appear redder than the disk cannot be related only to the dust reddening since the shift in color between the two component is not parallel to the Av gradient, as it is shown in the two panels of figure 5.7. Thus they are dusty but also with a lower sSFR respect to the disk. In quiescent systems both components lie in the quiescent region.

These trends are also seen in the analysis shown in figure 5.8. The two panels represents the median U-V colors as a function of redshift. Bulges in star forming and quiescent systems show similar trend across all epochs. This population is here divided in two subclasses : massive bulges ($logM_b > 10 M_\odot$) and not massive ($log(M_b) < 10 M_\odot$). This is done because, as explained in the previous chapter, this class of bulges populate the low mass end of the mass-size plane where the relation tends to be flat. This can be due to the fact that they follow a different relation or because the limit of the method is reached and their properties are dominated by systematic/errors, thus they can affect the final results. For this reason I decided to keep two distinct classes. However figure 5.8 shows that also such bulges in star forming and quiescent systems follow a similar trends. Differently the disks are blue in star forming systems and show a red color in quiescent galaxies.

5.3 Discussion

The key question that we want to investigate with the present analysis is how galaxies quench and what is the link between the quenching and the growth of the bulge. Several quenching mechanisms are proposed. They can be divided in mass and environmental quenching. The latter one contains process that are exclusive for satellite galaxies. In the mass quenching cat-

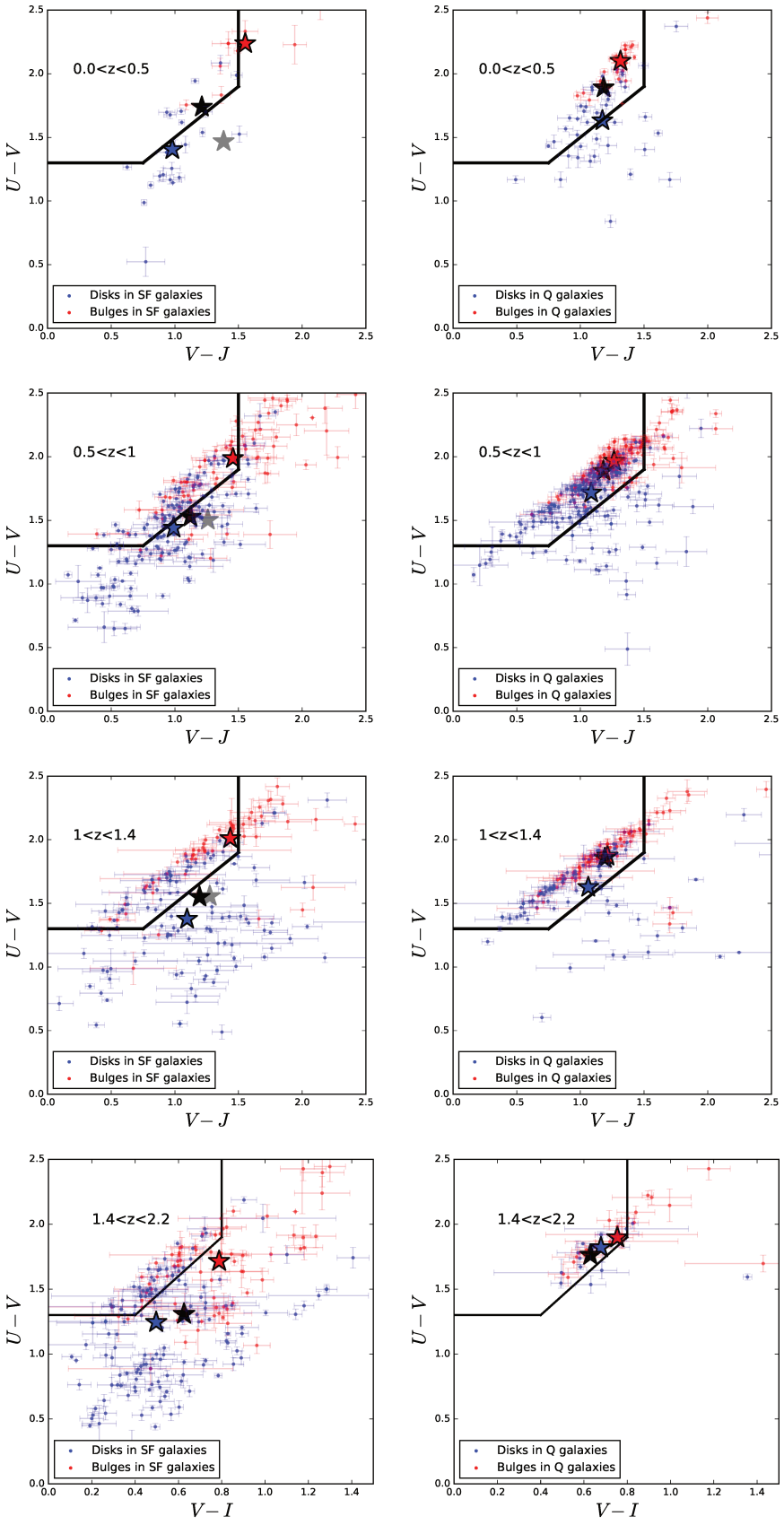

Figure 5.6: Color distributions of bulges and disks in star forming (left) and quiescent (right) galaxies in the UVJ/UVI plane. The blue and the red star are the median value for bulges and disks respectively. The black one is the median color estimated using the CANDELS catalog.

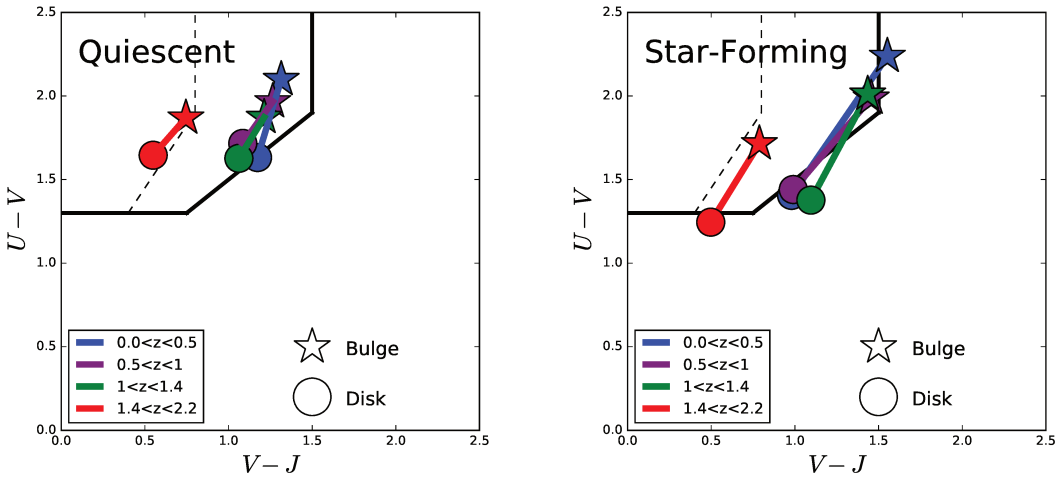

Figure 5.7: Summary of the bulges and disks color in the UVJ/I plane in different redshift. The dotted lines are defining the quiescent region in the UVI plane.

egory there is variety of processes that act either in remove the gas from the galaxy or preventing the present/inflowing gas to form stars. They can be internal process as the AGN/supernova feedback. The energy released increases the gas temperature preventing the star formation. Moreover some external process as the thermal shock, due to the mass of the halo, can act to halt the accretion of new gas.

Also a galaxy can quench by itself growing the bulge. Indeed the accretion of a central density will stabilize the gas present in the disk, preventing new star formation events (morphological quenching Martig et al., 2009). Even though several works already shown the existence of a correlation between the morphology and the star formation activity (Wuyts et al., 2011, Huertas-Company et al., 2015, Whitaker et al., 2016) the link between the growth of the central bulge and the quenching is still not well understood. Recents works also pointed out as the presence of a central density is preliminary step for a galaxy to quench (Barro et al, 2015, Lang et al, 2014, Bluck et al., 2014).

In this context results from this work show an evidence of galaxies hosting bulges already in the main sequence (B/T >0.2) as well as a lack of passive bulgeless galaxies. It supports the idea that the presence of the bulge is a required condition for a galaxy to quench.

The analysis of the color shows that almost all galaxies in our sample present negative color gradients. Indeed all bulges are redder than the disk.

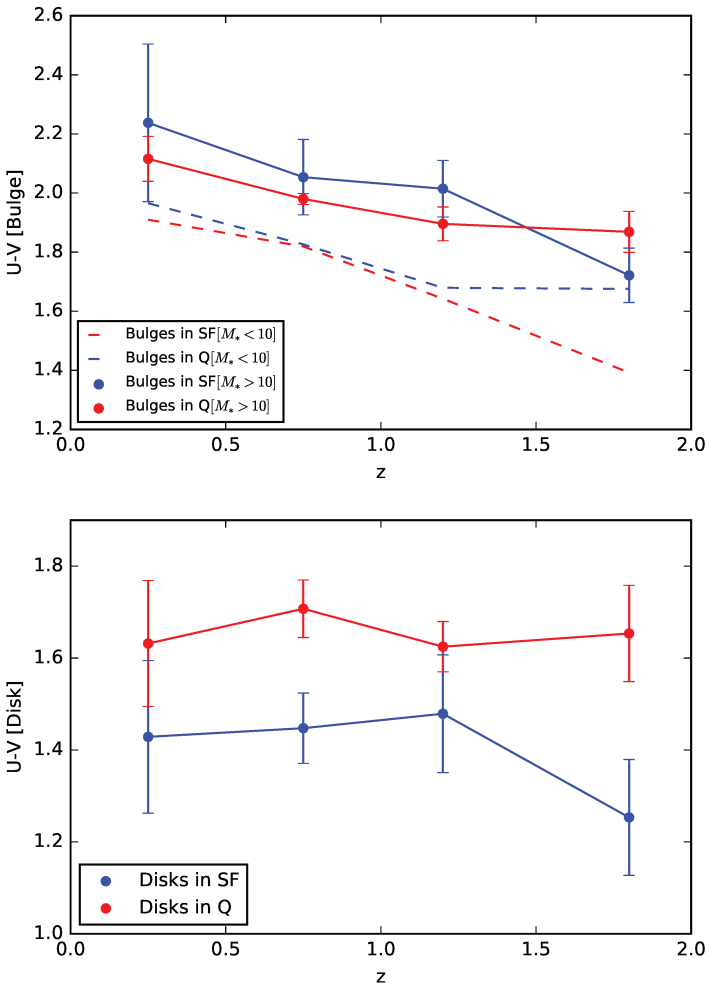

Figure 5.8: Color distribution of bulges (top) and disks (bottom) in star forming and quiescent systems at different redshift. Only galaxies with $M_* > 10M_\odot$ are considered here. Bulges are divided in two populations

This is seen in bulge/disk dominated systems as well as in the case of a double components galaxies. In the context of the quenching scenario, the present results are in disagreement with a constant decrease of the sSFR at all radii. Indeed the different color of disks in star forming and quiescent galaxies, and the lack of passive bulgeless galaxies, support the idea that the central component is built before the galaxy will moves into the passive region, compatible with the morphological quenching scenario. Moreover bulges have similar color in star forming and quenched galaxies. It can be interpreted as that bulges, at all redshift and in star forming systems, are already built and are starting to quench, while the disk is still star forming. Consequently galaxies start to quench from the central region in agreement with a scenario of inside-out quenching introduced by previous works (Tacchella et al., 2016).

Chapter 6

Conclusions

Explaining the existence of the two main populations of galaxies is one of the most challenging tasks in the field of galaxy evolution, i.e. constraining the mechanisms that regulate star-formation in galaxies. The bimodal distribution of the structural properties as well as stellar masses, colors, SFR, etc. suggests a link between the morphological structures and the quenching processes. In the actual state of the art the origin of this correlation is still debated. Do galaxies start to quench from the inside? Do bulges grow in the main sequence? Is there a link between the bulge growth and the quenching? Proper answers to these questions requires to resolve properties of internal components of galaxies at different epochs.

Following that purpose I performed bulge-disk decompositions of the surface brightness profile of $\simeq 17'300$ galaxies (F160W < 23, $0 < z < 2$) in 4-7 filters, covering a spectral range of 430-1600 nm. I used data from the CANDELS survey, optimal dataset for this kind of analysis due to the high spatial resolution and the multi-wavelength coverage.

In order to test the global accuracy of the fits I used a set of $\simeq 4000$ mok galaxies generated by the sum of two analytical profiles. Applying the same analysis as for the real data I firstly estimated the magnitude limit of the method (or S/N) to then show that the derived structural parameters of bulges and disks are globally unbiased below this value.

One challenge of this kind of analysis is in the choice between a single or a double component model to reproduce the surface brightness profile. After exploring different methods, we finally decided to use a novel selection algorithm based on the deep-learning. This kind of approach allows to make an a-priori selection of the best profile. It reduces contaminations from wrong fits or unphysical models caused by the second profile, not always needed. The result of such kind of classification is that the light profile of $\simeq 20\%$ of galaxies in the sample is well reproduced by an exponential disk model,

while 15% prefer a Sérsic profile with n>2. The remaining fraction, almost the 70% of the sample, requires a double profile.

In the following step, I fitted the 4-7 points Spectral Energy Distributions with stellar population models (BC03) of disks and bulges independently to obtain informations as stellar masses, rest-frame colors etc. The ensemble of the previous procedures results in a catalog that contains structural/morphological informations together with the stellar population properties for a large sample of bulges and disks within galaxies, which is released to the community [1]. This is the largest and more complete catalog of bulge-disk decompositions up to $z = 2$.

In the second part of the thesis I used the derived catalog to analyze separately the distributions of bulges and disks in the mass-size plane, from z∼2 to z∼0.2, in order to put additional constraints on their formation mechanisms. I found that bulges and disks follow different relations at all epochs. Their distributions is very similar to the ones observed for passive and star-forming galaxies from a 1-component fit. This agreement reflects the fact that the majority of quenched galaxies are bulge dominated while star-forming galaxies are disk dominated. Consequently the scaling relations of star forming/quiescent galaxies are mainly guided by their dominant component.

Interestingly, I found that massive disk ($M_{*,d} > 2 * 10^{10} M_{\odot}$) size does not show a strong dependence with the morphology of the host galaxies. Hence at fixed stellar mass pure disk systems or disk embedded in bulge dominated systems have similar sizes. The presence/built of the central density does not seem to affect their properties. However, disks at z∼2 have a size that is 20% smaller than today.

Bulges in the same mass regime ($M_{*,b} > 2 * 10^{10} M_{\odot}$) have also similar sizes, independently of the bulge-to-total ratio. It suggests a unique formation process for massive bulges and also that disk survival/regrowth is a common phenomena after bulge formation (30% of massive bulges live in disk dominated systems). I found however that pure bulges (B/T>0.8) are 30% larger than bulges embedded in disks at fixed stellar mass and have larger Sérsic indices. This is can be explained by a later growth of these systems through minor mergers.

The last part of the thesis focuses on the relation between morphological transformations and quenching. I found that most of the disky galaxies (B/T <0.2) are in the main sequence, while the majority of the bulge dominated systems (B/T >0.8) lie in the quiescent region. This result does not discard the existence of passive disks but suggests that a possible quenching channel without the bulge growth is not common at least in the general field

[1] lerma.obspm.fr/huertas/form_CANDELS

environment probed by our data. Moreover it shows that pure "blue" bulges exist, as already seen in previous works, suggesting that the formation of bulges happens while galaxies are still star forming.

Between these two extreme cases there is a population of galaxies with $0.2 < B/T < 0.8$. They are systems that are both quenched and star-forming with similar abundances. For that reason they are the optimal sample to probe how quenching is acting within galaxies. At fixed stellar mass, bulges in star-forming galaxies are found to be $\sim$ 20-30% larger than bulges in quenched systems. Regarding the disks no systematic difference is measured. This result can be interpreted as a signature that galaxies experience an additional morphological transformation during or after quenching, but such eventual structural changes are confined into the bulge since no significant difference in size is measured for disks hosted in star-forming and quiescent systems. However, the effect of the progenitor bias cannot be discarded. Bulges in quiescent galaxies appear more compact because the measurement is affected by the new quenched galaxies that are more compact only because they quenched recently.

In order to get more insight into the different possibilities and with the aim to put constraints on the formation timescale of bulges and disks, I analyzed the distributions of the UVJ rest-frame colors. This is the first attempt to analyze resolved UVJ colors at these redshifts. I found that almost all galaxies in our sample present negative color gradients. Disks are blue in star forming galaxies and red in quiescent systems , as expected. Interestingly, bulges are always redder than the disk, although their positions in the UVJ plane is closer to the dusty region than the one of pure passive systems. This is compatible with a scenario of inside-out quenching put forward by previous works. However, rejuvenation through disk accretion could lead to similar signatures. Discern between the two possible processes require the knowledge of typical ages of bulges and disks. For that reason I extended the analysis including narrow band imaging (SHARDS).

6.1 On going work

6.1.1 Improving the SED analysis adding the SHARDS data

The knowledge of typical ages of bulges and disk allows to put constraints on their formation timescale. However this step requires a well resolved SED and thus an optimal wavelength coverage. For that reason I extended the analysis to the SHARDS survey, a deep NB imaging survey (25 filters that cover the spectral range of 500-950 nm) of the GOODS-N field. In this section I will introduce before the SHARDS survey. I will then explain the method that is followed to combine the HST models with the SHARDS data. Finally I will show some preliminary results.

6.1.2 SHARDS survey

The Survey for High-z Absorption Red and Dead Sources (SHARDS,Pérez-González et al., 2013), is an ESO large program that consists in an ultra deep spectro-photometric survey. It is carried out with the OSIRIS instrument on the 10.4 m Gran Telescopio Canarias (GTC). It covers the entire GOODS-North field, down to 26.5 AB mag. It covers the spectral range between [500-950] nm with 25 medium-band filters (FWHM-17 nm), and spectral resolution of R$\sim$50. The main aim of this project is to build a sample of quiescent early type galaxies at $z > 1$. Following that purpose, this survey was designed to measure the rest frame UV spectra of galaxies at $z > 1$, in order to detect the Mg absorption line, necessary and sufficient sign to detect massive and quiescent ETGs at high redshift.

6.1.3 Method

As largely explained in the previous chapter, the bulge-to-disk decomposition of the light profile requires high signal-to-noise ratio and an optimal resolution. For that reason in the previous analysis we decided to use the HST/CANDELS data applying the multi bands fit. SHARDS is a ground based survey, thus its resolution does not allow to apply directly the multiple fitting. To fix this issue I used the HST models, rescaled to the SHARDS resolution, as a constraints to model the light profile on this set of data. Thanks to knowledge of the Chebyshev polynomial coefficients, it is possible to trace the wavelength dependence of each quantities and extract the corresponding values for the SHARDS filters wavelength. It can be done, since all the SHARDS bands are within the HST wavelength coverage. The polynomial

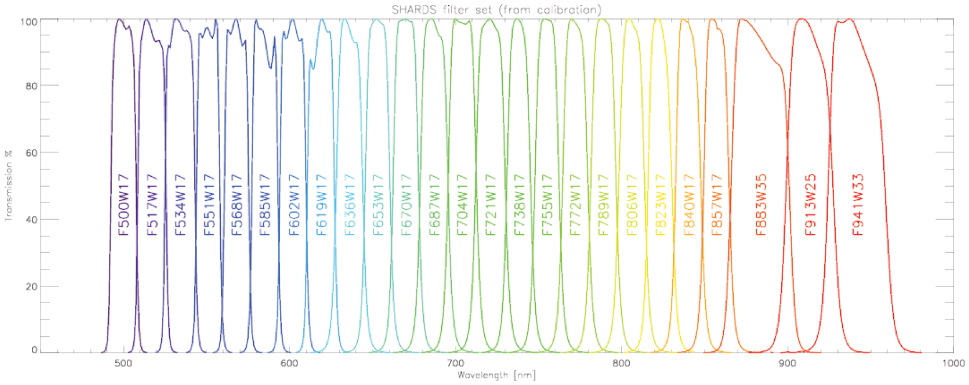

Figure 6.1: Transmission curves for SHARDS filter set (individually normalized)

functions are not trustable outside the range of the data since they are not constrained. Once all the needed values are interpolated, they are used to model the Sérsic profile for single/double component with Galapagos-2. Regarding the choice of the degree of freedom, theoretically, the same setup as for the HST data can be applied. Therefore, while it works properly for the single model fit, it could introduce a bias in the resulting models for the double profile fitting. Indeed, giving to many degree of freedom to the functions, in that case, will bring the algorithm to not be able to separate properly the two components, due to the background noise and the low resolution. For that reason all the parameters are fixed to the interpolated values, except the magnitudes. The final step is then the SED fitting, using HST+SHARDS filters, to estimate the stellar parameters.

6.1.4 Preliminary results

As a proof of concept, the "combined" bulge-to-disk decomposition was applied on a sample of galaxies classified as double component systems by the CNN algorithm. The resulting models, obtained by combining the SHARDS and HST data are compatible with the one recovered with HST alone. Even though the method need to be optimized, as it will be discussed in the next section, since already a small shift in flux between the two dataset does not allow to obtain a reliable SED.

Figure: 6.2 shows an example of the accuracy that can be reached from the bulge-to-disk decomposition done using together the HST and the SHARDS data. The single Sérsic model is quite well recovered. The results are in good agreement. It means that the interpolation and the following adaptation

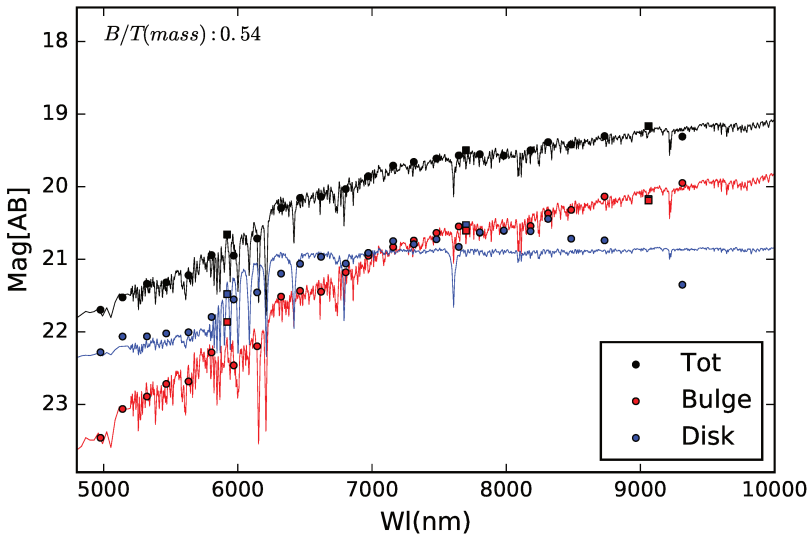

Figure 6.2: Example of the SED analysis done combining the HST and the SHARDS data. The black line represents the total magnitude/flux, while the red and the blue ones are respectively the bulge and the disk component. Points are magnitudes from the Sérsic model.

of the HST models to the SHARDS resolutions are well implemented. The bulge and the disk magnitudes are also compatible in the range of wavelength covered by both dataset.

Table 6.1 shows an example of the output of the SED analysis done with HST+SHARDS data. This analysis reveals that the disk is young and star forming while the bulge component is older with low value of on going star formation activity. These results are still preliminary and need to be carefully tested.

HST+SHARDS	ltau	t [Gyr]	lmass	Av	lsfr	chi2
Bulge	7.90	1.9	10.94	0.7	-6.21	0.4
Disk	8.30	1.38	10.86	0.2	0.25	0.2

Table 6.1: Results from the SED fitting on bulge and disk obtained from the combined decomposition.

Problems of the method and possible solutions

Figure 6.3 shows the resulting magnitude profile for a representative sample of galaxies. The SHARDS profiles, for many objects, are in quite well agree-

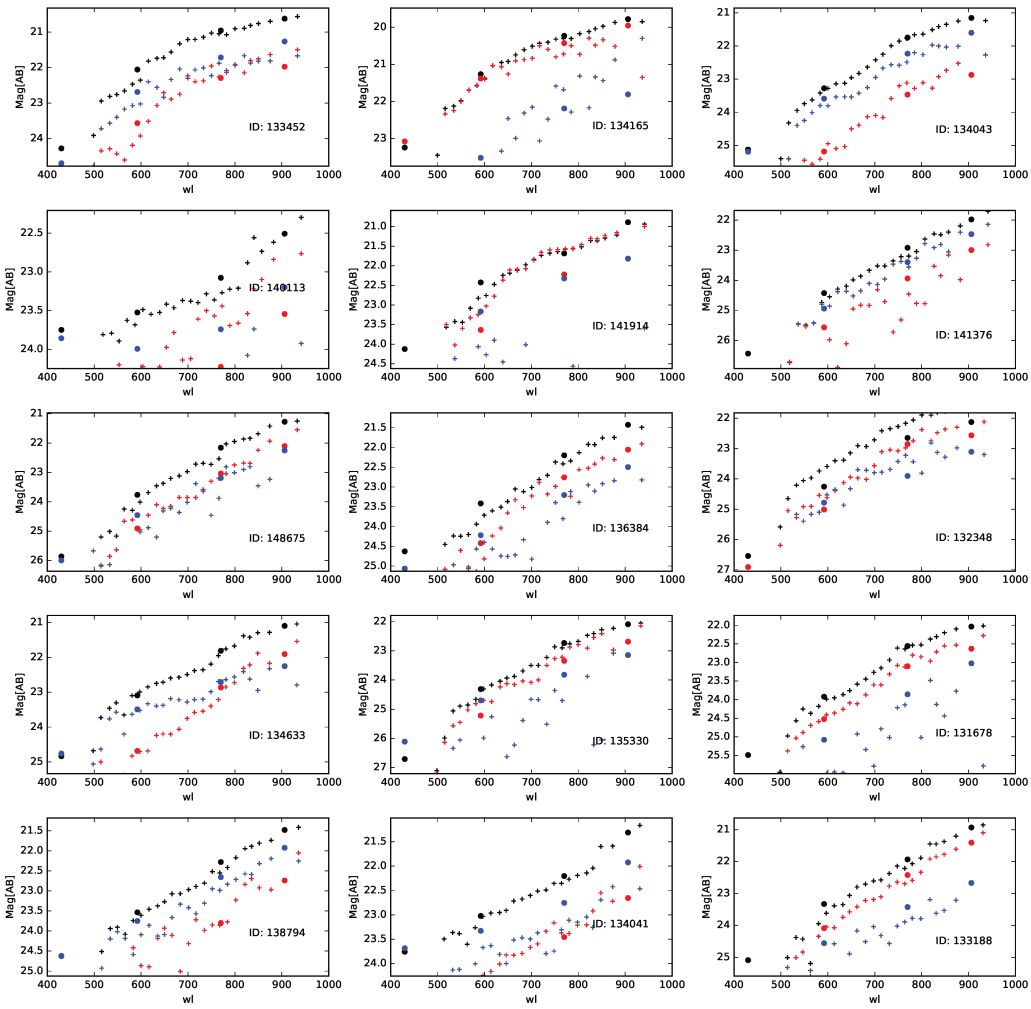

Figure 6.3: Examples of bulge-to-disk decomposition combining the HST models with the SHARDS data. Blue points are the total magnitudes, red and green are respectively bulges and disks magnitudes.

ment with the HST data. Thanks to the large number of filters covering a tight range of frequencies, it is possible to follow the fluctuations of the flux and to observe some emission/absorption lines. Although this is verified for most of single model profile, there are many cases in which the bulge-disk decomposition fails and the final magnitudes are shifted respect to the HST data. The difference can be due to the high number of the degrees of freedom given to the magnitude function, since in this test I left them totally free. The solution has to be find in an optimal adjustment between the degrees of freedom and the range of values in which the polynomials can vary. The reduction of the order of the function constraints the wavelength dependence of the magnitudes since the single value are going to be correlated each other. On the other side restrict the range of values in which the magnitude spans can avoid the degeneration of the fit due to the low resolution. The default setting of GALFITM allows the single band magnitude to vary in a range of $^{+}_{-}5$ magnitudes from the input value. While this weak constriction has reasonable meaning in a normal fit, in this case, since the input values are already the result of a best fit model, it can lead space to contamination. More tests need to be done in order to explore the effects of these changes on the final output.

6.2 Future project

Classical bulges vs pseudo-bulges

Simulations and observations agree in the existence of two populations of bulges : classical and pseudo bulge. Reviewing the state-of-the-art in the literature related with this topic reveals that classical and pseudo-bulges show different properties and thus follow different scaling relations due to different formation process (Gadotti, 2009, Kormendy & Fisher, 2008). Most of the works already done are applied in the local universe. The present catalog allows to extend this analysis at larger redshift. Along the entire analysis presented in this work I did not consider galaxies classified as pseudo-bulges. This classification is telling us that the light profile of the central part of those galaxies is well described by a Sérsic model with $n<2$. This is the reference model for which the selection algorithm was trained on. Indeed bulges can appears with an apparent shape as a pseudo bulges due to a combination of the projected angle and the axis ratio. A step forward is then to apply a selection that take into account of these possible contaminations, to build a cleaned sample of pseudo bulges. The study of scaling relations as well as compare their properties with the classical bulges can allow to put

constraint on the different formational processes. Are pseudo-bulges younger than the classical one? how the central bar affect the building of the central density? Various works proposed a possible rejuvenation process of bulges in barred galaxies. (Gadotti & Coelho, 2015). Proper answer to these questions require to explore typical colors and ages. Moreover the addition of a third profile is a path to test this theory, as it is already done in the local universe (Salo et al., 2015, Gadotti, 2010, Vera et al., 2016, Nair & Abraham, 2010). The multi-wavelength approach will allow to estimate the stellar population properties that it is a quite new and not common topic.

Environmental quenching?

The evolution of galaxies is guided by internal processes, related to the galaxy itself like AGN activity or supernova feedback, as well as gravitational interactions that results in major/minor mergers. In addition to that, the environment where they reside into has to be taken into account to have a complete scenario. Dense environments like clusters or group, are believed to accelerate the evolution producing more massive galaxies, as well as to modify their morphology. This field is largely explored in the literature with discordant results. No relevant difference is measured in the mass-size relation of massive elliptical galaxies in the local universe (Maltby et al., 2010, Huertas-Company et al., 2013b), while several authors claim that they show larger sizes when they belong to groups or clusters at high redshift (**?**Delaye et al., 2014). Moreover spirals with extended stellar discs are not present in cluster. It suggests that this component cannot survive in the environmental conditions present in dense region. (Maltby et al., 2010, Cebrián & Trujillo, 2014, Kuchner et al., 2017) Galaxy harassment, ram pressure stripping, tidal force etc, are all mechanisms that are acting to remove or trigger the consumption of the gas content. Since the gas is less bounded in the outskirt than in the central region, all these processes are going to affect first the external region causing the fading of the disk. This is reflected in the mass size relation this component as shown by Kuchner et al. [2017]. The present catalog allow to explore how the morphology differ between dense and less dense environment as well as to better quantify the effects of the the environmental quenching on the disk component.

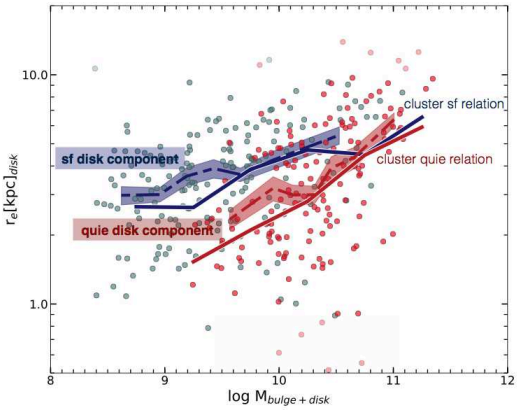

Figure 6.4: The distribution of sizes of the disk component for 3 σ clipped data of star-forming (blue) and quiescent (red) galaxies. The overall trends suggest that disk components in quiescent galaxies are smaller than in star-forming galaxies. For reference we also include the whole-galaxy (single component) effective radii relation.Faint points represent galaxies excluded by the clipping routine (Kuchner et al., 2017).

Chapter 7

Appendix

7.1 Paper: A catalog of polychromatic bulge-disc decompositions of $\sim$ 17.000 galaxies in CANDELS

MNRAS **000**, 1–?? (2017) Preprint 13 November 2017 Compiled using MNRAS LATEX style file v3.0

A catalog of polychromatic bulge-disc decompositions of ~ 17.000 galaxies in CANDELS

Paola Dimauro[1],★ Marc Huertas-Company[1,2,3], Emanuele Daddi[4], Pablo G. Pérez-González[4], Mariangela Bernardi[2], Guillermo Barro[6], Fernando Buitrago[7], Fernando Caro[1,3,9], Andrea Cattaneo[8], Helena Dominguez-Sánchez[1], Sandra M. Faber[9], Boris Häußler[10], Dale D. Kocevski[11], Anton M. Koekemoer[12], David C. Koo[9], Simona Mei[1,3], Joel Primack[8], Aldo Rodriguez-Puebla[13], Mara Salvato[14], Francesco Shankar[15], Diego Tuccillo[1]

[1] *LERMA, Observatoire de Paris, CNRS, PSL, Université Pierre et Marie Curie, 61 Avenue de l'Observatoire, 75014, Paris, France*
[2] *Department of Physics and Astronomy, University of Pennsylvania, Philadelphia, PA 19104, USA*
[3] *Université Paris Diderot, 5 Rue Thomas Mann, 75013, France*
[4] *CEA Saclay, Laboratoire AIM-CNRS-Université Paris Diderot, Irfu/SAp, Orme des Merisiers, 91191, Gif-sur-Yvette, France*
[5] *Departamento de Astrofísica, Facultad de CC. Físicas, Universidad Complutense de Madrid, E-28040 Madrid, Spain*
[6] *University of California, Berkeley, CA 94720, USA 0000-0001-6813-875X*
[7] *Instituto de Astrofisica e Ciencias do Espaco, Universidade de Lisboa, OAL, Tapada da Ajuda, P-1349-018 Lisbon, Portugal*
[8] *GEPI, Observatoire de Paris, 61 Avenue de l'Observatoire, 75014, Paris, France*
[9] *University of California, Santa Cruz, CA 95064, USA*
[10] *European Southern Observatory, Alonso de Cordova 3107, Vitacura, Casilla 19001, Santiago, Chile*
[11] *Department of Physics and Astronomy, Colby College, Waterville, ME 04961, USA*
[12] *Space Telescope Science Institute, 3700 San Martin Drive, Baltimore, MD 21218, USA*
[13] *Instituto de Astronomía, Universidad Nacional Autónoma de México, A.P. 70-264, 04510 México, D.F., Mexico*
[14] *Max Planck Institut fur Plasma Physik and Excellence Cluster, 85748 Garching, Germany*
[15] *Department of Physics and Astronomy, University of Southampton, Highfield, SO17 1BJ, UK*

Accepted XXX. Received YYY; in original form ZZZ

ABSTRACT

Understanding how bulges grow in galaxies is of capital importance to unveil the link between galaxy morphology and star-formation. To that purpose, obtaining accurate decompositions into their main components (bulges and disks) of large samples of galaxies at different cosmic epochs is required. This is particularly challenging, especially at high redshifts, where galaxies are poorly resolved. This work presents a catalog of bulge-disc decompositions of the surface brightness profiles of ~ 17.600 H-band selected galaxies in the CANDELS fields ($F160W < 23, 0 < z < 2$) in 4 to 7 filters covering a spectral range of $430 - 1600nm$. This is the largest available catalog of this kind at $z > 0.2$. By using a novel approach based on deep-learning to select the best model to fit, we manage to control systematics arising from wrong model selection and obtain less contaminated samples than previous works. We show that the derived structural properties are within $\sim 10 - 20\%$ random uncertainties. We then fit stellar population models to the decomposed SEDs of bulges and disks and derive stellar masses (and stellar mass bulge-to-total ratios) as well as rest-frame colors (U,V,J) for bulges and disks separately. All data products are publicly released with this paper.

Key words: galaxies: fundamental parameters, galaxies: high-redshift, galaxies: bulges

1 INTRODUCTION

Galaxies are essentially formed by two major components, disks and bulges, which formation mechanisms are believed

★ E-mail: paola.dimauro@obspm.fr

to be very different. Disks are generally rotationally supported and confined into a thin plane. They are believed to be the consequence of gas infall into halos, which transfer their angular momentum to the baryons. Bulges have generally a 3D shape and larger velocity dispersions of the stars. Their formation requires dissipative process and a loss of angular momentum. Mergers of two disks is the classical channel to grow bulges (e.g.Toomre 1977). However numerical models show that disks, especially at high redshift when they are more unstable and gas rich, can also self generate a bulge through instabilities (e.g. Bournaud 2016) and/or inflow of cold gas towards the center (e.g. Zolotov et al. 2015). Properly understanding how all these different processes come together to assemble galaxies into their main components, requires identifying bulges and disks in galaxies and studying their evolution across cosmic time. Since disks and bulges have different projected surface brightness distributions, the decomposition of the light by fitting analytic Sersic models (Sersic 1968) to the 1D or 2D light profiles has been widely used in the literature. Extending this approach to large datasets arising from deep-surveys, where objects cannot be checked on an individual basis, is particularly challenging. Not only because of the computing time but also because the amount of systematics that need to be controlled. At low redshift, where galaxies are reasonably well resolved, two works have obtained bulge-disc decompositions on several hundreds of thousands of galaxies in the SDSS (Simard et al. 2011; Meert et al. 2015). A significant amount of post processing is required anyway to assess the quality of the fits and eventually identify unphysical solutions. One key issue for instance is deciding wether two components are really needed to model the light profile or if one unique component is better suited. This is usually addressed by performing a-posteriori statistical tests to measure if the addition of an extra component improves the fit (e.g. Meert et al. 2015).

At high redshift, the situation is even more dramatic both because of lower S/N and because galaxies start to be less well resolved even with space based imaging. That is why, most of the works involving surface brightness fitting of large samples of distant galaxies tend to use one single Sersic component and reduce that way the amount of free parameters (e.g. Häussler et al. 2007; van der Wel et al. 2012). Two component fitting is generally done on smaller datasets (e.g. Bruce et al. 2014a). Even there, degeneracies are reduced by adding more contraints on the parameters. For example, Bruce et al. (2014a) forced the Sersic index of the bulge to be 4. Many works have shown however that bulges have a wider distribution of the Sersic index (e.g Meert et al. 2015) so this might not be the ideal solution.

An additional issue of bulge-disc decompositions is that they are performed on the light profiles. Models predict however stellar mass distributions. Deriving stellar masses from light distributions, however, requires requires assuming a M/L ratio, which can be different for bulges and disks and also from galaxy to galaxy. Assuming that the light traces equally the mass in stars (a unique M/L for all galaxies/components) is clearly an oversimplification which can introduce additional systematics. This is especially true for high redshift studies, where very different cosmic epochs are probed.

In this paper we present a catalog of bulge-disc decompositions of ~ 17.000 galaxies in the CANDELS fields. This is the largest catalog of this kind for objects at $z > 0.2$. Besides of the size, this work introduces several novelties as referred to previous works to improve some of the issues discussed above. First, we develop a method based on deep-learning to estimate the optimal model that should be used to fit the light profile (namely one or two components). As opposed to other techniques existing in the literature which work on the fitting residuals, our method acts before the fitting, at the pixel level. Additionally, our fits are done simultaneously in 4 to 7 (depending on the fields) high resolution filters using the modified version of GALFIT, GALFITM (Häussler et al. 2013; Vika et al 2014). This allows us to increase the S/N and reduce the random uncertainties but also to estimate Spectral Energy Distributions (SEDs) of bulges and disks and a M/L for every component by fitting stellar populations models with the FAST code (Kriek et al 2009). We thus provide stellar population properties (stellar masses, SFRs) and rest-frame colors (U,V,J) for bulges and disks. This should enable a less biased comparison with predictions of galaxy formation models. The catalog is made public with the present paper[1].

The paper proceeds as follows. We describe the dataset in section 2. The methodology used for profile fitting is discussed in sections 3 and sections 4. The accuracy of the catalog is quantified in section 5. The stellar population properties are described in section 6. All magnitudes are measured in the AB system.

2 DATA

Our starting point for the selection are the official CANDELS (Grogin et al. 2011; Koekemoer et al. 2011) H-band (F160W) selected catalogs (Galametz et al 2013 for UDS, Guo et al 2013 for GOODS-S, Barro et al. (2017) for GOODS-N and Stefanon et al. 2017 for COSMOS and AEGIS). For this study, we only consider galaxies brighter than $F_{160W} = 23$. This magnitude selection is applied to ensure reliable two component decompositions as detailed in section 5. In addition to the three NIR images (F105, F125, F160), observed as part of the CANDELS survey, we use ancillary data in four additional bands for GOODS-N and GOODS-S (F435W, F606W, F775W, F850L) and two in the AEGIS, UDS and COSMOS fields (F606W, F814W). All images are resampled to a common pixel scale of 0.06 $arsec/pixel$. This is required to perform simultaneous multi-wavelength fits to the surface brightness profiles as described in section 4.

We also use in this work the 2D single Sersic fits published in van der Wel et al. (2012) in three NIR filters (F105W, F125W, F160W) and the deep-learning based *visual* morphologies published in Huertas-Company et al. (2015). The official CANDELS redshifts are used. More details can be found in Dahlen et al. (2013). Spectroscopic redshifts are used when available. If not, we use photometric redshifts derived through SED fitting by combining different available codes. Although we derive stellar masses of bulges of disks (described in section 6) we also use total

[1] lerma.obspm.fr/ huertas/CANDELS

z	All	Q	SF	Bulge	Disk
0-0.5	9.0	9.16	8.98	8.47	8.29
0.5-1.0	9.75	9.91	9.79	9.22	9.10
1.0-1.4	10.3	10.38	10.28	9.69	9.59
1.4-2.0	10.7	10.72	10.69	10.03	10

Table 1. Stellar mass completeness of the sample used in this work. We show the values for all galaxies, quiescent (Q), star-forming (SF) and also for the embedded bulges and disks components.

stellar masses from previous works for comparison (Huertas-Company et al. 2016). Namely, the best available redshift is used to estimate stellar masses based on the PEGASE01 stellar population models (Fioc & Rocca-Volmerange 1999). We assume solar metallicity, exponentially declining star formation histories, Salpeter (1995) IMF and a Calzetti et al. (2000) extinction law. The M_*/L ratios are converted to a Chabrier (2000) IMF by applying a constant 0.22 dex offset. Rest-frame magnitudes (U,V,J) are also derived as part of the SED fitting procedure and are used to divide galaxies between star-forming and quiescent systems with the now standard way (see Whitaker et al. 2012).

Our final sample consists of $\sim$ 17.600 galaxies out of $\sim$ 19.000 with $F160W < 23$ in the CANDELS survey. The difference comes from the fact that there is not a perfect overlap between the fields in the different filters. We restricted our analysis to galaxies observed with at least 4 filters. Figure 1 shows the distribution of the selected galaxies in the $M_* - z$ plane. We estimate the stellar mass completeness using the method described in Pozzetti et al. (2010). The lower limit stellar mass (M^*_{lim}) is computed as: $log(M^*_{lim}) = log(M_*) + 0.4 \times (m_{f160W} - 23)$, where m_{f160W} is the apparent magnitude in the $F160W$ filter where the selection is done. The completeness is then estimated as the 90th percentile of the distribution of M^*_{lim}. We repeat the same procedure for all galaxies as well as for passive and star-forming galaxies (selected according to their UVJ colors). The obtained values are indicated in figure 1 and also tabulated in table 1. We estimate a mass completeness limit of $\sim$ 10.7 at $z \sim 2$. We notice that for the passive population, very few galaxies lie below the completeness limit, despite the bright magnitude cut. This is expected given the evolution of the stellar mass function of passive galaxies (e.g. Ilbert et al. 2013), which at $z > 1.5$, is dominated by massive galaxies. As a sanity check, since the CANDELS catalogs are several magnitudes deeper than our selected catalog, the stellar mass completeness is also estimated by computing the stellar mass above which at least 80% of galaxies from the deep catalog at a given mass and redshift are selected (see also Huertas-Company et al. 2016), obtaining similar results. We also provide in table 1 an estimate of the completeness for embedded components (bulges and disks). For bulges (disks) we simply multiply the stellar mass completeness of passive (star-forming) galaxies by 0.2, since we estimate (see section 5.3) that we can reliably measure the magnitude of the bulge (disk) component down to $B/T \sim 0.2$ (0.8).

The key measurement added by this work is a one/two

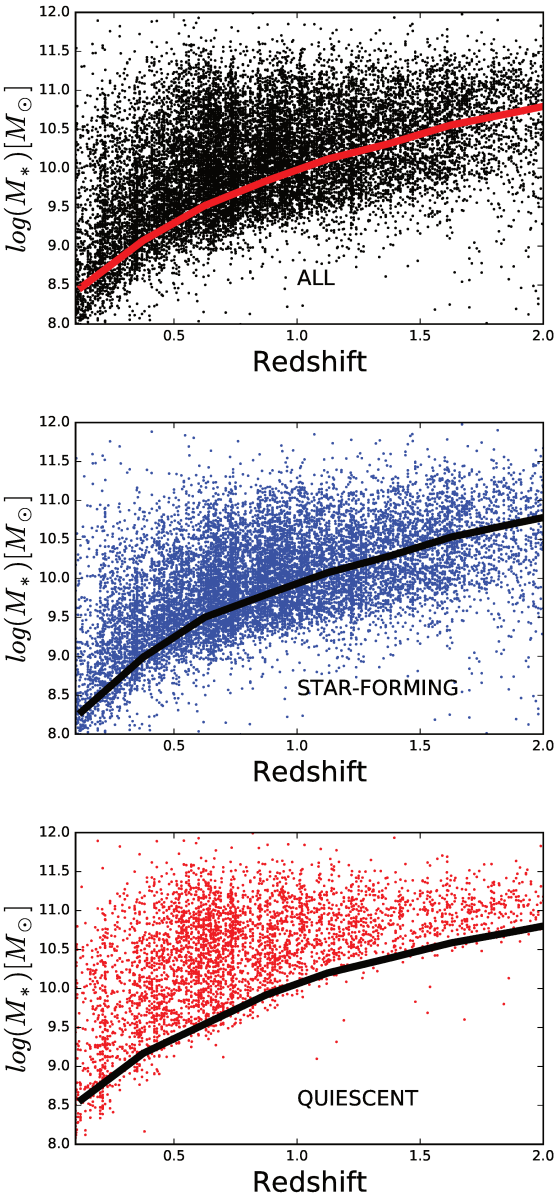

Figure 1. Stellar mass completeness of the selected sample.The panels show the relation between redshift and stellar mass for galaxies in our sample ($F160W < 23$). Top: all galaxies, middle: star-forming, bottom: quiescent. The shaded regions indicate the stellar mass completeness estimated using the method described in the text.

component (bulge/disk) decomposition of the surface brightness profiles in different filters. In the following we describe the details of the methodology as well as the procedure used to estimate the uncertainties.

3 BEST-MODEL SELECTION WITH DEEP-LEARNING

A fundamental problem with surface brightness profile fitting is to decide how many components are needed to model the galaxy light. By using two component models, we force the fitting algorithm to find a solution with 2 components

within a given set of constraints even if the galaxy might be better fitted with one single Sersic profile or another combination of profiles. This can lead to unphysical solutions, introducing a systematic error in our subsequent analysis of bulges and disks properties. The reason is that some light might be associated with a bulge and/or a disk even if there is not such a component in the galaxy. This systematic uncertainty can potentially dominate over random uncertainties when performing a scientific analysis (e.g. Meert et al. 2015).

Several works have used a statistical approach to tackle this problem. By looking at the residuals of the resulting fits it is possible to establish a probability that adding a profile actually improves the fit (e.g. Simard et al. 2011; Meert et al. 2015). This is sometimes combined with a visual inspection (Margalef-Bentabol et al. 2016). This approach still has the problem that a better fit does not necessarily mean a physically meaningful result and that the light is actually properly associated to bulges and disks.

Here we introduce a novel alternative technique based on unsupervised feature learning (deep-learning). The main novelty is that the best model to fit a galaxy is set a-priori, instead of by looking at the residuals maps a-posteriori. The objective is then to measure, given a galaxy image, which analytic model, among a finite set of possibilities is preferred to describe the surface brightness distribution. Recall that this is different from a morphological classification. We are not aiming at obtaining the *true* morphology but to assess if a given analytical model is appropriate to describe the galaxy.

We proceed in two main steps described in the following.

3.1 Training on simulated analytic galaxies

We first simulate a set of 100.000 synthetic galaxies reasonably spanning all the range of structural parameters expected using the GalSim code[2]. Images are convolved with a real PSF and realistic noise from CANDELS images is added as explained in section 5.2. For this particular application, we only simulate one filter (F160W) that will be used to define the model to be fitted. The H-band filter is chosen as a reference since it is the detection band and also the deepest.

We then define 4 types of profiles among the simulated galaxies:

- Pure Sersic: $B/T > 0.8$ and $n_{bulge} > 2.5$. These are galaxies for which the surface brightness profile should be well described with a Single Sersic model.
- Pure Exponential: $B/T < 0.2$ or ($B/T > 0.8$ and $0.5 < n_{bulge} < 1.5$): Objects for which the surface brightness profile is well captured with a single exponential profile or a one component Sersic profile with a very low Sersic index.
- Bulge + Exponential: $0.2 < B/T < 0.8$ and $n_{bulge} > 2.5$: Systems that clearly require two components, one with an exponential profile and another with a large Sersic index.
- Pseudo-bulge + Exponential: $B/T > 0.2$ and $B/T < 0.8$ and $n_{bulge} < 2$: Systems that still require two Sersic components, but both with low values of the Sersic index.

[2] http://galsim-developers.github.io/GalSim/index.html

For each class of profile, we train an independent Convolutional Neural Network (CNN) in a binary classification mode to isolate the given profile from the others in the simulated galaxies. An introduction to CNNs is out of the scope of this work. For more information, we refer the reader to Dominguez-Sanchez et al. (2017) and Tuccillo et al. (2017) where more details are given. In this work we train 4 different machines with the same architecture. The input of the network is a simulated 2D image (with noise and PSF) centered on the galaxy (64×64 pixels) and the output is a probability that the image is described by the model it was trained to identify. The model has 4 convolutional layers of increasing depth (from 16 to 64) and 2 fully connected layers. A 3×3 max pooling is performed after each convolutional layer to reduce the number of parameters and a 10% dropout is applied during training to avoid over-fitting. Additionally, a 1% gaussian noise is added in the first layer to avoid that the network learns features on the noise pattern. The model configuration was established after testing different architectures. Slight modifications do not change the main results. The model is trained until convergence and evaluated on the validation dataset.

At the end of the training process, each simulated galaxy has 4 associated probabilities. Recall that the probabilities do not add to 1 since they were estimated with four independent CNNs. Since for the simulated galaxies, we know the model that was generated, we can quantify the ability of the CNN to distinguish between different profiles on an independent test dataset which was not used during the training phase. Following a standard procedure, we use the area under the ROC curve as main indicator, quantified by two parameters: Specificity (P) and Sensitivity (C):

$$C = \frac{TP}{TP + FN}$$

$$P = \frac{TN}{TN + FP}$$

TP, FP stand for true and false positives respectively, TN, FN are true and false negatives. Specificity is therefore a measurement of how contaminated a selection of a given class is by galaxies not belonging to that class. Sensitivity is a measurement of how good the machine recovers all galaxies belonging to a given class. In figure 2 we show how these two quantities change depending on the applied probability threshold. As expected, the larger the probability, the purer the sample is but also less complete. The plots confirm that the CNN models are able to distinguish between the 4 different types of profiles. We notice that a probability threshold of $p = 0.4$ results in a reasonable trade-off between purity and completeness, around 80% – 90%.

3.2 Knowledge transfer to real galaxies

The above results are based on simulations. The critical step is to use the 4 machines to classify our real galaxies. Our aim is to provide, for each object, a probability that a given model (i.e. pure bulge, pure disk, bulge+exponential, pseudo-bulge+exponential) is preferred to describe its surface brightness profile. We insist that this is not a morphological classification and it is fundamentally different

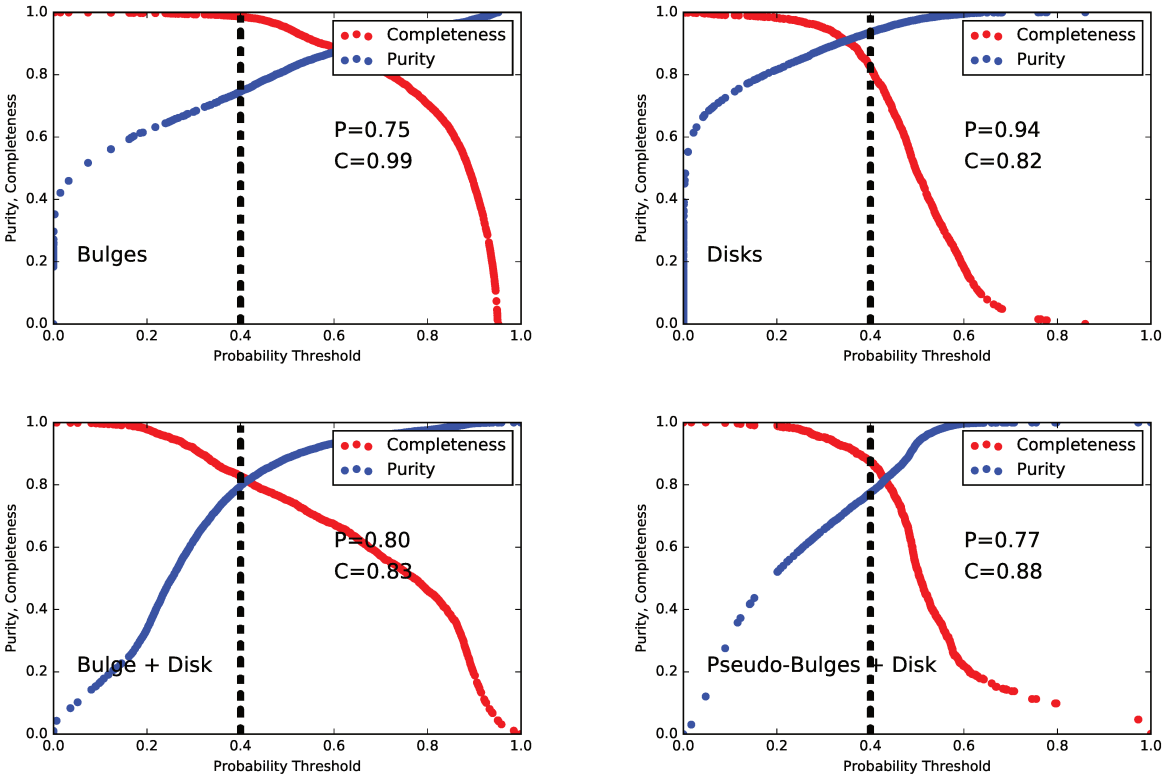

Figure 2. Purity and completeness as a function of the probability threshold for the 4 types of models considered in this work. The labels in each plot show the values for the adopted threshold of P=0.4 (black dashed line).

than the visual morphological catalog presented in Huertas-Company et al. (2015). It measures, given a set of available analytic profiles, which one is better suited to fit the surface brightness distribution of a given galaxy. This information is intended to be used as input for fitting the light profiles as explained in the following sections.

In transferring the trained machine to real data, there is a risk that the CNN does not provide reliable results since simulations and real galaxies are obviously different. For example, even though our simulations include realistic instrumental effects and noise, we did not include close companions in the training set nor irregular galaxies or bars. The validity of the knowledge transfer between simulations and real data is difficult to evaluate since, as opposed to the simulations, the *true* profile is not known in the real sample

In order to verify that the trained model properly represents reality, the only alternative is to perform some posterior sanity checks.

- First, we visually inspect a significant number of color images of different classes provided by the CNN. Although, this is not a quantitative measurement, it allows to identify obvious errors. Examples of the galaxies classified according the different types of profiles are shown in figure 3. Generally speaking, when the algorithm measures that 2 components are required, a bulge and a disk are appreciated in the color image.
- In terms of types of models, we find that for the majority of the galaxies ($\sim$ 55%) a bulge+exponential model is preferred. Then, $\sim$ 20% of galaxies are well fitted with an exponential model, $\sim$ 15% are preferentially fitted with 2 low Sersic index components and $\sim$ 10% are well described with one Sersic profile with $n > 2$. This is also in rather good agreement with the expectations. The majority of galaxies are described by a *classical* two component model with a central bulge with large Sersic index and an exponential disk. However, it is worth noticing that if no model pre-selection is done and a 2 component fit is blindly applied to all the sample, the systematic error reaches $\sim$ 50% and thus most probably dominates the error budget.
- Then we measure that $<$ 10% of the galaxies in the real sample have all 4 probabilities below $P = 0.4$, i.e. their surface brightness profile is not properly described by any of the 4 considered models. All other galaxies have at least one of the probabilities above this threshold. This is good indication that the network did not find drastic differences between the training/test simulated samples and the real data. Otherwise the probability distributions would have been very low for all real galaxies.
- Regarding, those galaxies for which no model is preferred ($P < 0.4$), the visual classification taken from Huertas-Company et al. (2015) indicates that the vast majority of them ($> 80\%$) are classified as irregulars with high probability (see also figure 3). It is expected that their surface brightness profile is not properly described by any of the considered models. We notice additionally that for the irregulars for which a best profile was actually found a *pure* disk like profile is the most preferred solution.

Following this methodology, each galaxy in the catalog

has associated four probabilities which measure how accurate a given profile to fit its light distribution is. This allows to select a model to fit a-priori and that way reduce systematic uncertainties as described in section 5.

4 MULTI-λ FITS WITH GALFITM

The main tools we used to perform the fits are GALFITM and GALAPAGOS-2 from the MEGAMORPH project (Häussler et al. 2013; Vika et al 2014). They are based on GALAPAGOS and GALFIT (Barden 2012; Peng et al. 2002). The main difference it that they allow to simultaneously fit all images at different wavelengths (as opposed to an independent fit for each band). As shown in the aforementioned works, the advantage of such an approach is that, by combining data from all filters, we effectively increase the S/N and naturally use the color information. Therefore the fit is better constrained down to fainter magnitudes than when considering all bands independently. In order to do so, the wavelength dependence of the structural parameters of galaxies is parametrized with a family of Chebyshev polynomials. The order of the polynomial for each quantity is a user-configurable parameter which sets the degree of freedom. The fitting algorithm then minimizes the coefficients of the function for each structural parameter. If the degree of freedom is equal to the number of filters, then the parameter is effectively independent in each band. It is obviously the case for the fluxes. For the other parameters, the choice (of the degrees of freedom allowed) is a trade-off between allowing total independence or setting no variation with wavelength (thus reducing the number of free parameters). More details can be found in Häussler et al. (2013); Vika et al (2014).

There is no obvious way of selecting the optimal configuration. The wavelength dependence of the structural parameters will certainly vary from galaxy to galaxy. Our approach has been to empirically test different configurations and use them to estimate random uncertainties as discussed in section 5. For each galaxy we fit 2 types of models: a 1 component Sersic model and a 2 component Sersic+Exponential model. Then, for each of the models we adopt three different setups for GALFITM as shown in table 2. In all setups, the fluxes of both components are left free, the centroids of galaxies are set constant over wavelength (we assume that the images were properly aligned). The position angles of the galaxy and the axis ratios are also kept constant since these quantities are not expected to present strong wavelength dependence. The most critical parameters are the Sersic index and the effective radius. We explore the effect of the wavelength dependence of the size by allowing a quadratic variation in the setups 1 and 4 and restricting to constant in the setups 2 and 5. Additionally, the maximum degree of freedom is reduced to the number of bands used in each field. For the Sersic index of the bulge (Sersic+Exponential model) we only allow a linear variation (given that the bulge is normally dominated by old stellar populations, we do not expect a strong wavelength dependence of the Sersic index). However, we changed the range from 0-8 in the setups 4 and 5 to 2.5-8 in setup 6. This is used, as explained in section 5, to evaluate our procedure for model selection based on CNNs (see section 3). The properties of all runs performed are summarized in table 2.

			x	y	mag	r	n	q	pa
Sersic	setup 1		0	0	6	2	1	0	0
	setup 2		0	0	6	0	1	0	0
	setup 3		0	0	6	1	1	0	0
Sersic+Exp	setup 4	BULGE	0	0	6	2	1	0	0
		DISK	0	0	6	2	fix	0	0
	setup 5	BULGE	0	0	6	0	1	0	0
		DISK	0	0	6	0	fix	0	0
	setup 6	BULGE	0	0	6	1	1*	0	0
		DISK	0	0	6	1	fix	0	0

Table 2. Orders of the polynomial functions used in the GALFITM run for each parameter. Each galaxy was fitted with 2 models (Sersic / Sersic + Exp) and three different setups. 0=constant over all wavelengths, 1=linear, 2=quadratic function, 6 =free. The main difference between the setups resides on the degree of freedom allowed in the size wavelength dependence. For setup 3, the Sersic index of the bulge component is only allowed to vary in the range 2.5 – 8.

5 QUANTIFICATION OF UNCERTAINTIES

We quantify in the following, the global accuracy of our final bulge/disk catalog with different approaches.

5.1 Accuracy of model selection

In order to test the validity of our methodology to select the best model, we compare the outputs delivered by GALFITM with the expectations according to the CNN based classes. If both, the best model *class* and the fitting procedure work as expected, one would expect that the best fit model converges towards the expected *best* profile. In figure 5, we show the H-band Sersic index distributions of the bulge component for galaxies classified in the 4 profile classes detailed previously (using a probability threshold of 0.4). For obvious reasons, for objects for which a single Sersic model is preferred, we plot the global Sersic index as well as for pure exponential profiles. Figure 5.1 summarizes the criteria used for the selection. We clearly see that the distributions are different for every type of model and follow the expected trends. Pure disks and pseudo-bulges have almost all Sersic indices lower than 2. Pure bulges, peak at values of $n \sim 3-4$. The distribution for objects that require a 2 component fit extends to large values as well. However, there is a fraction of objects for which our CNN based model selection technique would have preferred a model with a high Sersic index bulge while the fitting procedure converges to a solution with a lower value (dashed orange line in figure 5). Given that we expect a contamination of $\sim$ 15% (see fig. 2), the fraction seems a bit higher than expected. In order to test if this is a problem of GALFIT converging to a local minimum, we use the results of setup 6 (table 2) in which the Sersic index of the bulge was forced to be larger than 2.5 at all wavelengths. For approximately 50% of the objects, the fitting procedure converged to a new solution with n_b exactly equal to 2.5, i.e. the boundary condition. We considered therefore that for these objects a low Sersic index bulge is the best solution. However, for the remaining 50%, the new setup provided a solution with $n_b > 2.5$ in agreement with the CNN classification. The cor-

Figure 3. Color images of galaxies of the 4 types of models, and unclassified. From top to bottom: galaxies for which a pure disk model is fitted, galaxies for which a pure bulge model is preferred, galaxies for which a 2 component model with $n_b > 2.5$ is preferred, objects for which a low Sersic index bulge is the best solution, irregular/unclassified galaxies.

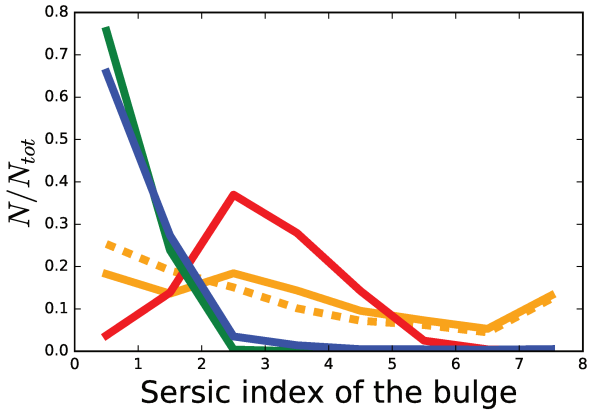

Figure 5. H band bulge Sersic index distribution for the different CNN derived models (see text for details). For bulges (B) and disks (D), the global Sersic index is plotted. For the B+D and PB+D we plot the Sersic index of the bulge component only.

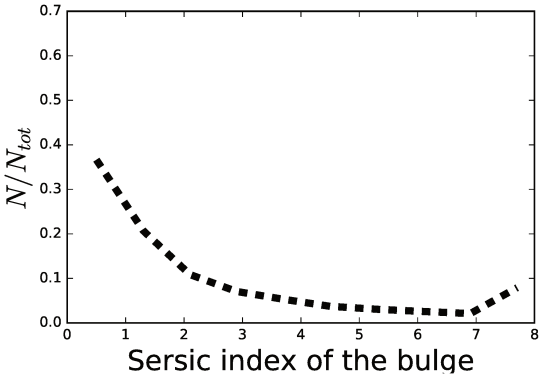

Figure 6. H band bulge Sersic index distribution of all galaxies with no model pre selection. If no model selection is applied, ~ 50% of the bulges have Sersic indices lower than 2.

rected distribution is shown in figure 5. As expected, the number of bulges with $n_b < 2$, has been reduced and is now compatible with the expected contamination level. We notice that, if no model selection is applied, half of the bulges have low Sersic index values (< 2) as shown in figure 6.

In figure 7, we show the distribution of the difference between the sizes of disks and bulges for objects identified as requiring two components. As expected, for the vast majority of the objects, the disk component has a larger effective radius than the bulge. For comparison, we also show the same distribution for objects that were classified as pure disks by the CNN model. In that case, roughly half of the population has a bulge larger than the disk. This confirms that a 2 component model is not suited for these galaxies. Including the bulges of these objects in any scientific analysis would definitely introduce a systematic error that can potentially bias the results.

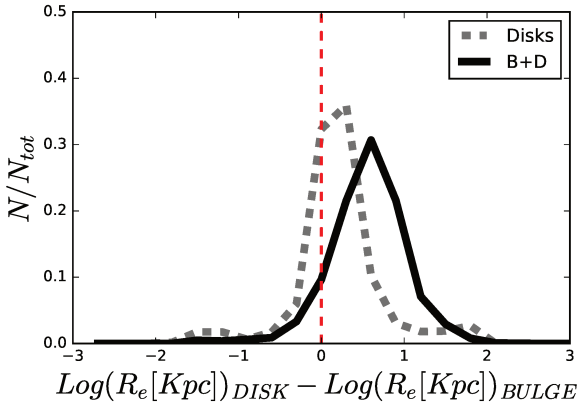

Figure 7. Distribution of the difference between the sizes of disks and bulges for our 2 component systems (black line). The vast majority of the objects have larger disks as expected. The dashed line shows the same distribution for one component disks according to the CNN classification (see text for details). For roughly half of the objects, the fit converges to a solution in which the bulge is larger than the disk. This confirms that 2 component are most probably not needed for these systems.

5.2 Statistic systematic uncertainties with simulations

We use simulations as commonly done in the literature to estimate the global accuracy of the fits. In particular, one key quantity to be calibrated is the limiting magnitude (or S/N) below which measurements remain unbiased. From van der Wel et al. (2012), we know that for galaxies fainter than $F160W = 24.5$ (at the *wide* depth), statistical errors on the structural parameters derived from 1 component Sersic fits exceed ~ 20%. This threshold needs to be calibrated for 2 component fits.

In order to do so, we follow a standard procedure based on simulations of analytic profiles as done in several previous works (e.g. Häussler et al. 2007; van der Wel et al. 2012; Delaye et al. 2014). Namely, we generate mock galaxies with 2 analytic profiles (a Sersic profile for the bulge component and an exponential for the disk). The structural parameters of each component as well as the total magnitudes and B/T ratios are randomly distributed to span the range of values found in real data. We then convolve each profile with a real PSF and embed the galaxies in a real background.

A key difference compared to previous approaches is that our fitting procedure fits all wavelengths simultaneously. This needs to be captured in the simulations too, i.e the profile needs to be simulated in every band. A random distribution of all parameters as a function of wavelength is not a good approximation to reality. As done in Vika et al. (2013), we simplified the problem by selecting a real low redshift galaxy ($z \sim 0.5$) presenting clearly two components (from visual inspection and our CNN classification) for which we obtained a bulge/disc decomposition (see figure 8). We then use the best SED models for the bulge and the disk as templates for our simulations (see section 6 for details on the SED fitting).

We first assign, to every simulated galaxy, a random B/T (in the i-band rest-frame) and a total magnitude (in the H band) in the range of [18 – 25]. This allows to fix

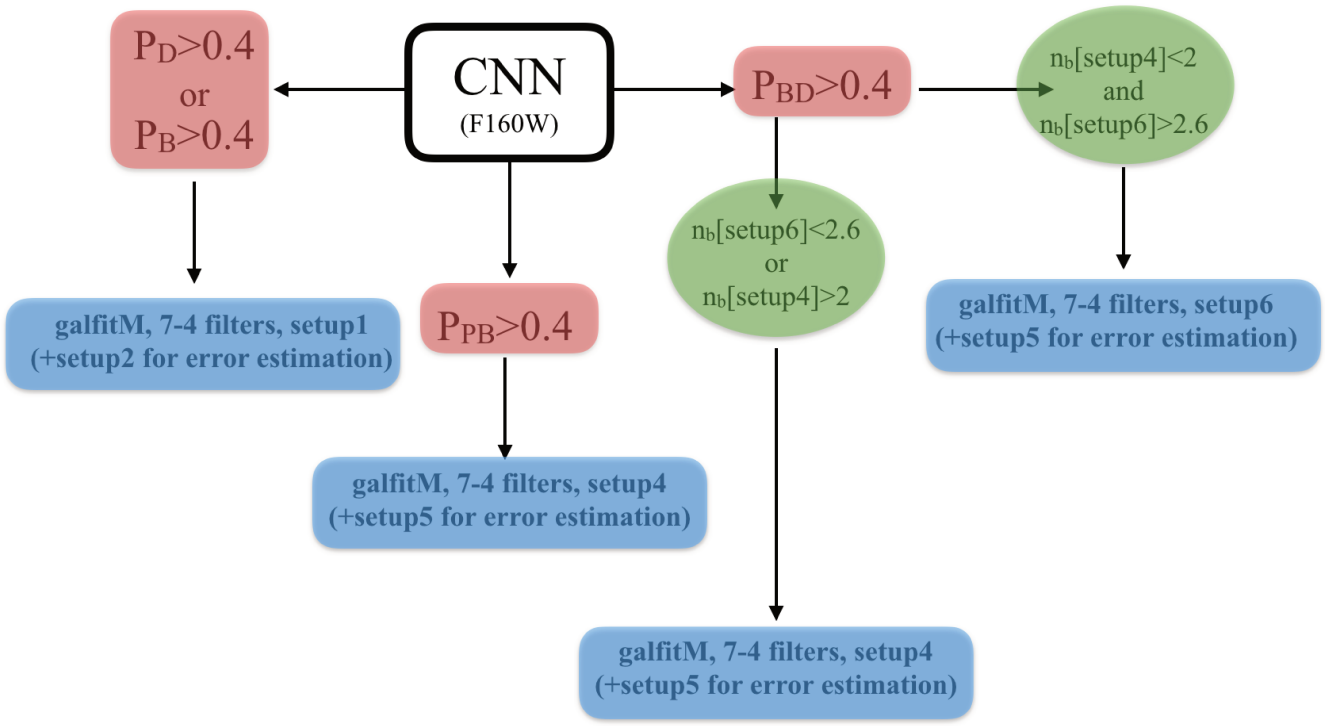

Figure 4. Flow chart showing the use of the different setups depending on the CNN based classification. This is the selection used to build the released *Gold catalog*.

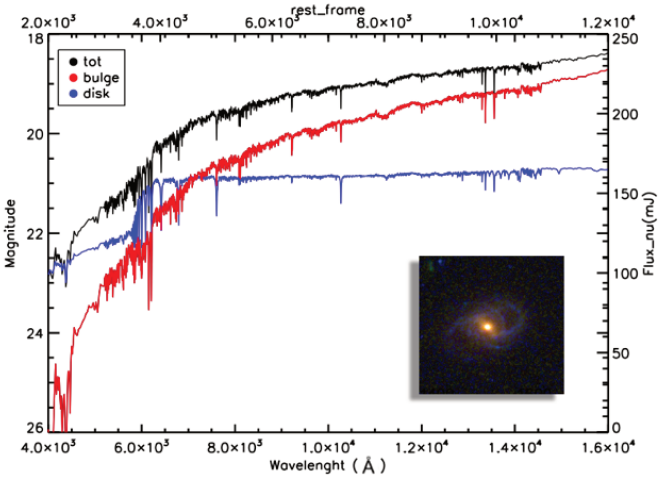

Figure 8. Template galaxy used for the simulation. The bulge SED is shown in red and the disk in blue. The black line shows the global SED. Random variations of this template are used to build a simulated sample (see text for details).

the bulge and disk fluxes in the H band. We also associate a random redshift in the range [0.01,3] and shift the SED template described above accordingly. This allows to associate a realistic magnitude in all other bands with a typical SED of a bulge and a disk while also accounting for the real redshift distribution. The surface brightness profile of the disk is rendered using an exponential profile. For the bulge component, we draw a random value of the Sersic index between 2 and 4, and we assume no wavelength dependence. In order to have a realistic wavelength dependence for the radii, we used random examples from the real data, imposing that the bulge should be always smaller than the disk. The final simulated sample contains ~ 4000 galaxies.

We then run GALAPAGOS-2 with exactly the same settings used for the real data and compare the input and recovered parameters to assess statistical errors.

Figure 9 compares the input and output sizes of bulges and disks for two different filters: F850,F160W. A complete visualization of all the parameter space is complex given the amount of parameters. We decided to highlight the dependence of the size with the galaxy morphology (quantified through B/T), the magnitude and the redshift. The accuracy on the photometry and stellar masses is discussed in section 6. As expected, we observe that the errors in the structural parameters of the disk (bulge) increase towards high (low) B/T values. When one of the two components dominates over the other it becomes more difficult to quantify both components properly. However, globally the errors remain within ~ 10−20%. Figure 9 also shows that at fainter magnitudes ($F160 > 23 - 23.5$) the bulge sizes start deviating from the zero bias line. This suggests that the S/N limit above which results become biased is reached (as pointed out by van der Wel et al. 2012 for 1 component fits). We thus apply a magnitude cut at $F160W = 23$ to keep a zero bias and a scatter lower than 30%. Only galaxies brighter than this magnitude limit will be included in the final catalog re-

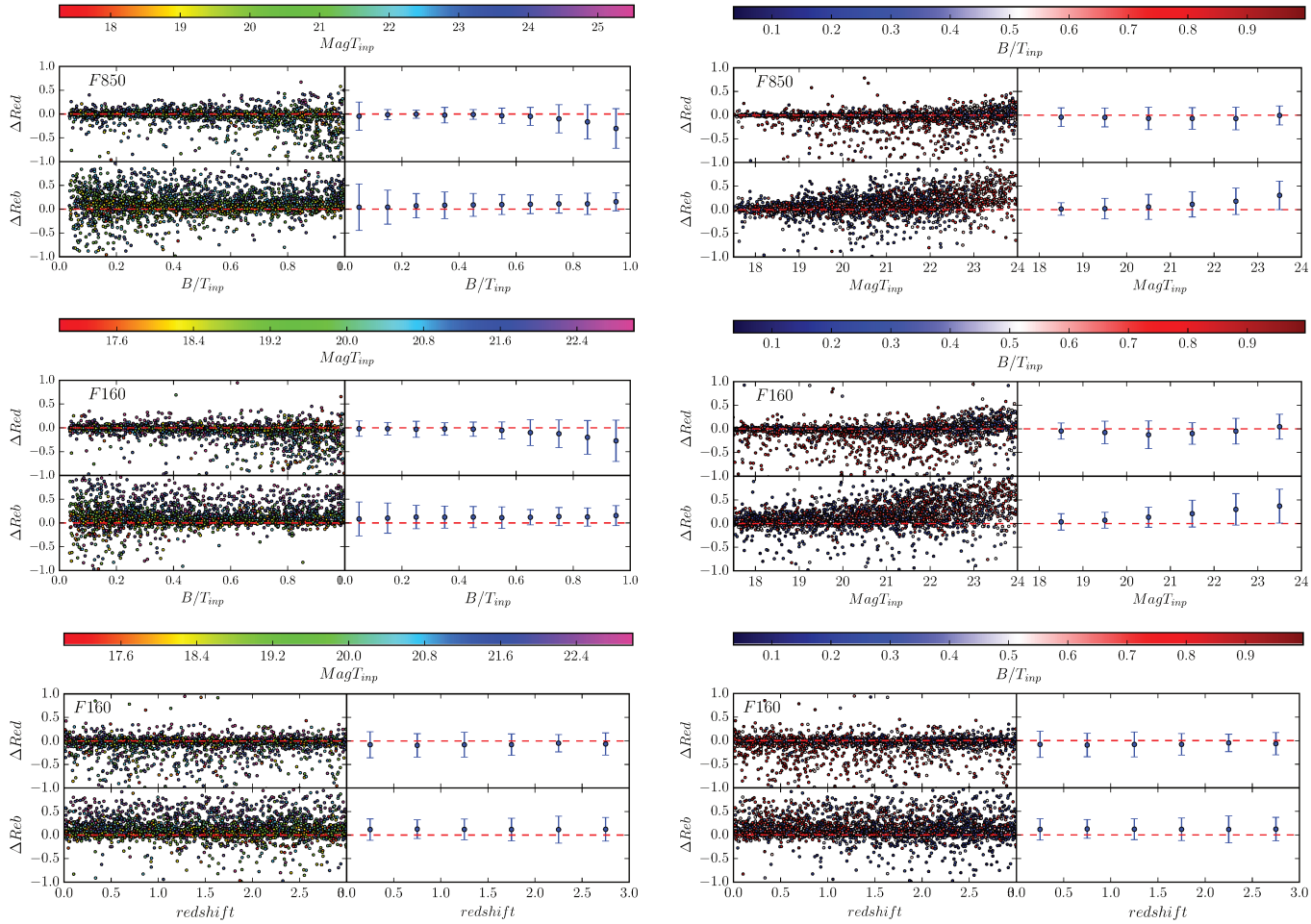

Figure 9. Comparison between simulated and recovered bulge (R_b) and disk (R_d) half-light radii in two filters: F850 (top line) and F160 (middle and bottom rows). All panels show in the y-axis the relative difference between input and output values: $\Delta Re = \frac{R_{in} - Rout}{R_{in}}$. The results are plotted against B/T (total magnitude) and color coded with total magnitude (B/T) in the left (right) panels. The last row shows the errors against redshift. In each plot we show individual galaxies in the left panels and binned median values and scatters on the right panels.

leased with this work. Finally, figure 9 also shows that errors do not strongly depend on redshift. We emphasize however that the simulations performed are not representative of the *real* evolution of galaxy SEDs since we are using a unique template.

5.3 Individual random uncertainties

The above procedure provides an estimate of the average error but does not estimate an error bar on an individual basis for every galaxy and every parameter. This is particularly required for this work in order to fit the SEDs of bulges and disks with stellar populations models (see section 6). Although, GALFIT provides error bars, they are known to be underestimated and not very indicative of the true error (see e.g. Häussler et al. 2007). This is generally explained because GALFIT assumes a gaussian noise distribution when computing the errors (which is not a good approximation for HST drizzled images) and also does not consider the effects of companions. In GALFITM, the situation is even more dramatic since the fits in all bands are not independent and the constraints in the different parameters are therefore coupled. The GALFIT manual states that in such a case, the estimation of errors is not reliable.

Therefore we follow an analogous approach to the one used in van der Wel et al. (2012) to estimate individual errors for each parameter. Since we have fitted all galaxies with different settings for each type of model (Sersic+Exponential, Sersic) the differences on the resulting fits between the two settings can be used to estimate random uncertainties. The main difference between the two runs resides on the wavelength dependence of the size and the Sersic index.

We assume that errors in the derived structural parameters of the 2 component fits depend essentially on the magnitude of the object, the Sersic index of the bulge, sizes of both components and the relative brightness of the two components measured by the bulge-to-total ratio in a given filter as well as on the *visual* aspect of the galaxy. For the one component fit, we postulate that errors depend on magnitude, Sersic index, effective radii and morphology. Other

parameters such as the position angle and the axis ratio are expected to have little impact on the errors. For each galaxy in the catalog and every band we compute thus 2 vectors $\mathbf{p^{1C}}$ $\mathbf{p^{2C}}$ for 1-component and 2-component respectively:

$$\mathbf{p^{1C}} = (\frac{m}{\sigma_m}, \frac{log(n)}{\sigma_{log(n)}}, \frac{log(R_e)}{\sigma_{log(R_e)}}, f_{sph,disk,irr})$$

$$\mathbf{p^{2C}} = (\frac{m}{\sigma_m}, \frac{log(n)}{\sigma_{log(n_b)}}, \frac{log(R_d)}{\sigma_{log(R_d)}}, \frac{log(R_e)}{\sigma_{log(R_e)}}, \frac{BT}{log(BT)}, f_{sph,disk,irr})$$

In the above equation, m designates the apparent magnitude in a given filter, n is the Sersic index, R_d and R_e are the effective radii of the disk and the bulge component and B/T is the ratio between the flux of the bulge and the total flux in the same band as M. f_{sph}, f_{disk} and f_{irr} are the probabilities that the galaxy looks like a spheroid, disk or irregular respectively (Huertas-Company et al. 2016). Each value is normalized by the dispersion to have similar variation ranges for all parameters.

Based on this vector p, we compute the 8D euclidian distance of each galaxy to all other galaxies in the catalog and select the 50 closest objects to a given galaxy[3]. This assumes that similar galaxies in terms of relative distance in the space defined by p should have similar errors in the structural parameters. Then the error on a given parameter (for example bulge magnitude) is taken as the 3-sigma clipped standard deviation of the difference between two setup estimates. The same technique is used to estimate errors on the 1 component Sersic fits, but in that case, the vector p is set to depend only on 5 quantities (magnitude, Sersic index, half light radius and morphology) as done in van der Wel et al. (2012).

Results are shown in figure 10. We show in particular the typical errors on magnitudes and sizes of both components. The typical magnitude error for the bulge and disk magnitudes are ~ 0.2 and ~ 0.1 mags respectively. As expected, it depends on the bulge-to-total ratio as already assessed by the simulations from the previous section. For objects with $B/T < 0.2$, the error on the bulge magnitude increases to $0.6 - 0.7$ magnitudes and the error on the disk magnitude rises to ~ 0.5 for $B/T > 0.8$. This confirms that the properties of embedded components are estimated accurately only if the dominant component represents less than 80% of the light. There is little or no dependence of the magnitude errors on other parameters such as the size or the Sersic index of the bulge. Regarding the errors on sizes of both components, the average error for the bulge is $\sim 20\%$ and $\sim 10\%$ for the disks, with again, a dependence on B/T.

Figure 11 shows the error dependence on wavelength. Both errors on magnitude and size are larger in shorter wavelengths. This is somehow expected since bluer bands are shallower. It is also easy to explain that bulges are more severely affected since they are expected to be redder and therefore fainter in the bluer wavelengths.

[3] changing this number by a factor of 2, does not significantly alter the results

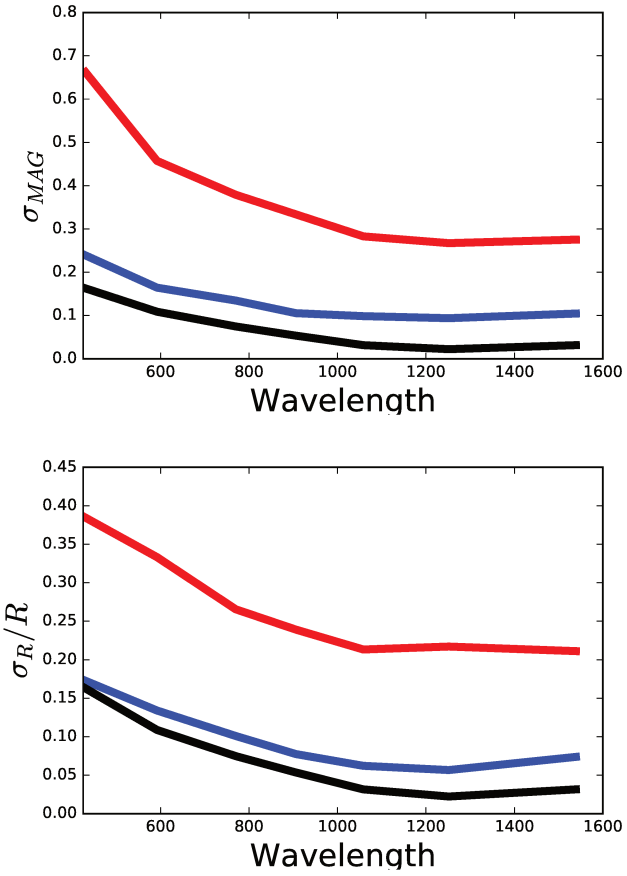

Figure 11. Average estimated random uncertainties for bulges (red lines), disks (blue lines) and the full galaxy (black lines) as a function of wavelength. Errors are larger in the bluer bands, especially for the bulge component as expected.

5.4 Comparison with the literature

Finally, we also perform a comparison with the literature. Namely, van der Wel et al. 2012 did a 1-component Sersic fit to all galaxies in CANDELS down to $H = 24.5$ in two NIR filters (F125,F160) independently. As described in the previous sections, the method used in this work differs from this work in the sense that all bands are fitted simultaneously. Although this technique is intended to benefit from a better S/N, one needs to make sure that no systematics are introduced in the process. At least for bright objects, similar results should be obtained in both works. In figure 12 are compared the magnitude, Sersic index and half light radii, from our catalog with the ones from van der Wel et al. (2012). There is a reasonable agreement with a systematic difference compatible with zero and a scatter of the order of $\sim 10\%$ increasing at fainter magnitudes as expected. The scatter is of the order of the error reported in the measurement as discussed by van der Wel et al. (2012). This result confirms then that our procedure works as expected at least for a 1 component fit and that no systematic biases are introduced by using all filters jointly.

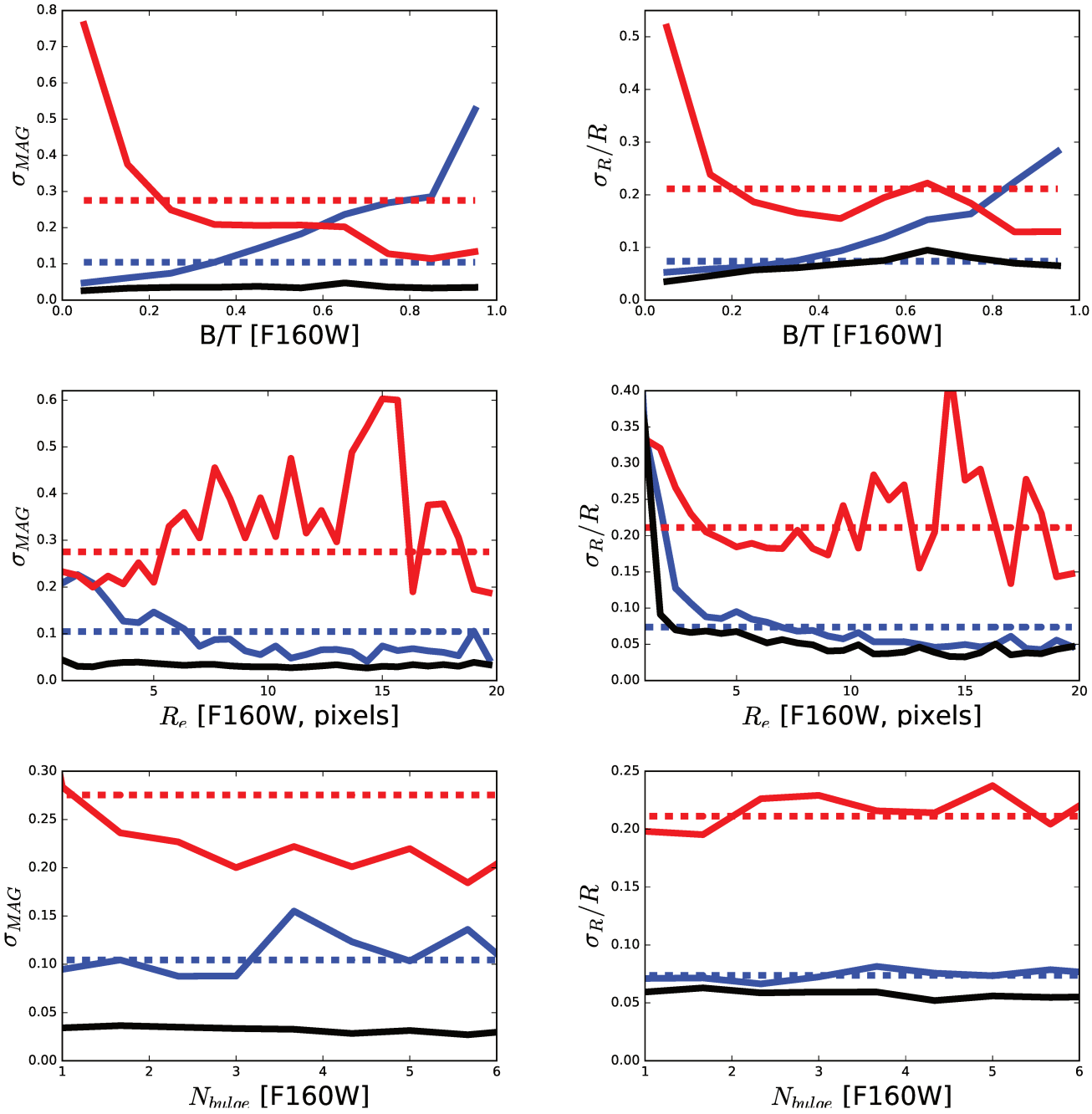

Figure 10. Average estimated random uncertainties in the derived structural parameters for bulges (red lines), disks (blue lines) and the full galaxy (black lines) as a function of structural parameters derived with setups 1 and 4. The left column shows the errors on the F160W magnitude and the right column on the effective radius in the same filter. Errors are shown as a function of B/T (top), size (middle), bulge Sersic index (bottom). Errors are estimated by computing the dispersion between measurements on similar objects with different setups as explained in the text. The general trend is that errors are larger for the bulge component than for the disk and that errors show mostly a dependence with B/T. The dashed horizontal lines are median errors computed for all the sample.

6 STELLAR POPULATION PROPERTIES OF BULGES AND DISKS

Using the methods described in the previous sections, we obtain 4-7 points SEDs for bulges and disks in our sample together with a measure of uncertainties in the derived fluxes in each band (see section 5). We then perform a standard SED fitting with the FAST code (Kriek et al 2009) and derive stellar masses, SFRs, ages and metallicities for all bulges and disks. Additionally, using the best-fit models we also derive rest-frame U,V,J colors for bulges and disks. The input models are grids of Bruzal & Charlot (2003) models that assume a Chabrier (2003) IMF and Calzetti et al.

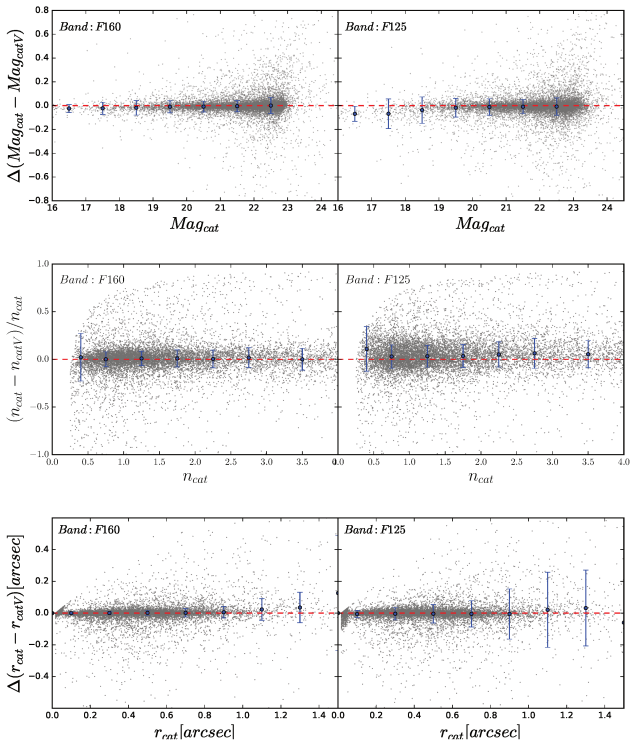

Figure 12. Comparison between our 1-component fits and the ones from van der Wel et al. (2012) in two filters. Results for the F160W and F125W filters are shown in the left and right panel respectively. Gray points in all panels show the difference between our measurements and the published ones for individual galaxies. Blue larger points are the median difference values and the error bars show the $3 - sigma$ clipped scatter. Top panels: magnitude difference. Middle panels: Sersic index. Bottom panels: half light radii.

(2000) extinction law. For the star formation history (SFH) we applied an exponentially declining model, with tau in the range of [8:10].

Figure 13 shows some examples of the best-fit templates for galaxies with one or two components according to the CNN based classification. More examples can be checked on line in the public release of the catalog[4].

Random uncertainties in the stellar population parameters are estimated by performing 500 MonteCarlo simulations for each galaxy. Assuming the errors on the fluxes as computed in section 5, we generate 500 SED realizations for each galaxy that we fit with FAST. The uncertainty on each parameter is derived as the minimum and maximum value within the 68% realizations with smaller reduced χ^2 values. Rest-frame colors are also computed for each realization and the uncertainty is computed in an analogous way.

Using the simulations described in 5.2, it is also possible to estimate a global statistical uncertainty on the stellar populations properties. Since the main quantity that will be used in forthcoming works are B/T ratios, we focus here on the stellar masses of both components. We notice that uncertainties in other parameters might be large given the reduced wavelength coverage and therefore should be used with caution.

We first run FAST on the simulated SEDs of both components and then perform a second run on the recovered fluxes from GALFITM on the same simulated galaxies. Figure 14 shows the comparison of both estimates. We find that the bias is close to zero and the dispersion of the order of $\sim 0.2 - 0.3$ dex, which is the typical error expected for SED based stellar masses. This results in an unbiased estimate of the stellar-mass bulge-to-total ratio with a typical scatter of ~ 0.2. Notice that this does not mean that the *true* stellar mass is recovered. It indicates however that GALFITM properly recovers the fluxes of the disk and bulge components without introducing additional systematics as already demonstrated for the sizes in section 5.2. Another additional check is shown in the right panel of figure 15 which compares the stellar mass obtained by fitting the photometry of a 1-component fit to the stellar mass obtained by adding the masses of the bulge and disk components. The two estimates agree within a ~ 0.2 dex uncertainty as expected.

Finally, in order to have an independent estimate of the reliability of the stellar masses derived with only 4-7 filters, we compare our values with the stellar masses estimated in CANDELS which cover a larger spectral range. This is shown in the two first panels of figure 15. Our estimates are unbiased, but with a scatter of ~ 0.4. This scatter should be a combination of model dependence (we did not use the same stellar populations models) and spectral sampling. As a matter of fact, when the sample is divided between galaxies for which we have a spectral sampling of 4 points or less and the others, the results are still unbiased but the scatter increases from ~ 0.3 with 4+ filters to ~ 0.4 with less than 4 filters.

7 FINAL CATALOG

The catalog release is made in three different tables. The same unique identifier is used to link all tables.

- *Gold catalog:* Contains a table with our best selected configuration for each galaxy. For each galaxy we provide the structural parameters in all bands derived from what we think is the best setup (see Table 2) according to the CNN best class. The selection essentially follows the flow chart of figure 5.1. For each parameter we then provide an errorbar computed with the method described in section 5.3. Additionally, we provide an estimate of the stellar mass bulge-to-total ratio as well as rest-frame colors for bulges and disks in the two GOODS fields. For standard uses, we recommend to use this catalog.
- An additional table with *all* structural measurements in all bands and setups described in this work is also provided along with the CNN outputs. This table should be used to explore different selections.
- A third table with the derived stellar population properties for bulges and disks resulting from the SED fitting as well as the uncertainties. This table allows to compute bulge to total stellar mass ratios.

[4] https://lerma.obspm.fr/huertas/form_CANDELS

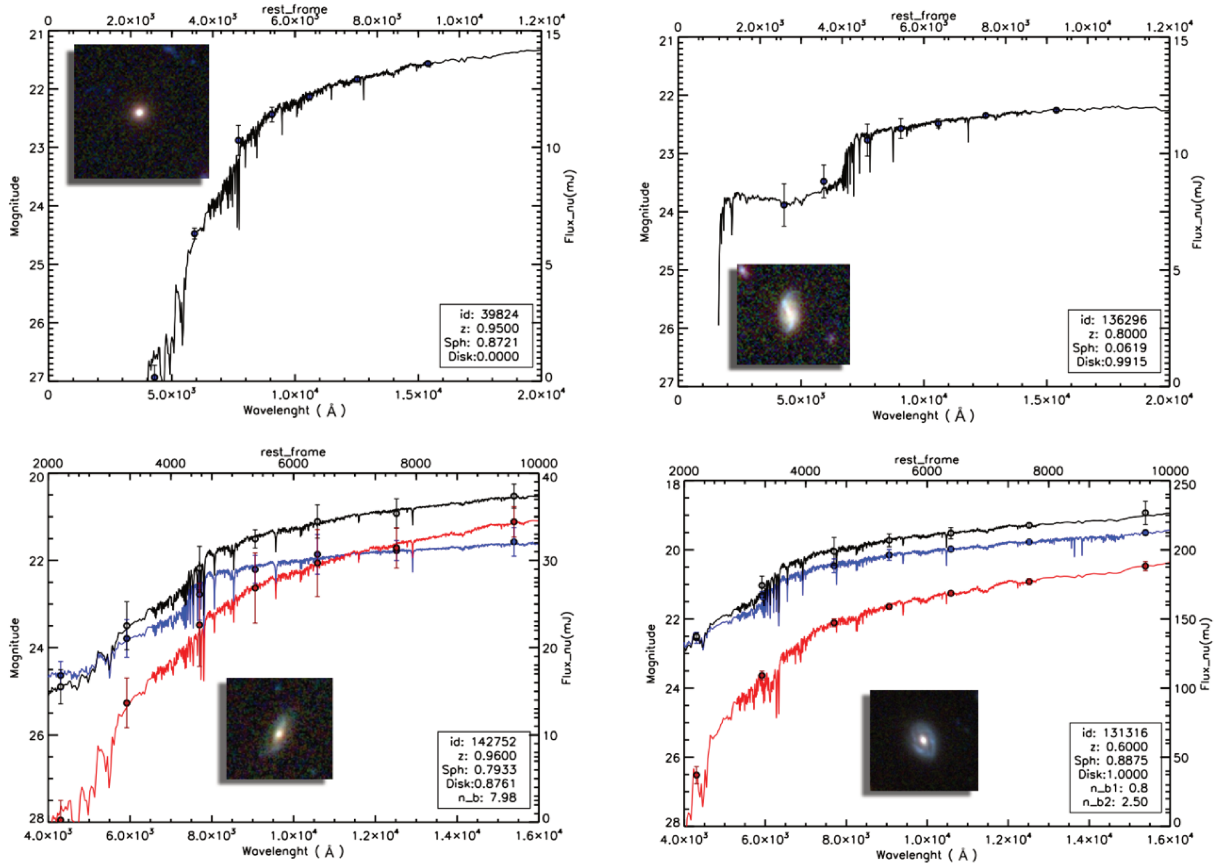

Figure 13. Examples of different morphologies, classified as explained in section 3. Top: pure bulge galaxy on the left and a pure disk one on the right. For both just a single profile is required. Bottom: Bulge+Exponential on the left and a Pseudo-Bulge+Exponential on the right. The color code is the same than for figure 8, Results from single Sersic fits are shown in black, red and blue are for the disk and the bulge components respectively. The points show the measured flux in the 7 bands. The solid line are the best fit models obtained with FAST.

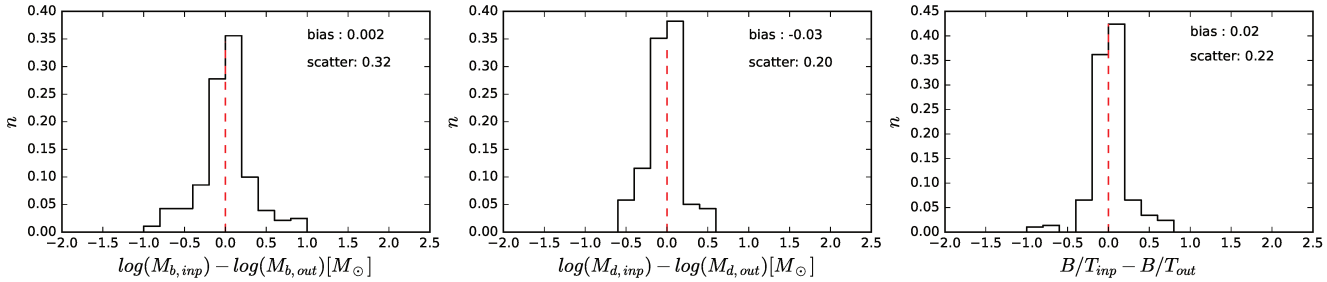

Figure 14. Distribution of the difference between the stellar masses estimated using the simulated photometry and the ones obtained with the recovered fluxes by MEGAMORPH (see text for details). Left panel: bulge mass, middle panel: disk mass. The right panel shows the error distribution of the stellar mass bulge-to-total ratio.

8 SUMMARY AND CONCLUSIONS

This work presents a catalog of multi-wavelength bulge-disc decompositions of ~ 17.000 galaxies in the five CANDELS fields. The dataset is mass complete down to $\sim 5\times10^{10}$ solar masses at $z \sim 2$.

Each galaxy is fitted with a 1-component Sersic model and a 2 component Sersic (bulge) + exponential (disk) model and with three different setups each in which we essentially modify the wavelength dependence of the size and Sersic index of the bulge component. We used the GALFITM/GALAPAGOS2 code from the MEGAMORPH project, allowing to simultaneously fit images at different wavelengths. One key new ingredient of this work is that we proposed a new method to address the systematic uncertainties arising from the use of a wrong model to describe the surface brightness profile of galaxies. The technique, based on convolutional neural networks, provides a quantitative measurement of how well a given profile (1 / 2 components) describes a given galaxy. We show that our proposed method can distin-

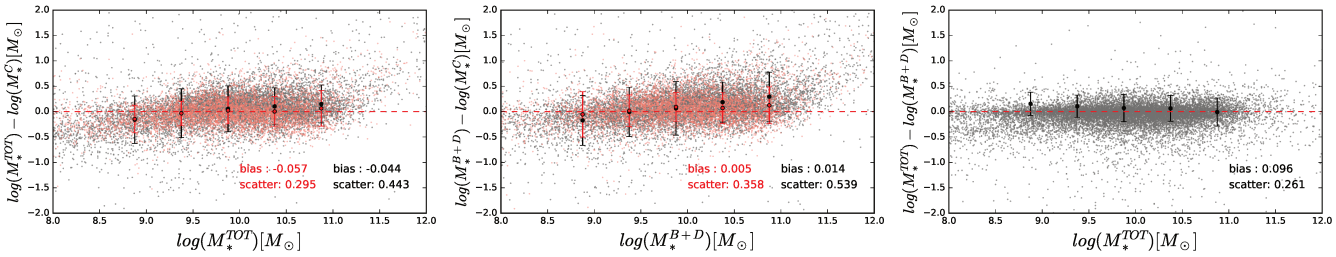

Figure 15. Uncertainties on stellar mass-estimates. The left panel shows the comparison between the stellar mass estimated in CANDELS (M_*^C) and our estimates based on fits to the photometry from a 2D Sersic fit (M_*^{TOT}). The middle panel shows the same comparison but using the stellar mass estimated by adding the masses of the disk and the bulge components (M_*^{B+D}). The red sample are galaxies covered by all 7 filters. Gray points show galaxies whose SED was fitted using four bands. The bias and the scatter are estimated independently for the two samples. Finally, the right panel shows the comparison between the total stellar mass obtained from fitting the photometry estimated with a Single Sersic and the stellar mass obtained by adding the stellar masses of the bulge and the disk.

guish between different profiles with a $\sim 80-90\%$ accuracy. It allows us to reduce the contamination from unphysical components at the $\sim 10\%$ level and study a clean sample of bulges and disks.

Through extensive simulations, we show that the structural parameters derived for bulges and disks are globally unbiased. We develop a method based on the comparison of results from different runs to provide individual error bars for each structural parameter. We show that the typical error for the bulge (disk) magnitudes are ~ 0.2 (~ 0.1) mags. For galaxies with $B/T < 0.2$ ($B/T > 0.8$) the error on the bulge (disk) magnitudes increases to ~ 0.5 mags. Sizes are estimated within $\sim 10-20\%$ uncertainty.

The derived spectral energy distributions of both components with realistic errors are then fitted with stellar population models to estimate stellar masses and bulge-to-total mass ratios. We show that the statistical uncertainties are of the order of $\sim 20\%$. We also provide rest-frame colors and SFRs which will be analyzed in forthcoming woks.

The catalog including all derived quantities is made public with the present work.

ACKNOWLEDGMENTS

The present work has essentially been funded by a French Doctoral Contract. The authors are also grateful to Google for the unrestricted gift given to the University of Santa Cruz to carry out the project: "Deep-Learning for Galaxies".

REFERENCES

Abramson, L. E., Gladders, M. D., Dressler, A., et al. 2016, ApJ, 832, 7
Abramson, L. E., Gladders, M. D., Dressler, A., et al. 2015, ApJL, 801, L12
Barden, M., Häußler, B., Peng, C. Y., McIntosh, D. H., & Guo, Y. 2012, MNRAS, 422, 449
Barro, G., Kriek, M., Pérez-González, P. G., et al. 2016, ApJL, 827, L32
Barro et al, 2015, ArXiv e-prints, astro-ph/1509.00469v1
Barro et al, 2014, Apj, 791, 52B
Barro, G., Faber, S. M., Pérez-González, P. G., et al. 2013, ApJ, 765, 104
Bluck, A. F. L., Mendel, J. T., Ellison, S. L., et al. 2014, MNRAS, 441, 599
Bournaud, F. 2016, Galactic Bulges, 418, 355
Bournaud, F., Perret, V., Renaud, F., et al. 2014, ApJ, 780, 57
Brinchmann, J., Charlot, S., White, S. D. M., et al. 2004, MNRAS, 351, 1151
Bruce, V. A., Dunlop, J. S., McLure, R. J., et al. 2014, MNRAS, 444, 1660
Bruce, V. A., Dunlop, J. S., McLure, R. J., et al. 2014, MNRAS, 444, 1001
Buitrago, F., Trujillo, I., Conselice, C. J., et al. 2008, ApJL, 687, L61
Carollo, C. M., Bschorr, T. J., Renzini, A., et al. 2013, ApJ, 773, 112
Carollo, C. M., Cibinel, A., Lilly, S. J., et al. 2014, arXiv:1402.1172
de la Rosa, I. G., La Barbera, F., Ferreras, I., et al. 2016, MNRAS, 457, 1916
Dahlen, T., Mobasher, B., Faber, S. M., et al. 2013, ApJ, 775, 93
Dekel, A., & Burkert, A. 2014, MNRAS, 438, 1870
Dekel, A., Birnboim, Y., Engel, G., et al. 2009, Nature, 457, 451
Delaye, L., Huertas-Company, M., Mei, S., et al. 2014, MNRAS, 441, 203
Elbaz, D., Daddi, E., Le Borgne, D., et al. 2007, A&A, 468, 33
Fisher, D. B., & Drory, N. 2016, Galactic Bulges, 418, 41
Galametz, A., Grazian, A., Fontana, A., et al. 2013, ApJS, 206, 10
Gargiulo, A., Bolzonella, M., Scodeggio, M., et al. 2016, arXiv:1611.07047
Genzel, R., Tacconi, L. J., Lutz, D., et al. 2015, ApJ, 800, 20
Giavalisco, M., Ferguson, H. C., Koekemoer, A. M., et al. 2004, ApJL, 600, L93
Glazebrook, K., Schreiber, C., Labbé, I., et al. 2017, Nature, 544, 71
Graham, A. W. 2013, Planets, Stars and Stellar Systems. Volume 6: Extragalactic Astronomy and Cosmology, 6, 91
Grogin, N. A., Kocevski, D. D., Faber, S. M., et al. 2011, ApJS, 197, 35
Guo, Q., White, S., Boylan-Kolchin, M., et al. 2011, MNRAS, 413, 101
Guo, Y., Ferguson, H. C., Bell, E. F., et al. 2015, ApJ, 800, 39
Guo, Y., Ferguson, H. C., Giavalisco, M., et al. 2013, ApJS, 207, 24
Hammer, F., Flores, H., Elbaz, D., et al. 2005, A&A, 430, 115
Häussler, B., McIntosh, D. H., Barden, M., et al. 2007, ApJS, 172, 615
Häußler, B., Bamford, S. P., Vika, M., et al. 2013, MNRAS, 430, 330

Huertas-Company, M., Shankar, F., Mei, S., et al. 2013, ApJ, 779, 29
Huertas-Company, M., Mei, S., Shankar, F., et al. 2013, MNRAS, 428, 1715
Huertas-Company, M., Gravet, R., Cabrera-Vives, G., et al. 2015, ApJS, 221, 8
Huertas-Company, M., Bernardi, M., Pérez-González, P. G., et al. 2016, MNRAS, 462, 4495
Hopkins, P. F., Cox, T. J., Younger, J. D., & Hernquist, L. 2009, ApJ, 691, 1168
Hopkins, P. F., Bundy, K., Croton, D., et al. 2010, ApJ, 715, 202
Huang, K.-H., Fall, S. M., Ferguson, H. C., et al. 2017, ApJ, 838, 6
Ilbert, O., McCracken, H. J., Le Fèvre, O., et al. 2013, A&A, 556, A55
Koekemoer, A. M., Faber, S. M., Ferguson, H. C., et al. 2011, ApJS, 197, 36
Kravtsov, A. V. 2013, ApJL, 764, L31
Kriek, M., et al. 2009, ApJ, 700, 221
Lange, R., Moffett, A. J., Driver, S. P., et al. 2016, MNRAS, 462, 1470
Lilly, S. J., & Carollo, C. M. 2016, ApJ, 833, 1
Lilly, S. J., Carollo, C. M., Pipino, A., Renzini, A., & Peng, Y. 2013, ApJ, 772, 119
Margalef-Bentabol, B., Conselice, C. J., Mortlock, A., et al. 2016, MNRAS, 461, 2728
Martig, M., Bournaud, F., Teyssier, R., & Dekel, A. 2009, ApJ, 707, 250
Meert, A., Vikram, V., & Bernardi, M. 2015, MNRAS, 446, 3943
Mei, S., Holden, B. P., Blakeslee, J. P., et al. 2009, ApJ, 690, 42
Muzzin, A., Marchesini, D., Stefanon, M., et al. 2013, ApJ, 777, 18
Naab, T., Johansson, P. H., & Ostriker, J. P. 2009, ApJL, 699, L178
Newman, A. B., Ellis, R. S., Bundy, K., & Treu, T. 2012, ApJ, 746, 162
Nipoti, C. 2012, Advances in Computational Astrophysics: Methods, Tools, and Outcome, 453, 233
Peng, C. Y., Ho, L. C., Impey, C. D., & Rix, H.-W. 2002, AJ, 124, 266
Peng et al., 2010
Pozzetti, L., Bolzonella, M., Zucca, E., et al. 2010, A&A, 523, A13
Rodriguez-Puebla, A., Primack, J. R., Avila-Reese, V., & Faber, S. M. 2017, arXiv:1703.04542
Sersic, J. L. 1968, Cordoba, Argentina: Observatorio Astronomico, 1968,
Shibuya, T., Ouchi, M., Kubo, M., & Harikane, Y. 2016, ApJ, 821, 72
Simard, L., Mendel, J. T., Patton, D. R., Ellison, S. L., & McConnachie, A. W. 2011, ApJS, 196, 11
Somerville, R. S., Behroozi, P., Pandya, V., et al. 2017, arXiv:1701.03526
Stefanon, M., Yan, H., Mobasher, B., et al. 2017, arXiv:1703.05768
Stringer, M. J., Shankar, F., Novak, G. S., et al. 2014, MNRAS, 441, 1570
Tacchella, S., Carollo, C. M., Forster Schreiber, N. M., et al. 2017, arXiv:1704.00733
Tacchella, S., Carollo, C. M., Renzini, A., et al. 2015, Science, 348, 314
Toomre, A. 1977, Evolution of Galaxies and Stellar Populations, 401
Trujillo, I. 2015, Galaxy Masses as Constraints of Formation Models, 311, 130
Popping, G., Decarli, R., Man, A. W. S., et al. 2017, arXiv:1703.05764
Stringer, M. J., Shankar, F., Novak, G. S., et al. 2014, MNRAS, 441, 1570
Tacchella, S., Carollo, C. M., Forster Schreiber, N. M., et al. 2017, arXiv:1704.00733
Tacchella, S., Dekel, A., Carollo, C. M., et al. 2016, MNRAS, 458, 242
van Dokkum, P. G., Franx, M., Kriek, M., et al. 2008, ApJL, 677, L5
van Dokkum, P. G., Nelson, E. J., Franx, M., et al. 2015, ApJ, 813, 23
van der Wel, A., Bell, E. F., Häussler, B., et al. 2012, ApJS, 203, 24
van der Wel, A., Franx, M., van Dokkum, P. G., et al. 2014, ApJ, 788, 28
Vika ,2014
Vika, M., Bamford, S. P., Häußler, B., et al. 2013, MNRAS, 435, 623
Whitaker, K. E., van Dokkum, P. G., Brammer, G., & Franx, M. 2012, ApJL, 754, L29
Whitaker, K. E., Bezanson, R., van Dokkum, P. G., et al. 2016, arXiv:1607.03107
Wisnioski, E., Förster Schreiber, N. M., Wuyts, S., et al. 2015, ApJ, 799, 209
Wuyts, S., Förster Schreiber, N. M., van der Wel, A., et al. 2011, ApJ, 742, 96
Zolotov, A., Dekel, A., Mandelker, N., et al. 2015, MNRAS, 450, 2327
Author A. N., 2013, Journal of Improbable Astronomy, 1, 1

Acknowledgments

I should to start the acknowledgments saying thanks to the fantastic people from the Astronomical Association (APA-lan) for guiding me to discover my passion for astronomy. The path is long. This thesis marks the final step of many years of study or perhaps it is only the beginning. We never stop learning.

All of this would not have been possible without the support of my family and all my friends that always make me seen the positive side of this adventure. Thanks to all friends from the lab (GEPI and LERMA) with whom I shared lunches and long coffee break. Here in Paris I could say that I have a second family. A big thanks to all the 'Astroguys' with whom I had a lot of drinks and parties. We should keep this tradition.

I cannot avoid a big thanks to Fiorella. We had a lot of crazy times together but also hard work days. I really had to thanks her and Fernando for their support along my last year. Each time I needed someone to speak they were there (even by Skype), thanks a lot for your patience!

Finally, if I am here writing the last page of the thesis is also thanks to my supervisors. Thanks for guiding me in this doctoral adventure.

Bibliography

Abramson, L. E., Gladders, M. D., Dressler, A., et al. 2016, ApJ, 832, 7

Abramson, L. E., Gladders, M. D., Dressler, A., et al. 2015, ApJL, 801, L12

Baldry, I. K., Glazebrook, K., Brinkmann, J., et al. 2004, ApJ, 600, 681

Barden, M., Häußler, B., Peng, C. Y., McIntosh, D. H., & Guo, Y. 2012, MNRAS, 422, 449

Barro, G., Kriek, M., Pérez-González, P. G., et al. 2016, ApJL, 827, L32

Barro et al, 2015, ArXiv e-prints, astro-ph/1509.00469v1

Barro, G., Faber, S. M., Pérez-González, P. G., et al. 2014, ApJ, 791, 52

Barro, G., Faber, S. M., Koo, D. C., et al. 2017, ApJ, 840, 47

Baugh, C. M., Cole, S., & Frenk, C. S. 1996, MNRAS, 283, 1361

Barro, G., Faber, S. M., Pérez-González, P. G., et al. 2013, ApJ, 765, 104

Belli, S., Newman, A. B., & Ellis, R. S. 2014, ApJ, 783, 117

Bennett, C. L., Larson, D., Weiland, J. L., et al. 2013, ApJS, 208, 20

Bernardi, M., Shankar, F., Hyde, J. B., et al. 2010, MNRAS, 404, 2087

Bertin, E. and Arnouts, S. et al. 1996, Astronomy & Astrophysics Supplement,117, 393-404

Behroozi, P. S., Wechsler, R. H., & Conroy, C. 2013, ApJ, 770, 57

Bryan, G. L., & Norman, M. L. 1998, ApJ, 495, 80

Brinchmann, J., Charlot, S., White, S. D. M., et al. 2004, MNRAS, 351, 1151

Bruzual, G. & Charlot, S. 2003, MNRAS, 344, 1000

Bluck, A. F. L., Mendel, J. T., Ellison, S. L., et al. 2014, MNRAS, 441, 599

Bournaud, F. 2016, Galactic Bulges, 418, 355

Bournaud, F., Perret, V., Renaud, F., et al. 2014, ApJ, 780, 57

Brinchmann, J., Charlot, S., White, S. D. M., et al. 2004, MNRAS, 351, 1151

Bruce, V. A., Dunlop, J. S., Cirasuolo, M., et al. 2012, MNRAS, 427, 1666

Bruce, V. A., Dunlop, J. S., McLure, R. J., et al. 2014, MNRAS, 444, 1660

Buitrago, F., Trujillo, I., Conselice, C. J., et al. 2008, ApJL, 687, L61

Bundy, K., Ellis, R. S., & Conselice, C. J. 2005, ApJ, 625, 621

Buta, R., & Combes, F. 1996, Fundamentals of Cosmic Physics, 17, 95

Buta, R. J., Sheth, K., Athanassoula, E., et al. 2015, ApJS, 217, 32

Calzetti, D., Armus, L., Bohlin, R. C., et al. 2000, ApJ, 533, 682

Cappellari, M., Emsellem, E., Krajnović, D., et al. 2011, MNRAS, 416, 1680

Carollo, C. M., Bschorr, T. J., Renzini, A., et al. 2013, ApJ, 773, 112

Carollo, C. M., Cibinel, A., Lilly, S. J., et al. 2014, arXiv:1402.1172

Cattaneo, A., Dekel, A., Faber, S. M., & Guiderdoni, B. 2008, MNRAS, 389, 567

Cattaneo, A., Faber, S. M., Binney, J., et al. 2009, Nature, 460, 213

Cebrián, M., & Trujillo, I. 2014, MNRAS, 444, 682

Chabrier, G. 2003, PASP, 115, 763

Cirasuolo, M., McLure, R. J., Dunlop, J. S., et al. 2007, MNRAS, 380, 585

Conselice, C. J. 2014, ARAA, 52, 291

Cowie, L. L., & McKee, C. F. 1977, ApJ, 211, 135

Daddi, E., Renzini, A., Pirzkal, N., et al. 2005, ApJ, 626, 680

Daddi, E., Dickinson, M., Morrison, G., et al. 2007, ApJ, 670, 156

Daddi, E., Bournaud, F., Walter, F., et al. 2010, ApJ, 713, 686

Dekel, A., Sari, R., & Ceverino, D. 2009, ApJ, 703, 785

de la Rosa, I. G., La Barbera, F., Ferreras, I., et al. 2016, MNRAS, 457, 1916

de Vaucouleurs, G. 1959, Handbuch der Physik, 53, 275

de Vaucouleurs, G. 1963, ApJS, 8, 31

Dahlen, T., Mobasher, B., Faber, S. M., et al. 2013, ApJ, 775, 93

Davis, M., Guhathakurta, P., Konidaris, N. P., et al. 2007, ApJL, 660, L1

Dekel, A., & Burkert, A. 2014, MNRAS, 438, 1870

Dekel, A., Birnboim, Y., Engel, G., et al. 2009, Nature, 457, 451

Delaye, L., Huertas-Company, M., Mei, S., et al. 2014, MNRAS, 441, 203

Eggen, O. J., Lynden-Bell, D., & Sandage, A. R. 1962, ApJ, 136, 748

Elbaz, D., Daddi, E., Le Borgne, D., et al. 2007, A&A, 468, 33

Elmegreen, D. M., Elmegreen, B. G., Ravindranath, S., & Coe, D. A. 2007, ApJ, 658, 763

Faber, S. M. 1972, A&A, 20, 361

Fang, J. J., Faber, S. M., Koo, D. C., & Dekel, A. 2013, ApJ, 776, 63

Fiore, F., Grazian, A., Santini, P., et al. 2008, ApJ, 672, 94-101

Fisher, D. B., & Drory, N. 2016, Galactic Bulges, 418, 41

Fontana, A., Pozzetti, L., Donnarumma, I., et al. 2004, A&A, 424, 23

Gadotti, D. A. 2009, MNRAS, 393, 1531

Gadotti, D. A. 2010, VizieR Online Data Catalog, 739,

Gadotti, D. A. 2011, MNRAS, 415, 3308

Gadotti, D. A., & Coelho, P. 2015, Highlights of Astronomy, 16, 339

Galametz, A., Grazian, A., Fontana, A., et al. 2013, ApJS, 206, 10

Gargiulo, A., Bolzonella, M., Scodeggio, M., et al. 2016, arXiv:1611.07047

Genzel, R., Tacconi, L. J., Combes, F., et al. 2012, ApJ, 746, 69

Genzel, R., Tacconi, L. J., Lutz, D., et al. 2015, ApJ, 800, 20

Giavalisco, M., Ferguson, H. C., Koekemoer, A. M., et al. 2004, ApJL, 600, L93

Glazebrook, K., Schreiber, C., Labbé, I., et al. 2017, Nature, 544, 71

Gott, J. R., III, & Thuan, T. X. 1976, ApJ, 204, 649

Graham, A. W. 2013, Planets, Stars and Stellar Systems. Volume 6: Extragalactic Astronomy and Cosmology, 6, 91

Grogin, N. A., Kocevski, D. D., Faber, S. M., et al. 2011, ApJS, 197, 35

Guo, Q., White, S., Boylan-Kolchin, M., et al. 2011, MNRAS, 413, 101

Guo, Y., Ferguson, H. C., Bell, E. F., et al. 2015, ApJ, 800, 39

Guo, Y., Ferguson, H. C., Giavalisco, M., et al. 2013, ApJS, 207,24

Guth, A. H. 1981, prd, 23, 347

Gunn, J. E., & Gott, J. R., III 1972, ApJ, 176, 1

Hammer, F., Flores, H., Elbaz, D., et al. 2005, A&A, 430, 115

Häußler, B., McIntosh, D. H., Barden, M., et al. 2007, ApJS, 172, 615

Häußler, B., Bamford, S. P., Vika, M., et al. 2013, MNRAS, 430, 330

Hatton, S., Devriendt, J. E. G., Ninin, S., et al. 2003, MNRAS, 343, 75

Hubble, E. 1929, Proceedings of the National Academy of Science, 15, 168

Huertas-Company, M., Shankar, F., Mei, S., et al. 2013, ApJ, 779, 29

Huertas-Company, M., Mei, S., Shankar, F., et al. 2013, MNRAS, 428, 1715

Huertas-Company, M., Gravet, R., Cabrera-Vives, G., et al. 2015, ApJS, 221, 8

Huertas-Company, M., Bernardi, M., Pérez-González, P. G., et al. 2016, MNRAS, 462, 4495

Hopkins, P. F., Cox, T. J., Younger, J. D., & Hernquist, L. 2009, ApJ, 691, 1168

Hopkins, P. F., Bundy, K., Croton, D., et al. 2010, ApJ, 715, 202

Hopkins, P. F., Kereš, D., Murray, N., Quataert, E., & Hernquist, L. 2012, MNRAS, 427, 968

Huang, K.-H., Fall, S. M., Ferguson, H. C., et al. 2017, ApJ, 838, 6

Humason, M. L. 1947, PASP, 59, 180

lbert et al

Ilbert, O., McCracken, H. J., Le Fèvre, O., et al. 2013, A&A, 556, A55

Kalinova, V., Colombo, D., Rosolowsky, E., et al. 2017, MNRAS, 469, 2539

Kauffmann, G., White, S. D. M., & Guiderdoni, B. 1993, MNRAS, 264, 201

Kauffmann, G., Heckman, T. M., White, S. D. M., et al. 2003, MNRAS, 341, 33

Kennicutt, R. C., Jr. 1998, ARAA, 36, 189

Knebe, A., Pearce, F. R., Thomas, P. A., et al. 2015, MNRAS, 451, 4029

Knobel, C., Lilly, S. J., Woo, J., & Kovač, K. 2015, ApJ, 800, 24

Koekemoer, A. M., Faber, S. M., Ferguson, H. C., et al. 2011, ApJS, 197, 36

Kravtsov, A. V. 2013, ApJL, 764, L31

Kriek, M., et al. 2009, ApJ, 700, 221

Kormendy, J. 1977, ApJ, 218, 333

Kormendy, J., & Richstone, D. 1995, ARAA, 33, 581

Kormendy, J., & Gebhardt, K. 2001, 20th Texas Symposium on relativistic astrophysics, 586, 363

Kormendy, J., & Fisher, D. B. 2008, Formation and Evolution of Galaxy Disks, 396, 297

Kormendy, J., & Bender, R. 2012, ApJS, 198, 2

Kormendy, J. 2015, Highlights of Astronomy, 16, 316

Kuchner, U., Ziegler, B., Verdugo, M., Bamford, S., & Häußler, B. 2017, A&A, 604, A54

Lang, P., Wuyts, S., Somerville, R. S., et al. 2014, ApJ, 788, 11

Lange, R., Moffett, A. J., Driver, S. P., et al. 2016, MNRAS, 462, 1470

Larson, R. B. 1975, MNRAS, 173, 671

Larson, R. B. 1976, MNRAS, 176, 31

Laurikainen, E., Salo, H., & Buta, R. 2005, MNRAS, 362, 1319

Laurikainen, E., Salo, H., Buta, R., & Knapen, J. H. 2011, Advances in Astronomy, 2011, 516739

Lawrence, A., Warren, S. J., Almaini, O., et al. 2007, MNRAS, 379, 1599

Lilly, S. J., & Carollo, C. M. 2016, ApJ, 833, 1

Lilly, S. J., Carollo, C. M., Pipino, A., Renzini, A., & Peng, Y. 2013, ApJ, 772, 119

Madau, P., & Dickinson, M. 2014, ARAA, 52, 415

Maltby, D. T., Aragón-Salamanca, A., Gray, M. E., et al. 2010, MNRAS, 402, 282

Mancini, C., Daddi, E., Renzini, A., et al. 2010, MNRAS, 401, 933

Mancini, C., Renzini, A., Daddi, E., et al. 2015, MNRAS, 450, 763

Margalef-Bentabol, B., Conselice, C. J., Mortlock, A., et al. 2016, MNRAS, 461, 2728

Martig, M., Bournaud, F., Teyssier, R., & Dekel, A. 2009, ApJ, 707, 250

Martig, M., Crocker, A. F., Bournaud, F., et al. 2013, MNRAS, 432, 1914

Meert, A., Vikram, V., & Bernardi, M. 2015, MNRAS, 446, 3943

Mei, S., Holden, B. P., Blakeslee, J. P., et al. 2009, ApJ, 690, 42

Mo, H. J., Mao, S., & White, S. D. M. 1998, MNRAS, 295, 319

Moore, B., Katz, N., Lake, G., Dressler, A., & Oemler, A. 1996, Nature, 379, 613

Mortlock, A., Conselice, C. J., Hartley, W. G., et al. 2013, MNRAS, 433, 1185

Morselli, L., Popesso, P., Erfanianfar, G., & Concas, A. 2017, A&A, 597, A97

Muzzin, A., Marchesini, D., Stefanon, M., et al. 2013, ApJ, 777, 18

Naab, T., Johansson, P. H., & Ostriker, J. P. 2009, ApJL, 699, L178

Nair, P. B., & Abraham, R. G. 2010, VizieR Online Data Catalog, 218

Newman, A. B., Ellis, R. S., Bundy, K., & Treu, T. 2012, ApJ, 746, 162

Nipoti, C. 2012, Advances in Computational Astrophysics: Methods, Tools, and Outcome, 453, 233

Nulsen, P. E. J. 1982, MNRAS, 198, 1007

Ostriker, J. P., & Steinhardt, P. J. 1995, arXiv:astro-ph/9505066

Ostriker, J. P., & Steinhardt, P. 2003, Science, 300, 1909

Pacucci, F., Ferrara, A., Grazian, A., et al. 2016, MNRAS, 459, 1432

Papovich, C., Bassett, R., Lotz, J. M., et al. 2012, ApJ, 750, 93

Peng, C. Y., Ho, L. C., Impey, C. D., & Rix, H.-W. 2002, AJ, 124, 266

Peng et al., 2010

Peng et al., 2015

Penzias, A. A., & Wilson, R. W. 1965, ApJ, 142, 419

Pérez-González, P. G., Cava, A., Barro, G., et al. 2013, ApJ, 762, 46

Planck Collaboration, Ade, P. A. R., Arnaud, M., et al. 2014, A&A, 571, A31

Poggianti, B. M., Calvi, R., Bindoni, D., et al. 2013, ApJ, 762, 77

Pozzetti, L., Bolzonella, M., Zucca, E., et al. 2010, A&A, 523, A13

Quilis, V., Planelles, S., & Ricciardelli, E. 2017, MNRAS, 469, 80

Roberts, M. S., & Whitehurst, R. N. 1975, ApJ, 201, 327

Rodighiero, G., Brusa, M., Daddi, E., et al. 2015, ApJL, 800, L10

Rodriguez-Puebla, A., Primack, J. R., Avila-Reese, V., & Faber, S. M. 2017, arXiv:1703.04542

Rowlands, K., Wild, V., Bourne, N., et al. 2017, arXiv:1707.07989

Rubin, V. C., & Ford, W. K., Jr. 1970, ApJ, 159, 379

Sandage, A. 1986, A&A, 161, 89

Salim, S., Rich, R. M., Charlot, S., et al. 2007, ApJS, 173, 267

Salo, H., Laurikainen, E., Laine, J., et al. 2015, ApJS, 219, 4

Schawinski, K., Urry, C. M., Simmons, B. D., et al. 2014, MNRAS, 440, 889

Schmidt, M. 1959, ApJ, 129, 243

Scoville, N., Aussel, H., Brusa, M., et al. 2007, ApJS, 172, 1

Sérsic, J. L. 1968, Cordoba, Argentina: Observatorio Astronomico, 1968,

Shen, S., Mo, H. J., White, S. D. M., et al. 2003, MNRAS, 343, 978

Shibuya, T., Ouchi, M., Kubo, M., & Harikane, Y. 2016, ApJ, 821, 72

Simard, L., Mendel, J. T., Patton, D. R., Ellison, S. L., & McConnachie, A. W. 2011, ApJS, 196, 11

Somerville, R. S., Behroozi, P., Pandya, V., et al. 2017, arXiv:1701.03526

Smoot, G. F., Bennett, C. L., Kogut, A., et al. 1992, ApJL, 396, L1

Speagle, J. S., Steinhardt, C. L., Capak, P. L., & Silverman, J. D. 2014, ApJS, 214, 15

Springel, V., White, S. D. M., Jenkins, A., et al. 2005, Nature, 435, 629

Stefanon, M., Yan, H., Mobasher, B., et al. 2017, arXiv:1703.05768

Stringer, M. J., Shankar, F., Novak, G. S., et al. 2014, MNRAS, 441, 1570

Tacchella, S., Carollo, C. M., Forster Schreiber, N. M., et al. 2017, arXiv:1704.00733

Tacchella, S., Dekel, A., Carollo, C. M., et al. 2016, MNRAS, 458, 242

Tacchella, S., Carollo, C. M., Renzini, A., et al. 2015, Science, 348, 314

Tacconi, L. J., Genzel, R., Neri, R., et al. 2010, Nature, 463, 781

Taylor, E. N., Franx, M., Glazebrook, K., et al. 2010, ApJ, 720, 723

Tasca, L. A. M., Le Fèvre, O., Hathi, N. P., et al. 2015, A&A, 581, A54

Toft, S., Zabl, J., Richard, J., et al. 2017, Nature, 546, 510

Toomre, A., & Toomre, J. 1972, ApJ, 178, 623

Tomczak, A. R., Quadri, R. F., Tran, K.-V. H., et al. 2016, ApJ, 817, 118

Trujillo, I., Förster Schreiber, N. M., Rudnick, G., et al. 2006, ApJ, 650, 18

Trujillo, I., Conselice, C. J., Bundy, K., et al. 2007, MNRAS, 382, 109

Trujillo, I., Cenarro, A. J., de Lorenzo-Cáceres, A., et al. 2009, ApJL, 692, L118

Trujillo, I. 2015, Galaxy Masses as Constraints of Formation Models, 311, 130

Popping, G., Decarli, R., Man, A. W. S., et al. 2017, arXiv:1703.05764

van de Sande, J., Kriek, M., Franx, M., et al. 2011, ApJL, 736, L9

van Dokkum, P. G., Franx, M., Kriek, M., et al. 2008, ApJL, 677, L5

van Dokkum, P. G., Nelson, E. J., Franx, M., et al. 2015, ApJ, 813, 23

van den Bosch, F. C. 1998, ApJ, 507, 601

van der Wel, A., Bell, E. F., van den Bosch, F. C., Gallazzi, A., & Rix, H.-W. 2009, ApJ, 698, 1232

van der Wel, A., Bell, E. F., Häussler, B., et al. 2012, ApJS, 203, 24

van der Wel, A., Franx, M., van Dokkum, P. G., et al. 2014, ApJ, 788, 28

van den Bergh, S. 1976, ApJ, 206, 883

Vera, M., Alonso, S., & Coldwell, G. 2016, A&A, 595, A63

Vika ,2014

Vika, M., Bamford, S. P., Häußler, B., et al. 2013, MNRAS, 435, 623

Volonteri, M. 2010, A&ARv, 18, 279

Vulcani, B., Bamford, S. P., Häußler, B., et al. 2014, MNRAS, 441, 1340

Walcher, J., Groves, B., Budavári, T., & Dale, D. 2011, Astrophysics and Space Science, 331, 1

Wang, W., Faber, S. M., Liu, F. S., et al. 2017, MNRAS, 469, 4063

Whitaker, K. E., van Dokkum, P. G., Brammer, G., & Franx, M. 2012, ApJL, 754, L29

Whitaker, K. E., Franx, M., Leja, J., et al. 2014, ApJ, 795, 104

Whitaker, K. E., Bezanson, R., van Dokkum, P. G., et al. 2016, arXiv:1607.03107

Williams, R. E., Blacker, B., Dickinson, M., et al. 1996, AJ, 112, 1335

Wisnioski, E., Förster Schreiber, N. M., Wuyts, S., et al. 2015, ApJ, 799, 209

Wuyts, S., Förster Schreiber, N. M., van der Wel, A., et al. 2011, ApJ, 742, 96

Zanella, A., Scarlata, C., Corsini, E. M., et al. 2016, ApJ, 824, 68

Zolotov, A., Dekel, A., Mandelker, N., et al. 2015, MNRAS, 450, 2327

Zwicky, F. 1933, Helvetica Physica Acta, 6, 110

Author A. N., 2013, Journal of Improbable Astronomy, 1, 1

Résumé

Les galaxies passives présentent des morphologies et des propriétés structurelles diff'erentes, que les galaxies, avec masse similaire, formant des étoiles. La distribution bimodale dans les relations d'eschelle suggére un lien entre le processus de quenching et les structures des galaxies. Comprendre les mécanismes et la chronologie de la formation du bulbe s'avére fondamental pour comprendre l'origine de cette corrélation. Les bulbes grossissent-ils au cours de la séquence principale? Les galaxies réaccrétent-elles un disque? Les galaxies cessent-elles leur formation d'étoiles á partir des régions internes? etc.
Répondre á ces questions nécessite de résoudre les parties internes des galaxies á différentes époques. Grâce aux données de haute résolution en multi-longueur d'ondes CANDELS, j'ai réalisé une décomposition bulbe-disque á partir des courbes de brillance de surface de $\simeq 17.300$ galaxies (F160W<23, 0<z<2) dans 4 $\acute{7}$ filtres couvrant un intervalle spectral compris entre 430-1600 nm. Une approche novatrice bas'ee sur le deep-learning, nous permet de s'electionner á priori les meilleurs profils. J'ai modélisé la SED afin d'obtenir les masses stellaires et les couleurs. Le résultat est un catalogue contenant les informations structurelles/morphologiques et les propriétés des populations stellaires d'un vaste échantillonnage de bulbes et de disques galactiques. Il s'agit de le catalogue plus grand et plus complet á des redshifts $z < 2$.
Le catalogue est utilisé pour comprendre comment les galaxies cessent leur formation d'étoiles et pour déterminer l'impact que le quenching peut avoir sur la morphologie. Les tailles de disques et bulbes massive ($M_* > 2 * 10^{10} M_\odot$) ne sont pas dependent de la morphologie (B/T). Ce résultat suggére une unique mécanismes de formation pour les bulbes massifs mais aussi que la survie ou la re-croissance du disque est un processus commun aprés la formation du bulbe. Toutefois, les bulbes pures (B/T>0.8) ont des tailles 30% plus grandes et ont un indice Sérsic également plus élevé. Ceci est compatible avec une croissance ultérieure tardive de ces systémes par fusion de galaxies.
Les bulbes dans galaxies forment étoilés sont 30% plus grand que les bulbes dans galaxies passive (a masse fixée). Concernant le disques, ils ne montre pas de difference entre le deux cas. Ces résultats peuvent être interprété comme un signe que les galaxies subissent une transformation morphologique supplémentaire pendant ou aprés le quenching. Pourtant, ils ne sont pas libre de l'effet appelé 'progenitor bias.
La plus part de (sinon tout) les pure disques (B/T<0.2) vivent au long de la sequence principale. Le quenching sans croissance de le bulbe n'est pas un processus commun. Pure "blue" bulbe (B/T>0.8) existent, suggérant que la formation des bulbes a lieux quand les galaxies sont encore formant étoiles.
Afin de mettre des contraintes sur le temp de formation des bulbes et des disques, J'ai étudié les couleurs U,V,J. La plupart des galaxies ont négatif pente dans le couleur. Les bulbes sont plus rouges que les disques dans galaxies que sont actifs, au tout les époque. Cette scénario est compatible avec le modéle inside-out quenching propos'ee deja dans précédent travails. Néanmoins, rejuvenation pour l'accretion d'un nouveaux disque porte le meme signature.

Mots Clés

structure des galaxies, evolution des galaxies, galaxy morphologie, quenching mechanisms.

Abstract

Passive galaxies have different morphologies and structural properties than star-forming galaxies of similar mass. The evidence of a bimodal distribution of galaxy properties suggests a link between the quenching process and and galaxy structure. Understanding the origin of this correlation requires establishing constraints on the mechanisms as well as on the timing of bulge formation. How are bulges formed?Do bulges grow in the main sequence? Are galaxies re-accreting a star forming disk? Do galaxies start to quench from the inside? etc.
Proper answers to these questions require resolving the internal components of galaxies at different epochs. Thanks to the CANDELS high-resolution multi-wavelength data, I performed 2-D bulge-disk decompositions of the surface brightness profile of $\simeq 17'300$ galaxies (F160W < 23, 0 < z < 2) in 4-7 filters, covering a spectral distribution of 430-1600 nm. A novel approach, based on deep-learning, allowed us to make an a-priori selection of the best profile. Stellar parameters are computed trough the SED fitting. The final catalog contains structural/morphological informations together with the stellar population properties for a large sample of bulges and disks within galaxies. This is the largest and more complete catalog of bulge-disc decompositions at $z < 2$. The catalog is then used to investigate how galaxies quench and transform their morphologies.
The size of disks and massive bulge is independent of the bulge-to-total ratio ($M_* > 2 * 10^{10} M_\odot$). It suggests a unique formation process for massive bulges and also that disk survival/regrowth is a common phenomenon after bulge formation. However pure bulges (B/T>0.8), are 20% larger than bulges embedded in disks at fixed stellar mass and have larger Sérsic indices. This is compatible with a later growth of these systems through minor mergers.
Bulges in star-forming galaxies are found to be 20-30% larger than bulges in quenched systems, at fixed stellar mass. This can be interpreted as a signature that galaxies experience an additional morphological transformation during or after quenching. However, this result is not free of progenitor bias.
Moreover, the vast majority (if not all) of pure disks (B/T<0.2) in our sample lie in the main-sequence. It suggests that quenching without any bulge growth is not a common channel at least in the field environment probed by our data. Pure "blue" bulges (B/T>0.8) do exist however, suggesting that the formation of bulges happens while galaxies are still star forming.
Finally, in order to put constraints on the formation times of bulges and disks I analyzed the UVJ rest-frame colors. Almost all galaxies in our sample present negative color gradients. Bulges are always redder than the disks at all redshifts. This is compatible with a scenario of inside-out quenching put forward by previous works. However rejuvenation through disk accretion could lead to similar signatures.

Keywords

galaxy structure, galaxy evolution, galaxy morphology, quenching mechanisms.